

Supplementary Information

Contents

Appendix S1. Site Details	3
Appendix S2. Methods for reconstruction of <i>DBH</i>	5
Appendix S3. Methods for climate data evaluation and correction	6
Appendix S4. Methods for comparing our approach with traditional methods	7
Appendix S5. Dealing with rapidly changing climate and tree growth	9
Table S1. Site Details.	11
Table S2. Species analyzed, their characteristics, and bark allometries applied.	12
Table S3. Sampling details for species by site.	13
Table S4. Allometric equations for bark thickness.	15
Table S5. Qualitative comparison of results from this study with previous studies employing conventional methods.	16
Figure S1. Density plot of core record start years by species for BCNM.	19
Figure S2. Density plot of core record start years by species for HKK.	20
Figure S3. Density plot of core record start years by species for SCBI.	21
Figure S4. Density plot of core record start years by species for LDW.	22
Figure S5. Density plot of core record start years by species for HF.	23
Figure S6. Density plot of core record start years by species for ZOF.	24
Figure S7. Density plot of core record start years by species for NIO.	25
Figure S8. Density plot of core record start years by species for LT.	26
Figure S9. Density plot of core record start years by species for CB.	27
Figure S10. Density plot of core record start years by species for SC.	28
Figure S11. Comparison of our approach with traditional methods of identifying climate signals: <i>Liriodendron tulipifera</i> at SCBI.	29
Figure S12. Comparison of our approach with traditional methods of identifying climate signals: <i>Abies alba</i> at Zofin.	30
Figure S13. Comparison of our approach with traditional methods of identifying climate signals: <i>Pseudotsuga menziesii</i> at Cedar Breaks.	31
Figure S14. Comparison of our approach with traditional methods of identifying climate signals: <i>Picea mariana</i> at Scotty Creek.	32
Figure S15. Climwin output for water variable group at BCNM.	33
Figure S16. Climwin output for temperature variable group at BCNM.	34
Figure S17. Climwin output for water variable group at HKK.	35
Figure S18. Climwin output for temperature variable group at HKK.	36
Figure S19. Climwin output for water variable group at SCBI.	37
Figure S20. Climwin output for temperature variable group at SCBI.	38
Figure S21. Climwin output for water variable group at LDW.	39
Figure S22. Climwin output for temperature variable group at LDW.	40
Figure S23. Climwin output for water variable group at HF.	41
Figure S24. Climwin output for temperature variable group at HF.	42
Figure S25. Climwin output for water variable group at ZOF.	43
Figure S26. Climwin output for temperature variable group at ZOF.	44
Figure S27. Climwin output for water variable group at NIO.	45
Figure S28. Climwin output for temperature variable group at NIO.	46
Figure S29. Climwin output for water variable group at LT.	47

Figure S30. Climwin output for temperature variable group at LT.	48
Figure S31. Climwin output for water variable group at CB.	49
Figure S32. Climwin output for temperature variable group at CB.	50
Figure S33. Climwin output for water variable group at SC.	51
Figure S34. Climwin output for temperature variable group at SC.	52
Figure S35. Best GLS models including climate and <i>DBH</i> for BCNM	53
Figure S36. Best GLS models including climate, <i>DBH</i> , and year for BCNM	54
Figure S37. Best GLS models including climate and <i>DBH</i> for HKK	55
Figure S38. Best GLS models including climate, <i>DBH</i> , and year for HKK	56
Figure S39. Best GLS models including climate and <i>DBH</i> for SCBI	57
Figure S40. Best GLS models including climate, <i>DBH</i> , and year for SCBI	58
Figure S41. Best GLS models including climate and <i>DBH</i> for LDW	59
Figure S42. Best GLS models including climate, <i>DBH</i> , and year for LDW	60
Figure S43. Best GLS models including climate and <i>DBH</i> for HF	61
Figure S44. Best GLS models including climate, <i>DBH</i> , and year for HF	62
Figure S45. Best GLS models including climate and <i>DBH</i> for ZOF	63
Figure S46. Best GLS models including climate, <i>DBH</i> , and year for ZOF	64
Figure S47. Best GLS models including climate and <i>DBH</i> for NIO	65
Figure S48. Best GLS models including climate, <i>DBH</i> , and year for NIO	66
Figure S49. Best GLS models including climate and <i>DBH</i> for LT	67
Figure S50. Best GLS models including climate, <i>DBH</i> , and year for LT	68
Figure S51. Best GLS models including climate and <i>DBH</i> for CB	69
Figure S52. Best GLS models including climate, <i>DBH</i> , and year for CB	70
Figure S53. Best GLS models including climate and <i>DBH</i> for SC	71
Figure S54. Best GLS models including climate, <i>DBH</i> , and year for SC	72
Figure S55. Climate responses at SC before and after 1970.	73
Figure S56. All significant climate - <i>DBH</i> interactions with <i>RW</i> as the response metric.	74
Figure S57. All significant climate - <i>DBH</i> interactions with <i>RW</i> as the response metric.	76
Figure S58. Relationships between <i>DBH</i> and <i>BAI</i> by decade for BCNM.	77
Figure S59. Relationships between <i>DBH</i> and <i>BAI</i> by decade for HKK.	78
Figure S60. Relationships between <i>DBH</i> and <i>BAI</i> by decade for SCBI.	79
Figure S61. Relationships between <i>DBH</i> and <i>BAI</i> by decade for LDW.	80
Figure S62. Relationships between <i>DBH</i> and <i>BAI</i> by decade for HF.	81
Figure S63. Relationships between <i>DBH</i> and <i>BAI</i> by decade for ZOF.	82
Figure S64. Relationships between <i>DBH</i> and <i>BAI</i> by decade for NIO.	83
Figure S65. Relationships between <i>DBH</i> and <i>BAI</i> by decade for LT.	84
Figure S66. Relationships between <i>DBH</i> and <i>BAI</i> by decade for CB.	85
Figure S67. Relationships between <i>DBH</i> and <i>BAI</i> by decade for SC.	86
SI References	87

Appendix S1. Site Details

Barro Colorado Nature Monument, Panama

Cores were collected within the Barro Colorado Nature Monument (BCNM), a 5600-ha reserve established in 1923 that includes Barro Colorado Island (BCI) and the surrounding mainland peninsulas (Alfaro-Sánchez et al., 2017). BCNM contains a mix of old-growth and mature secondary tropical moist forest. Live canopy trees on the peninsulas were cored between January 2015 and April 2015. In addition, several fallen dead trees on BCI were sampled by taking discs with chain saws.

We note that the secondary forest status of much of BCNM differs from ForestGEO's 50-ha plot on BCI, which is old-growth, and shows little directional trend in woody productivity (Rutishauser et al., 2020).

Huai Kha Khaeng, Thailand

Cores were collected within a ~300 ha acre area of seasonal dry evergreen and mixed deciduous forest in the Huai Kha Khaeng Wildlife Sanctuary (HKK). The site underwent a widespread, catastrophic disturbance in the mid-1800s and several smaller, more localized disturbances in the 1910s, 1940s, and 1960s (Baker et al., 2005).

Cores were collected between December 2010 and December 2011, sampling trees >5 cm DBH with the goal or representing a random subset of the local population of the target species. Details are given in Vlam et al. (2014).

Smithsonian Conservation Biology Institute, Virginia, USA

Cores were collected within the ForestGEO plot at the Smithsonian Conservation Biology Institute (SCBI). The forest is a secondary temperate broadleaf deciduous forest, which developed following agricultural abandonment in the mid 19th-century, dominated by the species included in our analysis (Bourg et al., 2013). Specifically, the 14 species sampled together account for 97% of woody productivity at the site (Helcoski et al., 2019).

In 2010-2011, cores were collected from a random subset of live trees ≥ 10 cm DBH. In 2016 and 2017, cores were extracted from trees found newly dead during an annual tree mortality census (Gonzalez-Akre et al., 2016). Details are given in Helcoski et al. (2019).

Lilly Dickey Woods, Indiana, USA

Lilly Dickey Woods (LDW) is a secondary temperate broadleaf deciduous forest dominated by oaks (*Quercus* spp.) and hickories (*Carya* spp.).

Cores were collected outside the ForestGEO plot, but within a contiguous patch of forest. In 2012 - 2014, cores were collected from live or dead dominant canopy trees with morphological characteristics typical of older trees (Maxwell et al., 2016). In 2020, additional cores were collected following an ecological study design, wherein all live trees $\geq \# \#$ cm within a (**SIZE**) plot were sampled.

Harvard Forest, USA

Harvard Forest (HF) is a secondary temperate mixed forest dominated by *Tsuga canadensis* and northern hardwood species including *Quercus rubra*, *Acer rubrum*, and *Betula alleghaniensis*. Cores were collected within the ForestGEO megaplot, and in the footprint of the original HF eddy-flux tower (Finzi et al., 2020). Samples were collected following an ecological study design (Dye et al., 2016), wherein all living or dead trees ≥ 10 cm DBH within a (**SIZE**) plot were cored.

Žofín Forest Dynamics Plot, Czech Republic

The Žofín forest (ZOF) is a well-preserved natural forest remnant dominated by *Fagus sylvatica* L., *Picea abies* L. and *Abies alba* Mill. The forest is not fully without past human direct interventions, and a limited

historical land use effect is also possible (see Kozáková et al., 2011). Acid deposition dramatically reduced growth in the late 20th century, with peak influence between the 1970s and the early 1990s (Elling et al., 2009; Pavel Šamonil & Vrška, 2008).

In total, 2210 individuals were cored either within the 25 ha ForestGEO plot or a larger, 74 ha plot in which it is embedded. The tree-ring data were collected for several studies around 2010 (Kašpar et al., in review; P. Šamonil et al., 2016, 2014; Pavel Šamonil et al., 2015, 2013; Vašíčková et al., 2019, 2016). The sampling strategy was mainly connected with the disturbance history of the forest and evaluation of growth of juvenile trees in gaps. Therefore, these data consist mainly of dominant and codominant tree species and relatively low number of young trees.

Niobrara, Nebraska, USA

The Niobrara site sits at the prairie-forest ecotone of the North American Great Plains. There, forests occur in cool, moist canyons formed by spring-fed tributaries along the Niobrara River. Cores were taken from seven north-facing *Betula papyrifera* stands along a 27 km section of the Niobrara River, as detailed in Bumann et al. (2019). The largest healthy trees within each stand were selected for coring.

Little Tesuque, New Mexico, USA

The Little Tesuque (LT) site is in a mature dry mixed conifer forest outside of Santa Fe, NM, in the foothills of the Sangre de Cristo Mountains. The site had not undergone stand-clearing disturbance (e.g., fire) in more than one hundred years. The growth of trees in the region, including at this site, are being severely affected by a strong drying trend under climate change (Touchan et al., 2011; Williams et al., 2013), with many missing growth rings in recent years.

In 2020, live canopy and sub-canopy trees, all >20 cm DBH, were sampled within a 1 ha plot (Little Tesuque plot 3; *lts3*).

Cedar Breaks, Utah, USA

Cores were collected within the Utah Forest Dynamics Plot ForestGEO plot on the Colorado Plateau in Cedar Breaks National Monument [CB; Furniss et al. (2017)]. The plot sits on the edge of cliff, which descends ~ 750 m to a valley below. The mature spruce-fir forest is dominated by the species analyzed here (*Abies bifolia*, *Populus tremuloides*, *Picea engelmannii*, *Pinus flexilis*, *Pinus longaeva*, *Picea pungens*, and *Pseudotsuga menziesii*). The site is largely undisturbed. The most recent fire occurred in 1802, and many currently living trees established before then. Living *Pinus longaeva* at the site date back ~ 1600 years, and deadwood at the site dates back to 0 AD (Cooper & Lutz, unpublished data).

In 2019, living individuals of each dominant species were cored.

Chronologies are published on ITRDB (Birch et al., 2020a, 2020b, 2020c, 2020d).

Scotty Creek, Northwest Territories, Canada

The Scotty Creek site is a black spruce (*Picea mariana*) forest on rapidly thawing discontinuous permafrost (Dearborn et al., 2020; Sniderhan & Baltzer, 2016). Vertical permafrost thaw has been causing drought stress in the shallow-rooted trees, resulting in growth declines (Sniderhan & Baltzer, 2016) and high mortality (Dearborn et al., 2020).

In the summers of 2012 and 2013, seven forest stands within a 2 km^2 area were sampled. In five stands with clearly defined boundaries at edges of permafrost plateaus, all living and dead trees ≥ 7 cm DBH were cored. In two stands without well-defined edges, cores were taken from a ≥ 7 cm DBH tree nearest to every 20 m interval in a 100×100 m grid, totaling 36 trees per stand. Sampling details are given in Sniderhan & Baltzer (2016).

Appendix S2. Methods for reconstruction of DBH

Tree diameter at breast height (or height of coring), DBH , was reconstructed over the time span for which a core record existed. DBH was reconstructed either from the outside in or from the inside out. We gave precedence to the outside-in approach; that is, when a recent DBH measurement was available, DBH was reconstructed from the outside in. In cases where DBH was not available, but when we knew that the core hit pith or could reasonably estimate how far off it was based on the curvature of the rings (Applequist, 1958; Duncan, 1989), DBH was reconstructed from the inside out.

The outside-in approach to DBH reconstruction started with a recent DBH measurement, DBH_m , where reference measurement year m is often but not necessarily at the time of coring. DBH for each year (y) of interest, Y , was then estimated using the following equation:

$$DBH_Y = DBH_m - 2 * \left[r_{bark,m} - r_{bark,Y} + \sum_{y=Y}^m RW_y \right]$$

Here, r_{bark} denotes bark thickness, which was estimated on a species-specific basis from allometries (Tables S2, S4). If DBH_m was taken before coring, RW values between $y = m$ and $y = Y$ were added instead of subtracted. If DBH_m was taken after coring, *... (check code)

In some cases, negative values of DBH_Y were predicted for the earliest years in the core record; that is, the sum of RW from the earliest year in the core record to year m , plus the predicted change in r_{bark} , was greater than half of DBH_m . Such cases could occur due to a measurement or data error, or if the tree's growth was asymmetrical around the pith, as commonly occurs (Speer, 2010). In cases where the error was egregious – i.e., where predicted DBH_Y of the earliest year in the record divided by DBH_m was < -0.5 – we removed the tree from the analysis. We assumed that smaller errors were attributable to asymmetrical growth, and re-distributed the error evenly across years so that DBH_Y prior to the first year in the core was zero. This correction was applied only to DBH_Y , and not to any RW records.

When a measurement of DBH_m was not available, and when the core hit pith or the distance to pith could be reliably estimated, DBH was reconstructed from the inside-out. Specifically, DBH for each year (y) of interest, Y , was estimated using the following equation:

$$DBH_Y = 2 * \left[r_{bark,Y} + \sum_{y=0}^Y RW_y \right]$$

Again, r_{bark} was estimated on a species-specific basis from allometries (Tables S2, S4).

When there was more than one core for a tree, the DBH reconstructions from each core were averaged to produce a single estimate of the tree's DBH through time. When the start or end dates of the records from the cores differed, we extrapolated growth of the shorter core to match the years covered by the longer core. Specifically, to fill in years at the more recent end, we assumed that the average growth rate of the ten years prior to the missing records applied to the missing years. To fill in years at the beginning of the tree's lifespan, we likewise assumed that the ten years adjacent to the missing record applied to the missing years; however, if this yielded a negative DBH estimate for the earliest year in the reconstruction, we divided the existing minimum DBH by number of years missing and applied that value to each year. We note again that these reconstructed growth records were used only for the reconstruction of DBH and were not included as response variables in any of our analyses.

Regardless of the DBH reconstruction approach (outside-in or inside-out), accurate reconstructions require accounting for r_{bark} , particularly for species that can attain very thick bark (e.g., *Pseudotsuga menziesii*, *Pinus ponderosa*). For the majority of species, including all thick-barked species, we assigned allometries relating r_{bark} to DBH , which were constructed for the species of interest or a related species (Tables S2, S4). When raw data on bark thickness data were available, we generated species-specific lognormal scaling relationships with the intercept forced to zero (Table S4). When raw bark thickness data were not available, we applied published bark allometries from other sources (Table S4).

Appendix S3. Methods for climate data evaluation and correction

Monthly climate data for 1901-2019 were obtained from CRU v.4.04 (I. Harris et al., 2014; Ian Harris et al., 2020), and in a few cases corrected based on more local records. For BCNM, we calculated monthly *PPT* and *PDF* from daily precipitation readings made on Barro Colorado Island starting in 1929 (Paton, 2019) and used these to replace the corresponding CRU records.

Additionally, we used 800 m resolution PRISM records (Daly et al., 2015, 2008) from 1930 to 2015 to test and correct for cases where the coarser-resolution CRU values were not locally representative. Variables in the PRISM data set included T_{max} , T_{mean} , T_{min} , and *PPT*. To test for substantial differences between CRU and PRISM records, each variable was compared on a monthly basis using linear regression. We considered CRU records to be inappropriate if (1) a paired t-test revealed a significant difference between CRU and PRISM records, and (2) the absolute value of the mean monthly difference between CRU and PRISM exceeded 2.5°C (temperature variables) or 10 mm per month (precipitation). Two sites met these criteria: LT and CB, both located in mountainous terrain in the western United States. For these sites, we used linear regression to characterize the relationship between the CRU and PRISM, and then used this relationship to correct CRU data outside the time frame of PRISM (i.e., pre-1930 and post-2015). CRU records were replaced with PRISM records over the time frame for which they were available. For these sites, CRU records for variables not included in the PRISM data set (*PDF*, *PET*) were considered unreliable and excluded from the analysis.

Appendix S4. Methods for comparing our approach with traditional methods

To test whether our methods gave similar results to traditional methods, we conducted qualitative comparisons of our results to previous studies based on the same cores (Table S5) and conducted a formal quantitative comparison for four species (Figs. S11-S14), as detailed below.

Qualitative comparison

For all species-site combinations, we reviewed previous studies characterizing the climate sensitivity of growth using conventional methods. In most cases, we were able to compare with previous studies from the same sites and sets of cores. When these were not available, we reviewed regional-level analyses believed to be representative of the site.

Results from previous studies were compiled alongside results from the climate-only model in this study (Table S5). Where previous studies examined numerous climate variables or time windows (e.g., Helcoski et al., 2019), we focus on those most relevant to our findings.

Beyond the methodological differences, original studies based on the same sets of cores varied from this one and from one another in factors including the exact set of cores analyzed, climate data sources, time frame of analysis, approaches to identifying candidate climate variables and windows (including whether this is done on a site or species level), methods for detrending and standardizing to build chronologies, and whether the effects of temperature and precipitation are considered separately (original studies) or additively (this study). To standardize for such differences, we selected a subset of species for a standardized quantitative comparison, as detailed below.

Quantitative comparison

We also conducted a formal comparison of our approach to conventional methods using identical tree-ring and climate data for four species: *Liriodendron tulipifera* at SCBI, *Abies alba* at Zof, *Pseudotsuga menziesii* at CB, and *Picea mariana* at SC (Figs. S11-S14). These species were selected for analysis because they have been well-studied in the past. For each species, we compared climate sensitivities for the top precipitation- and temperature- group variables, as identified in the main analysis.

Prior to analysis, data were prepared and cleaned as described in the Methods section, resulting in an identical set of records for input into each analysis. For the approach developed here, analysis was conducted as described in the Methods section, but with the *climwin* climate variable selection process limited to just the species of interest (as opposed to all species at the site), climate variables considered individually rather than additively, analysis of only first-order linear relationships, and with start date adjusted to match the conventional method (see below). *Climwin* is a useful analytical tool that automates the process of running and comparing numerous regressions, but its use does not alter results relative to what would be obtained via a more conventional approach; numerous climate drivers and time windows can be compared without *climwin* (e.g., REFS), and *climwin* can also be used on residual chronologies. Following the *climwin* analysis step, we extracted *beta* coefficients describing the slope of the relationship between climate and *RW*. *Beta* coefficients, along with their standard error, were obtained for each month within the analysis time frame (Table S1) and for the time window identified as optimal by *climwin*.

For the analysis using conventional methods, the ring-width series from each core was standardized via ARSTAN using a 2/3rds n spline, where n is the number of years in the series (Edward Roger Cook, 1985; E. R. Cook & Kairiukstis, 1990). We used the adaptive power transformation (Edward R. Cook & Peters, 1997) to reduce the influence of outliers and stabilize the variance over time. Next, to adjust for changes in variance as series replication decreased towards the earlier portion of each chronology, we stabilized each series using either the average correlation between raw ring-width series (*rbar*) method or a 1/3rds spline method (Jones et al., 1997). We applied the 1/3rds spline method when replication in the inner portion of each chronology (~30–50 yrs, depending on full chronology length) dropped below three trees. Next, we calculated a robust biweight mean chronology for each species from the ring-width indices (Edward Roger Cook, 1985). We used residual chronologies because the autoregressive standardization process in creating them removes much of the tree-level autocorrelation in growth, such that these chronologies would be expected to contain the most conservative information on interannual growth drivers (Edward Roger Cook, 1985).

We defined chronology start dates according to the subsample signal strength (SSS), using a cutoff of SSS = 0.80 (or 80% of the population signal). Thus, for this analysis only, we defined chronology start dates as the year the SSS exceeded 0.80 or two years after the start of the climate record, whichever came later. SSS exceeded 0.80 well before the start of the 1901 start of climate records for *Pseudotsuga menziesii* (1800s), *Abies alba* (1700), and *Picea mariana* (1850s). For *Liriodendron tulipifera*, SSS reached 0.8 with 11 trees in 1919, which we used as the start date for this series. We note that these start date criteria differ from those used in the main analysis (Table S3), which had earlier start dates because the analysis was not constrained by a need to represent the full population signal. End dates were defined as the last full year prior to sampling (Table S3), or 2007 for CB.

Beta (slope) coefficients for the relationship between tree growth and the monthly climate variable were derived as in Helcoski et al. (2019). Briefly, we used the R packages *dplR* (Bunn, 2008) and *bootRes* (Zang & Biondi, 2013) to analyze relationships between *RW* and monthly climate following the bootstrapping methodology of (Biondi & Waikul, 2004). Pearson correlations between climate variables and tree-ring chronologies were converted to linear slopes using the method of Charney et al. (2016).

Finally, we generated plots comparing month-by-month *beta* coefficients describing climate sensitivity, and also comparing *beta* coefficients for the window identified as optimal by *climwin* Figs. S11-S14).

We note that despite designing the analyses to be as comparable as possible, one-to-one correspondence of *beta* coefficients is not necessarily expected for several reasons. First, although the analysis time frame is standardized between the two approaches, the relative influence of each year will generally vary between the two approaches. The traditional approach, which all cores into a single residual chronology with one value per year, gives equal weighting to each year. In contrast, under the approach developed here, the number of records per year can vary across the analysis time frame, generally increasing over time as the younger trees enter the analysis. Thus, particularly when many younger trees are included in the analysis, the two approaches will effectively apply different weighting schemes to the years of the analysis period. In cases where climate-sensitivity differs between old and young trees, or where the climate and/or climate response changed substantially over the analysis time frame [e.g., at Scotty Creek; Fig. S14; Sniderhan & Baltzer (2016)], this may lead to divergence of the climate sensitivities estimated by the two methods.

Second, traditional analysis methods (using ARSTAN) were primarily designed to distill population-level variation to obtain the strongest possible climate signal for the reconstruction of past climate (E. R. Cook & Kairiukstis, 1990), not to characterize climate responses on the individual level, where variation is inherently higher. While conversion of Pearson correlations to linear slopes *sensu* Charney et al. (2016) approximates climate responses, it does not provide an exact slope describing the relationship between individual-level or population mean growth and climate. This is because standardization of variance and averaging of individual-level residuals prior to the climate analysis fundamentally alters and obfuscates individual-level responses.

We suspect that both of these factors may underlie the tendency for the traditional method to estimate stronger climate sensitivity than the approach developed here for Scotty Creek (Fig. S14), a comprehensively sampled black spruce forest (i.e., including young trees) on melting permafrost. We note, however, that there were no statistically significant differences in the *beta* coefficients of the two approaches at this site.

Appendix S5. Dealing with rapidly changing climate and tree growth

ISSUE #25 in ForestGEO-climate-sensitivity

Our analysis included two sites where climate change has had pronounced effects on tree growth: Little Tesuque, New Mexico, USA (LT) and Scotty Creek, NW Territories, Canada (SC). At LT, increasingly warm drought has dramatically reduced growth (Touchan et al., 2011; Williams et al., 2013), resulting in many missing rings in recent years. At SC, rapidly rising temperatures are causing melting permafrost, summer moisture stress, resulting in negative growth trends in basal area index (*BAI*) starting around 1950 and significant growth declines since 1970 in 56% of trees (Sniderhan & Baltzer, 2016).

Problematically, correlating tree growth residuals from which climate-driven trends had been removed against a climate signal with a strong directional trend would not necessarily identify the most relevant climate drivers (step 1 in Fig. 1). To explore whether selection of climate driver variables was strongly affected by directional trends in climate, we experimented with three different approaches to identifying the most important climate drivers at three sites: LT, SC, and SCBI (where the climate has not changed strongly). The first approach was the baseline method described in the Methods and presented in throughout the manuscript, where detrended growth residuals were correlated with raw climate data (step 1 in Fig. 1).

The second approach involved detrending the climate variables using a GAM with automated selection of the number of knots prior to the *climwin* step. Thus, this approach correlates growth anomalies to climate anomalies around a more slowly changing mean, and using it to select climate driver variables inherently assumes that the most important climate drivers of high-frequency (annual) growth variation are also the most important drivers of longer-term growth changes in response to changing climate. For *PPT* at LT, this approach and our baseline method identified identical time windows for all growth metrics. For the temperature variable at LT, this approach and our baseline method consistently identified *T_{max}* as the most important variable, but selected slightly different time windows with *RW* the response metric (May-July for baseline method, April-July when *T_{max}* was detrended). For the water variable at SC, the two methods identified identical climate drivers (previous May or June - previous August *PPT*, depending on growth metric but not the analysis method). For the temperature variable at SC, the methods identified different variables and windows, with the baseline method selecting July *T_{max}* and the detrending method selecting previous December *T_{mean}* (which makes little sense biologically). For the water variable at SCBI, this approach and our baseline method consistently identified previous June- current August *PPT* as the strongest climate driver, with the exception that current May-August came out as the strongest driver in the detrended analysis for ΔAGB . For the temperature variable at SCBI, results were somewhat different, with this approach identifying *T_{max}* as the most important variable, and the baseline approach identifying *PET*. Both identified time windows within the current growing season when *RW* was the metric, but time windows were not similar when *BAI* or *AGB* was the metric. Given little meaningful difference between these approaches, and no clear advantage of detrending the climate variable, we preferred the baseline method.

The third approach involved splitting analyses into decades before and after 1970 (*sensu* Sniderhan & Baltzer, 2016) – an approach that has also been applied in other studies in rapidly warming climates (Driscoll et al., 2005; Wilmking et al., 2004; e.g., **lloyd_no_2002?**). This approach should accurately capture the most important climatic drivers of growth variation prior to the acceleration of climate change in recent decades, and should also identify the drivers of recent high-frequency growth variation. For *PPT* at LT, optimal time windows pre-1970 and post-1970 were similar to those for the entire time period. For the temperature variable at LT, *T_{max}* was consistently identified as the most important variable, but its optimal time window extended back to the previous growing season pre-1970, but was limited to the current growing season post-1970 and for the analysis as a whole. For the water variable at SC, *PPT* was consistently selected as a better predictor than *PDF*, and responses pre- and post-1970 were generally similar to those over the full time period. For the temperature variable at SC, the pre- and post- 1970 time periods both identified *T_{min}* temperatures during a single month in the previous summer as the optimal climate driver for *RW*, whereas the analysis for the full time period identified *T_{max}* of current July (Fig. S55). For the water variable at SCBI, *PPT* was consistently selected as a better predictor than *PDF*, with similar time windows pre-1970 and for the full analysis period, compared to only a weak effect over a different time period (current May) post-1970 (Fig. S55). For the temperature variable at SCBI, selected variables (*PET*, *T_{max}*, or *T_{mean}*) and time windows

were variable across the three analysis periods, with only weak relationships in the post-1970 analysis period. These results indicate potentially shifting climate sensitivities, particularly at SC (Fig. S55), which may not be adequately captured by our baseline method. Further analysis into how climate sensitivities may be shifting would be valuable, but is beyond the scope of this analysis.

While we determined that our baseline method was suitable for the current analysis, we note that it remains problematic in that detrending of growth sequences ahead of identification of climate drivers precludes the possibility of the analysis capturing the climatic drivers of low-frequency growth changes. The ideal solution would likely be to avoid any type of detrending of growth sequences, but rather to use full GLS models (as in step 2 in Fig. 1) to assess the explanatory power of potential climate variables, but this would be computationally time-consuming and is beyond the scope of the current analysis.

Table S1. Site Details.

site code	site name	latitude*	longitude*	elevation (m.a.s.l.)	cores within ForestGEO plot?	canopy positions	tree statuses	date range	dormant season**	months in climwin
BCNM	Barro Colorado Nature Monument	9.15430	-79.8461	<160	no	canopy	live, dead	1931-2014	Nov-Apr	pOct-cDec
HKK	Huai Kha Khaeng	15.63240	99.2170	550	no	all	live	1903-2011	Nov-Apr	pOct-cDec
SCBI	Smithsonian Conservation Biology Institute	38.89350	-78.1454	273-338	yes	all	live, dead	1903-2017	Oct-Mar	pMay-cAug
LDW	Lilly Dickey Woods	39.23590	-86.2181	230-303*	no	canopy	live, dead	1903-2019	Oct-Mar	pMay-cAug
HF	Harvard Forest	42.53880	-72.1755	340-368*	yes	all	live, dead	1903-2014	Oct-Mar	pMay-cAug
ZOF	Žofín Forest Dynamics Plot	48.66380	14.7073	736-829*	some	all	live, dead	1903-2013	Oct-Mar	pMay-cAug
NIO	Niobrara	42.78000	-100.0210	644-702*	no	canopy	live	1948-2015	Oct-Apr	pMay-cAug
LT	Little Tesuque	35.73838	-105.8382	2684 - 2702	n.a.	canopy/ sub- canopy	live	1903-2018	Oct-Apr	pMay-cAug
CB	Utah Forest Dynamics Plot	37.66150	-112.8525	3020-3169	yes		live	1903-2007	Oct-Apr	pMay-cAug
SC	Scotty Creek	61.30000	-121.3000	280	no	all	live, dead	1903-2013	Sept-Apr	pMay-cAug

*Refers to ForestGEO plot (exception: LT) and is not necessarily the most accurate value for exact locations at which cores were taken. Geographic coordinates were used to extract climate data from CRU.

**Refers to approximate period during which woody growth ceases (dry season in the tropics, winter for temperate and boreal sites).

Table S2. Species analyzed, their characteristics, and bark allometries applied.

species code	family	latin name	sites sampled	leaf type	leaf phenology	light requirements*	bark allometry**
ABAL	Pinaceae	<i>Abies alba</i>	ZOF	needleleaf	evergreen	shade-tolerant	2
ABBI	Pinaceae	<i>Abies bifolia</i>	CB	needleleaf	evergreen	shade-tolerant	2
ACRU	Sapindaceae	<i>Acer rubrum</i>	HF	broadleaf	deciduous (cold)	intermediate	3
ACSA	Sapindaceae	<i>Acer saccharum</i>	LDW	broadleaf	deciduous (cold)	shade-tolerant	3
AFXY	Fabaceae	<i>Afzelia xylocarpa</i>	HKK	broadleaf	deciduous (drought)	light-demanding	neglected
BEAL	Betulaceae	<i>Betula alleghaniensis</i>	HF	broadleaf	deciduous (cold)	intermediate	4
BEPA	Betulaceae	<i>Betula papyrifera</i>	NIO	broadleaf	deciduous (cold)	light-demanding	5
CACO	Juglandaceae	<i>Carya cordiformis</i>	SCBI	broadleaf	deciduous (cold)	light-demanding	6
CAGL	Juglandaceae	<i>Carya glabra</i>	SCBI	broadleaf	deciduous (cold)	intermediate	7
CAOV	Juglandaceae	<i>Carya ovata</i>	LDW	broadleaf	deciduous (cold)	intermediate	7
CAOVL	Juglandaceae	<i>Carya ovalis</i>	SCBI	broadleaf	deciduous (cold)	intermediate	8
CATO	Juglandaceae	<i>Carya tomentosa</i>	SCBI	broadleaf	deciduous (cold)	light-demanding	9
CHTA	Meliaceae	<i>Chukrasia tabularis</i>	HKK	broadleaf	brevi-deciduous (drought)	intermediate	neglected
FAGR	Fagaceae	<i>Fagus grandifolia</i>	HF, SCBI	broadleaf	deciduous (cold)	shade-tolerant	neglected
FASY	Fagaceae	<i>Fagus sylvatica</i>	ZOF	broadleaf	deciduous (cold)	shade-tolerant	neglected
FRAM	Oleaceae	<i>Fraxinus americana</i>	LDW, SCBI	broadleaf	deciduous (cold)	intermediate	10
FRNI	Oleaceae	<i>Fraxinus nigra</i>	SCBI	broadleaf	deciduous (cold)	intermediate	10
JACO	Bignoniaceae	<i>Jacaranda copaia</i>	BCNM	broadleaf	deciduous (drought)	light-demanding	11
JUNI	Juglandaceae	<i>Juglans nigra</i>	SCBI	broadleaf	deciduous (cold)	light-demanding	12
LITU	Magnoliaceae	<i>Liriodendron tulipifera</i>	LDW, SCBI	broadleaf	deciduous (cold)	light-demanding	13
MEAZ	Meliaceae	<i>Melia azedarach</i>	HKK	broadleaf	deciduous (drought)	light-demanding	neglected
PIAB	Pinaceae	<i>Picea abies</i>	HF, ZOF	needleleaf	evergreen	shade-tolerant	14
PIEN	Pinaceae	<i>Picea engelmannii</i>	CB	needleleaf	evergreen	shade-tolerant	14
PIFL	Pinaceae	<i>Pinus flexilis</i>	CB	needleleaf	evergreen	light-demanding	17
PILO	Pinaceae	<i>Pinus longaeva</i>	CB	needleleaf	evergreen	light-demanding	neglected
PIMA	Pinaceae	<i>Pincea mariana</i>	SC	needleleaf	evergreen	shade-tolerant	15
PIPO	Pinaceae	<i>Pinus ponderosa</i>	LT	needleleaf	evergreen	light-demanding	16
PIPU	Pinaceae	<i>Pincea pungens</i>	CB	needleleaf	evergreen	intermediate	14
PIST	Pinaceae	<i>Pinus strobus</i>	HF, SCBI	needleleaf	evergreen	intermediate	18
PIST3	Pinaceae	<i>Pinus strobiformis</i>	LT	needleleaf	evergreen	light-demanding	17
POTR	Salicaceae	<i>Populus tremuloides</i>	CB	broadleaf	deciduous (cold)	light-demanding	19
PSME	Pinaceae	<i>Pseudotsuga menziesii</i>	CB	needleleaf	evergreen	intermediate	20
QUAL	Fagaceae	<i>Quercus alba</i>	LDW, SCBI	broadleaf	deciduous (cold)	intermediate	21
QUMO	Fagaceae	<i>Quercus montana</i>	LDW, SCBI	broadleaf	deciduous (cold)	intermediate	22
QURU	Fagaceae	<i>Quercus rubra</i>	HF, LDW, SCBI	broadleaf	deciduous (cold)	intermediate	23
QUVE	Fagaceae	<i>Quercus velutina</i>	LDW, SCBI	broadleaf	deciduous (cold)	intermediate	24
TEPA	Burseraceae	<i>Tetragastris panamensis</i>	BCNM	broadleaf	evergreen	shade-tolerant	25
TOCI	Meliaceae	<i>Toona ciliata</i>	HKK	broadleaf	deciduous (drought)	intermediate	neglected
TRTU	Meliaceae	<i>Trichilia tuberculata</i>	BCNM	broadleaf	evergreen	shade-tolerant	26
TSCA	Pinaceae	<i>Tsuga canadensis</i>	HF	needleleaf	evergreen	shade-tolerant	27

*For extratropical species, light requirements are classified based on the database of Niinemets & Valladares (2006). For tropical species, categorization is based on Alfaro-Sánchez et al. (2017) for BCNM and Vlam et al. (2014) for HKK.

**Bark allometry field indicates the species and site sampled to construct the bark allometry. When neither raw data nor an allometric equation for the study species was available, we selected the most appropriate equation that could be located for similar species. Equations are given in Table S4.

Table S3. Sampling details for species by site.

site	species code	all		with DBH		DBH range		date range
		n trees	n cores	n trees	n cores	sampled	reconstructed*	
BCNM	JACO	12	18	11	17	30.2-63.5	2.6-56.4	1931-2014
BCNM	TEPA	18	29	17	26	22.1-59.5	2.7-49.4	1931-2014
BCNM	TRTU	23	37	20	31	20.7-43.6	4.8-41.5	1931-2014
CB	ABBI	22	41	20	39	13.9-54.2	0-50.4	1903-2019
CB	PIEN	14	23	12	20	14-54.9	2.2-43.4	1903-2019
CB	PIFL	13	21	12	20	17.6-64.1	4.5-58.5	1903-2018
CB	PILO	17	25	7	11	45.8-63.6	35.4-57.5	1903-2019
CB	PIPU	16	29	15	28	22.4-50.8	8.6-50.5	1903-2019
CB	POTR	17	27	17	27	23.6-47.6	7.7-44.5	1903-2019
CB	PSME	11	21	11	21	10.6-64.2	2.6-63.3	1903-2019
HF	ACRU	18	59	18	59	10.1-22.1	0.9-20.4	1903-2013
HF	BEAL	13	44	13	44	10.2-37.9	1.6-20.5	1904-2013
HF	QURU	74	180	73	177	19.5-53	1.1-48.3	1903-2014
HF	TSCA	32	83	32	83	10.6-37	0.6-33.5	1923-2014
HKK	AFXY	39	127	39	127	20.1-98.7	0.1-81.4	1903-2011
HKK	CHTA	28	70	28	70	16-64.6	0.2-59.5	1904-2010
HKK	MEAZ	46	130	46	130	25.6-98.1	3.8-80.3	1914-2011
HKK	TOCI	45	143	45	143	16.6-116.4	1.7-80.5	1903-2011
LDW	ACSA	35	66	34	64	9-64.6	0-52.4	1903-2019
LDW	CAOV	9	18	8	16	unknown	0.6-37.4	1903-2013
LDW	LITU	15	28	14	26	unknown	1.2-69.4	1903-2019
LDW	QUAL	10	20	0	0	NA	NA	1903-2013
LDW	QUMO	10	20	8	16	unknown	1.1-52.4	1903-2013
LDW	QUVE	9	18	0	0	NA	NA	1903-2013
LT	PIPO	10	20	10	20	23.2-52.8	14.6-48.4	1903-2018
LT	PIST3	7	14	7	14	25.7-39.8	4.2-34.4	1903-2018
NIO	BEPA	42	138	42	138	unknown	0.4-33.5	1948-2015
SCBI	CACO	15	15	15	15	10.62-38.52	1.6-32.2	1903-2015
SCBI	CAGL	39	39	36	36	10.28-52.31	1.6-49.3	1903-2015
SCBI	CAOVL	25	25	24	24	15.11-60.32	2.6-47.2	1903-2015
SCBI	CATO	15	15	14	14	12.86-35.95	3.7-28.4	1903-2015
SCBI	FAGR	76	76	76	76	10.05-41.02	0.1-41.2	1920-2009
SCBI	FRAM	66	66	63	63	6.85-94.73	0.1-84.4	1903-2016
SCBI	FRNI	12	12	12	12	11.04-39.2	0.5-27.3	1903-1996
SCBI	JUNI	30	30	29	29	20.4-76.19	4.6-59.5	1903-2010

(continued)

site	species code	all		with DBH		DBH range		date range
		n trees	n cores	n trees	n cores	sampled	reconstructed*	
SCBI	LITU	106	106	105	105	10-91.42	0.1-81.1	1903-2010
SCBI	PIST	36	36	36	36	13.92-50.96	0.5-44.3	1931-2010
SCBI	QUAL	66	66	66	66	11.4-76.73	0.3-70.4	1903-2009
SCBI	QUMO	67	67	67	67	10.22-84.59	0.3-69.5	1903-2017
SCBI	QURU	70	70	70	70	11.07-87.65	2.5-79.2	1903-2016
SCBI	QUVE	81	81	81	81	16.02-82.33	0.5-78.4	1903-2009
SC	PIMA	443	443	395	395	7-24	0-16.4	1903-2013
ZOF	ABAL	46	46	46	46	50-121	21.1-107.4	1903-2010
ZOF	FASY	1369	1369	1369	1369	unknown	0.1-115.3	1903-2013
ZOF	PIAB	644	644	642	642	unknown	0-125.4	1903-2011

*Maximum reconstructed DBH's analyzed are less than maximum sampled DBH's because we discard size ranges with < 3 conspecific trees.

Table S4. Allometric equations for bark thickness.

species	equation	source	n	DBH.range.cm	site	source.1
<i>Abies alba</i>	$bark.mm = ((0.05 + 0.06 * (dbh.cm/2.54))/2) * 2.54$	equation	NA		North America	Miles, Patrick D.; Smith, W. Brad. 2009.
<i>Acer pseudoplatanus</i>	$bark.mm = 0.619 * \log(dbh.cm + 1)$	data	10	8.2-39.6	SCBI	Anderson-Teixeira et al. (2015)
<i>Betula alleghaniensis</i>	$bark.mm = ((0.15 + 0.03 * (dbh.cm/2.54))/2) * 2.54$	equation	NA		North America	Miles, Patrick D.; Smith, W. Brad. 2009.
<i>Betula papyrifera</i>	$bark.mm = ((0.13 + 0.05 * (dbh.cm/2.54))/2) * 2.54$	equation	NA		North America	Miles, Patrick D.; Smith, W. Brad. 2009.
<i>Carya cordiformis</i>	$bark.mm = 0.793 * \log(dbh.cm + 1)$	data	9	5.9-68.2	SCBI	Anderson-Teixeira et al. (2015)
<i>Carya glabra</i>	$bark.mm = 1.035 * \log(dbh.cm + 1)$	data	8	19.1-78	SCBI	Anderson-Teixeira et al. (2015)
<i>Carya ovalis</i>	$bark.mm = 1.531 * \log(dbh.cm + 1)$	data	8	6.4-63.1	SCBI	Anderson-Teixeira et al. (2015)
<i>Carya tomentosa</i>	$bark.mm = 1.105 * \log(dbh.cm + 1)$	data	8	5-57.3	SCBI	Anderson-Teixeira et al. (2015)
<i>Fraxinus americana</i>	$bark.mm = 2.223 * \log(dbh.cm + 1)$	data	9	6.1-94.2	SCBI	Anderson-Teixeira et al. (2015)
<i>Jacaranda copaia</i>	$bark.mm = 2.993 * \log(dbh.cm + 1)$	data	5	45.6-75	Panama	Raquel Alfaro-Sánchez (unpublished data)
<i>Juglans nigra</i>	$bark.mm = 2.107 * \log(dbh.cm + 1)$	data	9	13.6-85.4	SCBI	Anderson-Teixeira et al. (2015)
<i>Liriodendron tulipifera</i>	$bark.mm = 1.637 * \log(dbh.cm + 1)$	data	9	27.5-136.5	SCBI	Anderson-Teixeira et al. (2015)
<i>Picea abies</i>	$bark.mm = ((0.15 + 0.04 * (dbh.cm/2.54))/2) * 2.54$	equation	NA		North America	Miles, Patrick D.; Smith, W. Brad. 2009.
<i>Picea mariana</i>	$bark.mm = 3.726 * \log(dbh.cm + 1)$	data	12	6.9-7.9	Scotty Creek	Rajit Patankar and Jennifer Baltzer (unpublished data)
<i>Pinus flexilis</i>	$bark.mm = (1.299 * \sqrt{(dbh.cm)^{0.609}})^2$	equation	29	10-130	California (3 montane sites)	Zeibig-Kichas et al. (2016)
<i>Pinus ponderosa</i>	$bark.mm = (1.298 * \sqrt{(dbh.cm)^{0.802}})^2$	equation	81	5-160	California (4 montane sites)	Zeibig-Kichas et al. (2016)
<i>Pinus strobus</i>	$bark.mm = ((0.02 + 0.10 * (dbh.cm/2.54))/2) * 2.54$	equation	NA		North America	Miles, Patrick D.; Smith, W. Brad. 2009.
<i>Populus tremuloides</i>	$bark.mm = ((0.10 + 0.07 * (dbh.cm/2.54))/2) * 2.54$	equation	NA		North America	Miles, Patrick D.; Smith, W. Brad. 2009.
<i>Pseudotsuga menziesii</i>	$bark.mm = (0.785 * \sqrt{(dbh.cm)})^2$	equation	30	10-200	California (3 montane sites)	Zeibig-Kichas et al. (2016)
<i>Quercus alba</i>	$bark.mm = 1.828 * \log(dbh.cm + 1)$	data	10	9.3-101.8	SCBI	Anderson-Teixeira et al. (2015)
<i>Quercus montana</i>	$bark.mm = 2.083 * \log(dbh.cm + 1)$	data	8	5.8-99.1	SCBI	Anderson-Teixeira et al. (2015)
<i>Quercus rubra</i>	$bark.mm = 0.98 * \log(dbh.cm + 1)$	data	10	24.1-143.2	SCBI	Anderson-Teixeira et al. (2015)
<i>Quercus velutina</i>	$bark.mm = 1.394 * \log(dbh.cm + 1)$	data	8	16.2-110.7	SCBI	Anderson-Teixeira et al. (2015)
<i>Tetragastris panamensis</i>	$bark.mm = 1.672 * \log(dbh.cm + 1)$	data	4	22.7-48.8	Panama	Raquel Alfaro-Sánchez (unpublished data)
<i>Trichilia tuberculata</i>	$bark.mm = 1.367 * \log(dbh.cm + 1)$	data	12	21-40.5	Panama	Raquel Alfaro-Sánchez (unpublished data), Pete Kerby-Miller and Helene Muller-Landau (unpublished data)
<i>Tsuga canadensis</i>	$bark.mm = ((0.18 + 0.08 * (dbh.cm/2.54))/2) * 2.54$	equation	NA		North America	Miles, Patrick D.; Smith, W. Brad. 2009.

For assignments of species as proxies for those with out available bark allometries, see Table S2.

Table S5. Qualitative comparison of results from this study with previous studies employing conventional methods.

species	Precipitation response		Temperature response		reference
	previously observed	observed here	previously observed	observed here	
Barro Colorado Nature Monument, Panama					
JACO	pos. correlation to Apr-Dec <i>PPT</i> (strongest of the 3 species)	pos. correlation to Jan-Dec <i>PPT</i> (strongest of the 3 species)	no sig. correlation to annual T_{mean} or T_{min}	no correlation to Feb-Mar T_{min}	Alfaro-Sánchez et al. 2017
TEPA	pos. correlation to Apr-Dec <i>PPT</i> (response weaker than JACO, similar to TRTU)	pos. correlation to Jan-Dec <i>PPT</i> (response weaker than JACO, similar to TRTU)	no sig. correlation to annual T_{mean} or T_{min}	no correlation to Feb-Mar T_{min}	Alfaro-Sánchez et al. 2017
TRTU	pos. correlation to Apr-Dec <i>PPT</i> (response weaker than JACO, similar to TEPA)	pos. correlation to Jan-Dec <i>PPT</i> (response weaker than JACO, similar to TEPA)	no sig. correlation to annual T_{mean} or T_{min}	non-sig. pos. correlation to Feb-Mar T_{min}	Alfaro-Sánchez et al. 2017
Huai Kha Khaeng, Thailand					
AFXY	sig. pos. correlation with June <i>PPT</i> , otherwise n.s.	pos. correlation to p.Sep-Jun <i>PPT</i> frequency	sig. neg. correlation with T_{max} in Aug and Dec; T_{min} in p.Oct., Jul, Aug	slight pos. correlation to Apr-Oct T_{max}	Vlam et al. 2013
CHTA	sig. pos. correlation with April <i>PPT</i> , otherwise n.s.	no sig. correlation to p.Sep-Jun <i>PPT</i> frequency	sig. neg. correlation with T_{max} in May, Aug-Sept; T_{min} in Feb, May, Aug	neg. correlation to Apr-Oct T_{max}	Vlam et al. 2013
MEAZ	sig. pos. correlation with April <i>PPT</i> , otherwise n.s.	pos. correlation to p.Sep-Jun <i>PPT</i> frequency	sig. neg. correlation with T_{max} in May-Aug; T_{min} in May-Aug	neg. correlation to Apr-Oct T_{max}	Vlam et al. 2013
TOCI	sig. pos. correlation with p.Oct-p.Nov and April-May <i>PPT</i>	pos. correlation to p.Sep-Jun <i>PPT</i> frequency	sig. neg. correlation with T_{max} every month from pOct-June (excluding March); T_{min} in Jan and Mar-Aug	neg. correlation to Apr-Oct T_{max}	Vlam et al. 2013
Smithsonian Conservation Biology Institute, Virginia, USA					
CACO	pos. correlations with May-Aug <i>PPT</i> (sig. May, July)	pos. concave-down correlation to June-Aug <i>PPPT</i>	neg. correlations with May-Aug <i>PET</i> (sig. May-July)	neg. correlation to May-July <i>PET</i>	Helcoski et al. 2019
CAGL	pos. correlations with May-Aug <i>PPT</i> (sig. May)	pos. concave-down correlation to June-Aug <i>PPPT</i>	neg. correlations with May-Aug <i>PET</i> (n.s.)	neg. correlation to May-July <i>PET</i>	Helcoski et al. 2019
CAOVL	pos. correlations with May-Aug <i>PPT</i> (sig. Aug)	pos. concave-down correlation to June-Aug <i>PPPT</i>	neg. correlations with May-Aug <i>PET</i> (sig. all months)	neg. concave-down correlation to May-July <i>PET</i>	Helcoski et al. 2019
CATO	pos. correlations with May-Aug <i>PPT</i> (n.s.)	concave-down correlation to June-Aug <i>PPPT</i>	neg. correlations with May-Aug <i>PET</i> (sig. June)	neg. correlation to May-July <i>PET</i>	Helcoski et al. 2019
FAGR	pos. correlations with May-Aug <i>PPT</i> (sig. July-Aug)	pos. concave-down correlation to June-Aug <i>PPPT</i>	neg. correlations with May-Aug <i>PET</i> (sig. July-Aug)	no correlation to May-July <i>PET</i>	Helcoski et al. 2019
FRAM	pos. correlations with May-Aug <i>PPT</i> (sig. May-June)	pos. concave-down correlation to June-Aug <i>PPPT</i>	neg. correlations with May-Aug <i>PET</i> (sig. May-June)	neg. concave-down correlation to May-July <i>PET</i>	Helcoski et al. 2019
FRNI	no sig. correlations with peak growing season <i>PPT</i>	non-sig. pos. concave-down correlation to June-Aug <i>PPPT</i>	no sig. correlations with peak growing season <i>PET</i>	no correlation to May-July <i>PET</i>	Helcoski et al. 2019
JUNI	pos. correlations with May-Aug <i>PPT</i> (sig. Jun-Aug)	pos. concave-down correlation to June-Aug <i>PPPT</i>	neg. correlations with May-Aug <i>PET</i> (sig. July-Aug)	neg. concave-down correlation to May-July <i>PET</i>	Helcoski et al. 2019

S5, cont.

species	Precipitation response		Temperature response		reference
	previously observed	observed here	previously observed	observed here	
Smithsonian Conservation Biology Institute, Virginia, USA (cont.)					
LITU	pos. correlations with May-Aug <i>PPT</i> (sig. May-July)	pos. concave-down correlation to June-Aug <i>PPPT</i>	neg. correlations with May-Aug <i>PET</i> (sig. all months)	non-sig neg. concave-down correlation to May-July <i>PET</i>	Helcoski et al. 2019
PIST	pos. correlations with May-Aug <i>PPT</i> (n.s.)	pos. concave-down correlation to June-Aug <i>PPPT</i>	neg. correlations with May-Aug <i>PET</i> (n.s.)	no correlation to May-July <i>PET</i>	Helcoski et al. 2019
QUAL	pos. correlations with May-Aug <i>PPT</i> (sig. May)	pos. concave-down correlation to June-Aug <i>PPPT</i>	neg. correlations with May-Aug <i>PET</i> (sig. all months)	non-sig neg. concave-down correlation to May-July <i>PET</i>	Helcoski et al. 2019
QUMO	pos. correlations with May-Aug <i>PPT</i> (sig. May)	pos. concave-down correlation to June-Aug <i>PPPT</i>	neg. correlations with May-Aug <i>PET</i> (sig. May-June, Aug)	non-sig neg. concave-down correlation to May-July <i>PET</i>	Helcoski et al. 2019
QURU	pos. correlations with May-Aug <i>PPT</i> (n.s.)	pos. concave-down correlation to June-Aug <i>PPPT</i>	neg. correlations with May-Aug <i>PET</i> (sig. May, July-Aug)	neg. concave-down correlation to May-July <i>PET</i>	Helcoski et al. 2019
QUVE	pos. correlations with May-Aug <i>PPT</i> (sig. May-July)	pos. concave-down correlation to June-Aug <i>PPPT</i>	neg. correlations with May-Aug <i>PET</i> (sig. all months)	neg. concave-down correlation to May-July <i>PET</i>	Helcoski et al. 2019
Lilly Dickey Woods, Indiana, USA					
LITU	pos. correlations with Jun-Aug PDSI	pos. response to June <i>PPT</i>	neg. response to Jun-Aug <i>T_{max}</i>	neg. response to June <i>PET</i>	Maxwell, Harley, and Robeson 2016
QUAL	pos. correlations with Jun-Aug PDSI	pos. response to June <i>PPT</i>	neg. response to Jun-Aug <i>T_{max}</i>	neg. response to June <i>PET</i>	Maxwell, Harley, and Robeson 2016
QUMO	pos. correlations with Jun-Aug PDSI	pos. response to June <i>PPT</i>	neg. response to Jun-Aug <i>T_{max}</i>	neg. response to June <i>PET</i>	Maxwell, Harley, and Robeson 2016
QUVE	pos. correlations with Jun-Aug PDSI	pos. response to June <i>PPT</i>	neg. response to Jun-Aug <i>T_{max}</i>	neg. response to June <i>PET</i>	Maxwell, Harley, and Robeson 2016
Harvard Forest, Massachusetts, USA					
ACRU	NA		no response to Jan-April <i>T_{min}*</i>	neg. correlation to Mar <i>PET</i>	Alexander et al. 2019
BEAL	NA		no response to Jan-April <i>T_{min}*</i>	neg. correlation to Mar <i>PET</i>	Alexander et al. 2019
QURU	NA		no response to Jan-April <i>T_{min}*</i>	neg. correlation to Mar <i>PET</i>	Alexander et al. 2019
TSCA	NA		pos. response to Jan-April <i>T_{min}*</i>	pos. correlation to March <i>PET</i>	Alexander et al. 2019

S5, cont.

species	Precipitation response		Temperature response		reference
	previously observed	observed here	previously observed	observed here	
Žofín Forest Dynamics Plot, Czech Republic					
ABAL	no sig. correlations with June-July <i>PPT</i>	pos. correlation to p.Jun-p.July <i>PPT</i> frequency	sig. pos. correlation to April T (strongest T correlation)	pos. correlation to Jan-March T_{max}	Kašpar, Tumajer, Vašíčková, and Šamonil, in review
FASY	no sig. correlations with June-July <i>PPT</i>	pos. correlation to p.Jun-p.July <i>PPT</i> frequency	sig. pos. correlation to Jan T (strongest T correlation)	pos. correlation to Jan-March T_{max}	Kašpar, Tumajer, Vašíčková, and Šamonil, in review
PIAB	modest pos. correlations (n.s) with June-July <i>PPT</i> ≥700m elev. sites moisture limited June-Aug	non-sig. pos. correlation to p.Jun-p.July <i>PPT</i> frequency	sig. pos. correlation to March T (strongest current-year T correlation) ≥700m elev. sites temperature limited except June-Aug	pos. correlation to Jan-March T_{max}	Kašpar, Tumajer, Vašíčková, and Šamonil, in review Tumajer et al. 2017
Niobrara, Nebraska, USA					
BEPA	little relationship to <i>PPT</i> within analysis timeframe (exception: pos. correlation with pAug <i>PPT</i>); positive correlation to streamflow (<i>SF</i>) in some months (pJune, pAug, pNov, cJune); stronger relationship to PDSI	no sig. correlation to <i>PPT</i> , <i>PDF</i> , or <i>SF</i>	little relationship to T_{mean} within analysis timeframe (exception: neg. correlation with pJune and cJan T_{mean})	neg. concave-down correlation to pJune T_{mean}	Bumann et al. 2019
Little Tesuque, New Mexico, USA					
PIPO	increases with pOct-June <i>PPT</i> ** increase with cold-season <i>PPT</i> **	pos. concave-down correlation to pNov-cJuly <i>PPT</i>	NA		Touchan et al., 2011
PIST3	increases with pOct-June <i>PPT</i> **	pos. concave-down correlation to pNov-cJuly <i>PPT</i>	decrease with vapor pressure deficit of pAug-pOct and May-July** NA	neg. concave-down correlation to May-July T_{max}	Williams et al., 2013
Cedar Breaks, Utah, USA					
	NA		NA		-
Scotty Creek, NW Territories, Canada					
PIMA	predominantly pos. responses to annual <i>PPT</i>	pos. concave-down correlation to pJune-pAug <i>PPT</i>	predominantly positive responses to mean annual T_{mean} prior to 1970, shifting to predominantly negative responses after 1970	pos. correlation to July T_{max} . Temperature correlations predominantly pos. prior to 1970 (to pAug T_{min}), neg. after 1970 (to pJune T_{min})	Sniderhan and Baltzer 2016

*Indicates results from a regional study including but not limited to cores from the focal site.

**Indicates results from a regional study not including the focal site, but believed to be representative.

Figure S1. Density plot of core record start years by species for BCNM.

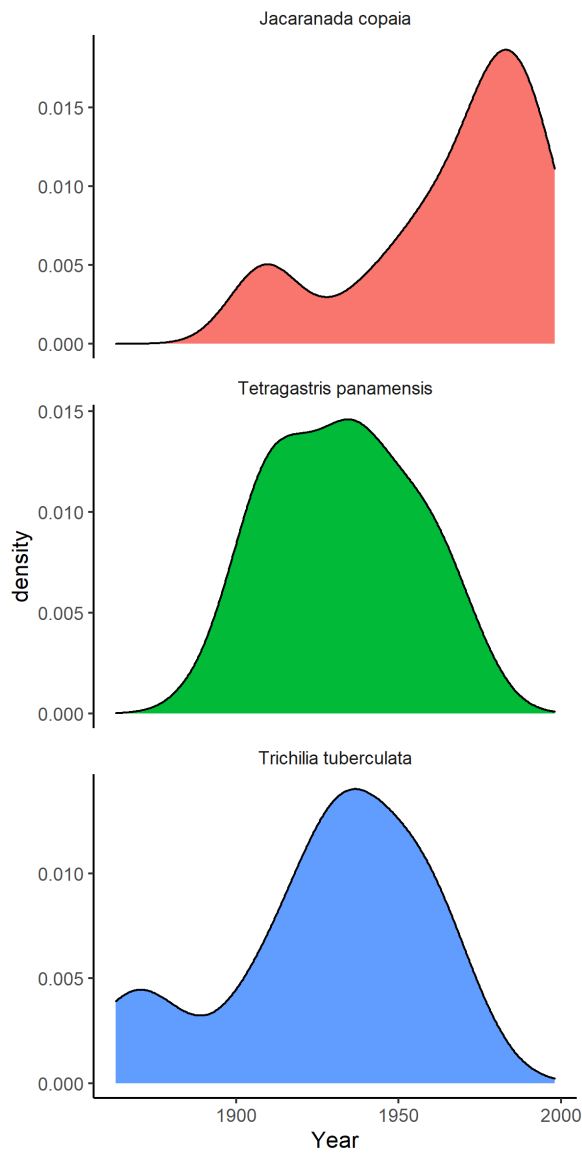


Figure S1. Density plot of core record start years by species for BCNM. This distribution approximates—but does not entirely match—the age distribution of trees cored. The core record start year can occur after a tree's recruitment year (i.e., year when the tree reached coring height) if the core fails to hit center or if the tree's center is lost to heartrot. “Heartrot was common at this site, implying that recruitment years are overestimated for some trees.”

Figure S2. Density plot of core record start years by species for HKK.

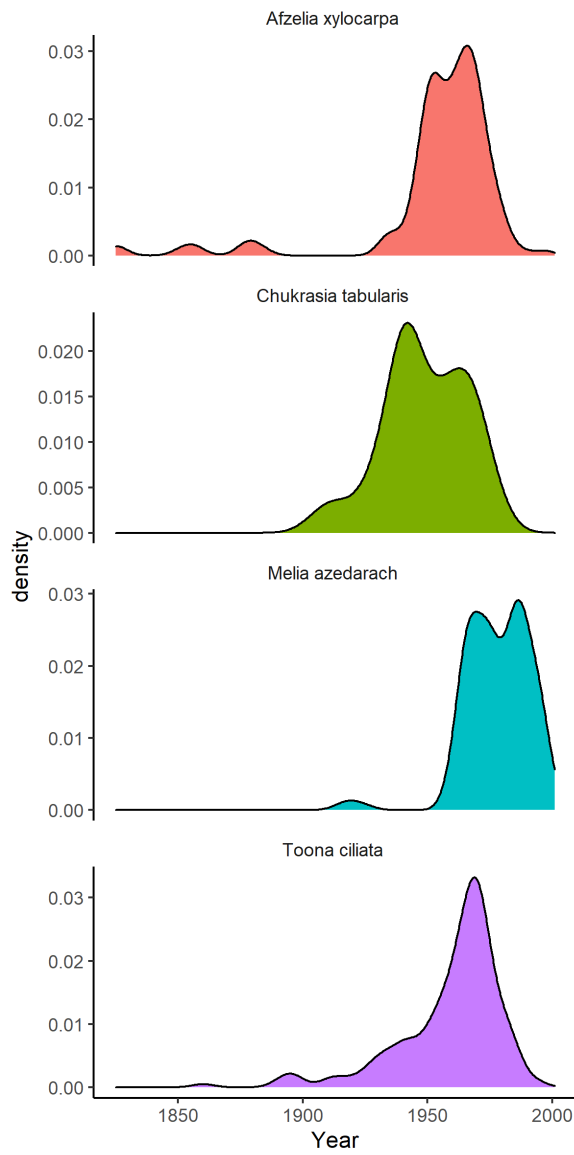


Figure S2. Density plot of core record start years by species for HKK. This distribution approximates—but does not entirely match—the age distribution of trees cored. The core record start year can occur after a tree's recruitment year (i.e., year when the tree reached coring height) if the core fails to hit center or if the tree's center is lost to heartrot.

Figure S3. Density plot of core record start years by species for SCBI.

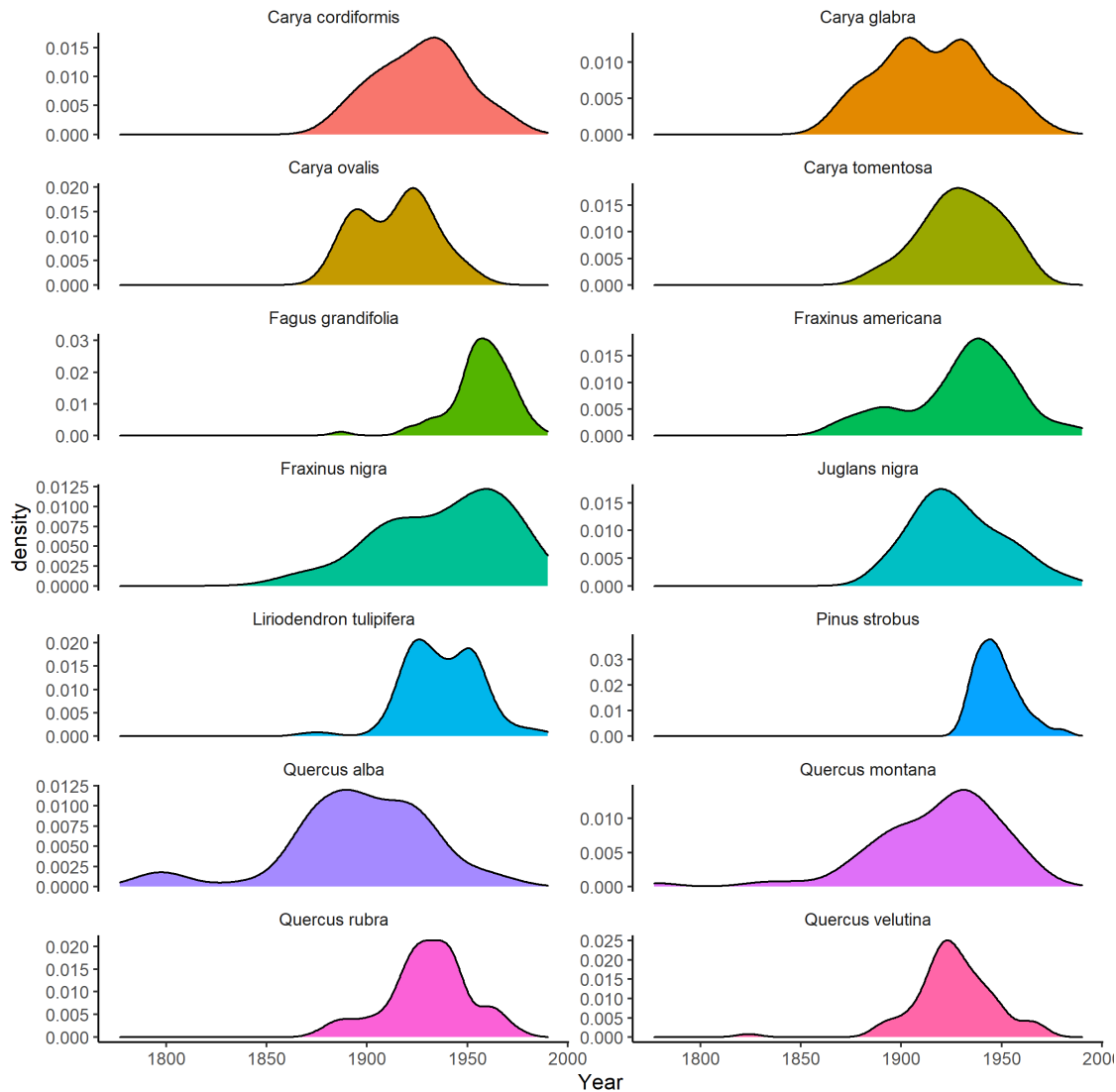


Figure S3. Density plot of core record start years by species for SCBI. This distribution approximates—but does not entirely match—the age distribution of trees cored. The core record start year can occur after a tree's recruitment year (i.e., year when the tree reached coring height) if the core fails to hit center or if the tree's center is lost to heartrot.

Figure S4. Density plot of core record start years by species for LDW.

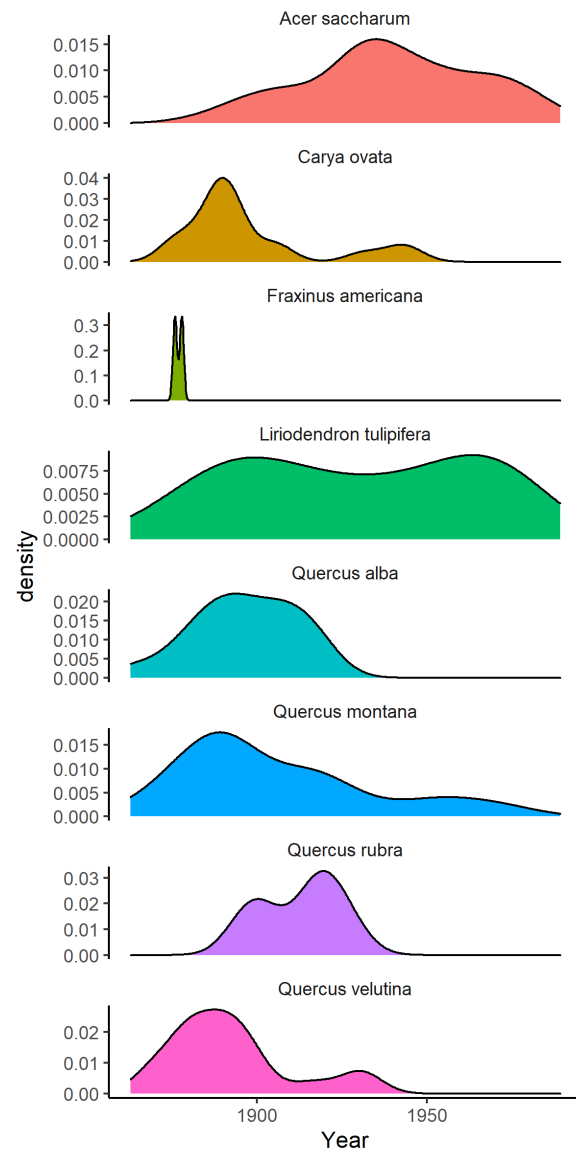


Figure S4. Density plot of core record start years by species for LDW. This distribution approximates—but does not entirely match—the age distribution of trees cored. The core record start year can occur after a tree's recruitment year (i.e., year when the tree reached coring height) if the core fails to hit center or if the tree's center is lost to heartrot.

Figure S5. Density plot of core record start years by species for HF.

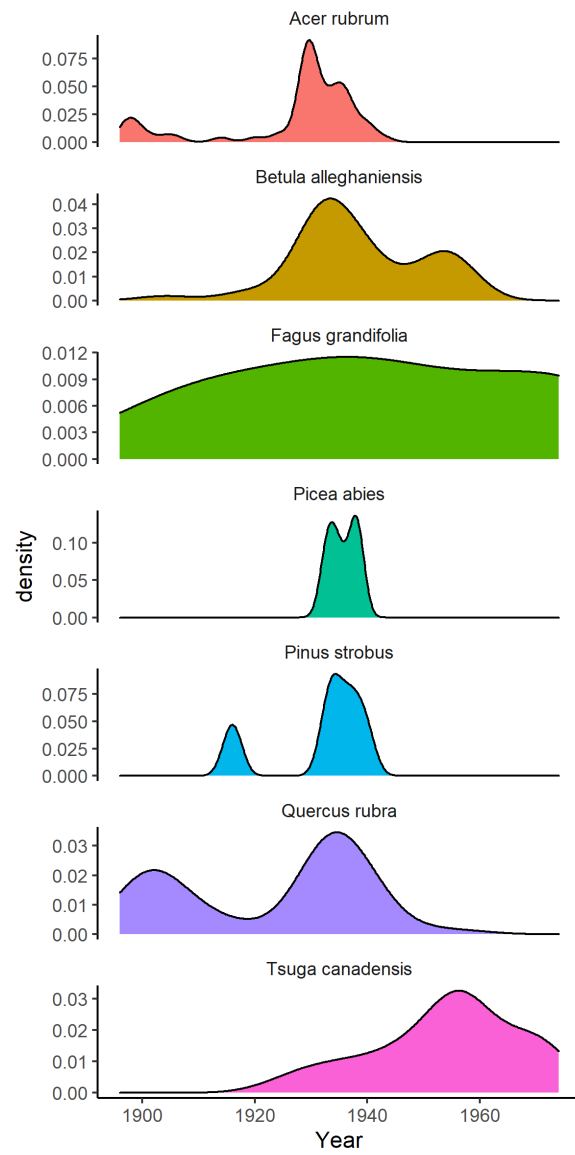


Figure S5. Density plot of core record start years by species for HF. This distribution approximates—but does not entirely match—the age distribution of trees cored. The core record start year can occur after a tree's recruitment year (i.e., year when the tree reached coring height) if the core fails to hit center or if the tree's center is lost to heartrot.

Figure S6. Density plot of core record start years by species for ZOF.

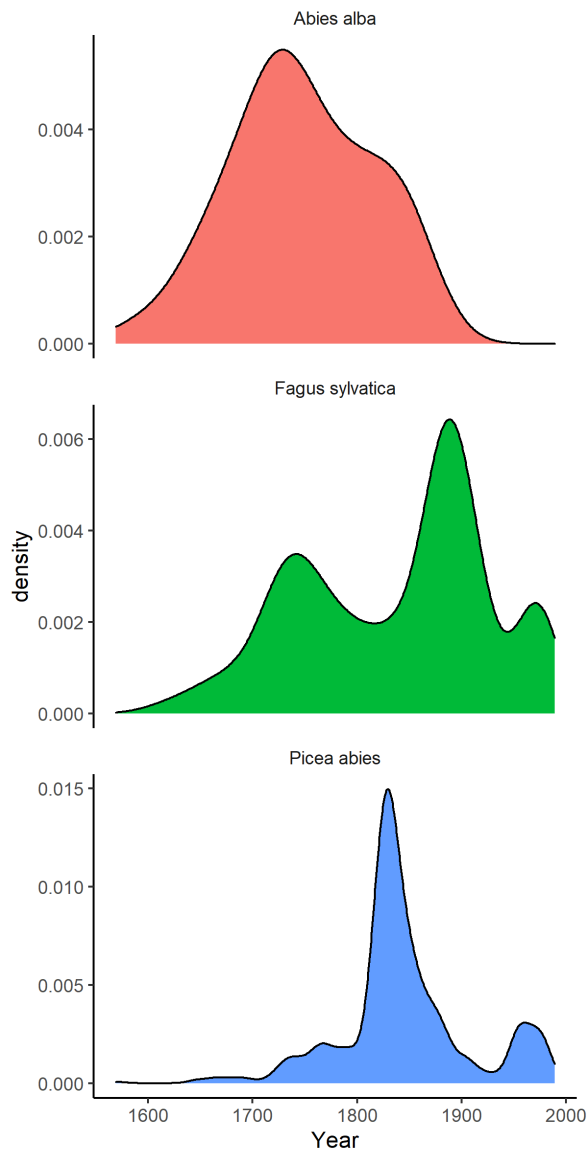


Figure S6. Density plot of core record start years by species for ZOF. This distribution approximates—but does not entirely match—the age distribution of trees cored. The core record start year can occur after a tree's recruitment year (i.e., year when the tree reached coring height) if the core fails to hit center or if the tree's center is lost to heartrot.

Figure S7. Density plot of core record start years by species for NIO.

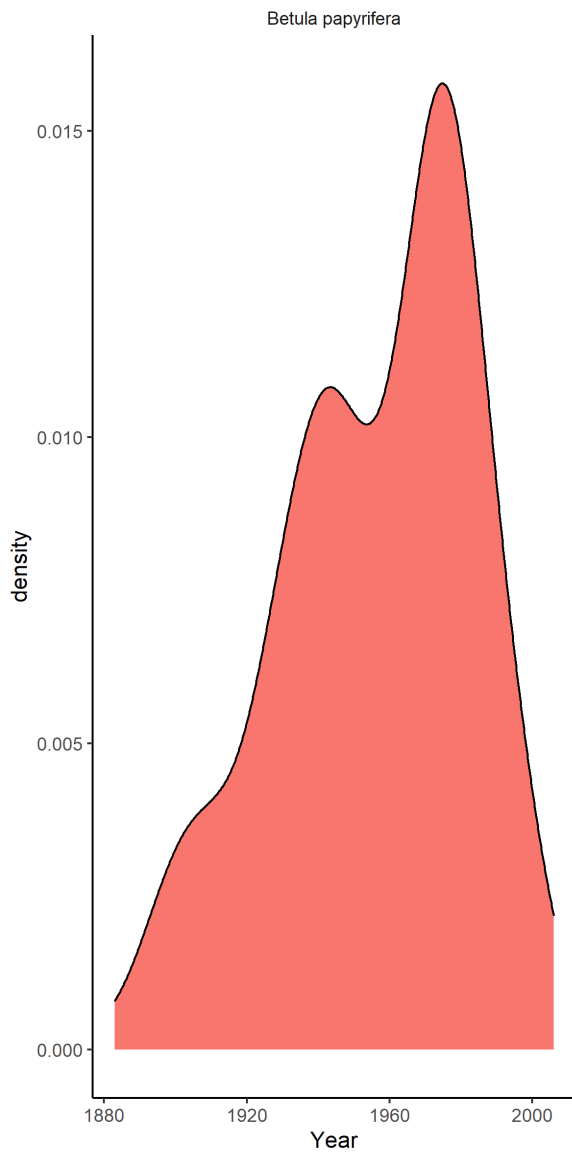


Figure S7. Density plot of core record start years by species for NIO. This distribution approximates—but does not entirely match—the age distribution of trees cored. The core record start year can occur after a tree's recruitment year (i.e., year when the tree reached coring height) if the core fails to hit center or if the tree's center is lost to heartrot.

Figure S8. Density plot of core record start years by species for LT.

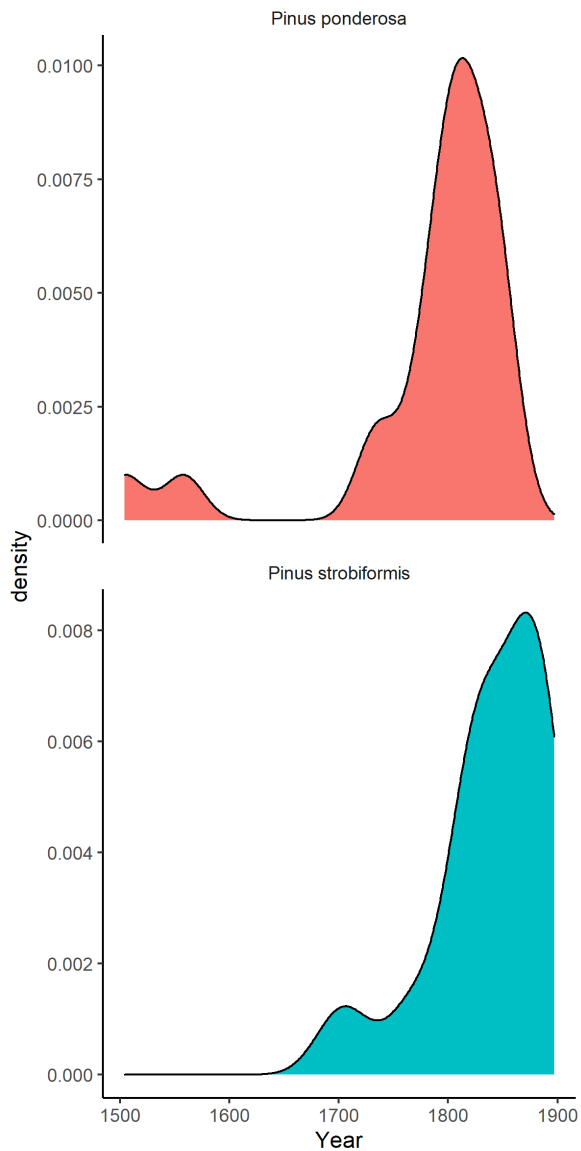


Figure S8. Density plot of core record start years by species for LT. This distribution approximates—but does not entirely match—the age distribution of trees cored. The core record start year can occur after a tree's recruitment year (i.e., year when the tree reached coring height) if the core fails to hit center or if the tree's center is lost to heartrot.

Figure S9. Density plot of core record start years by species for CB.

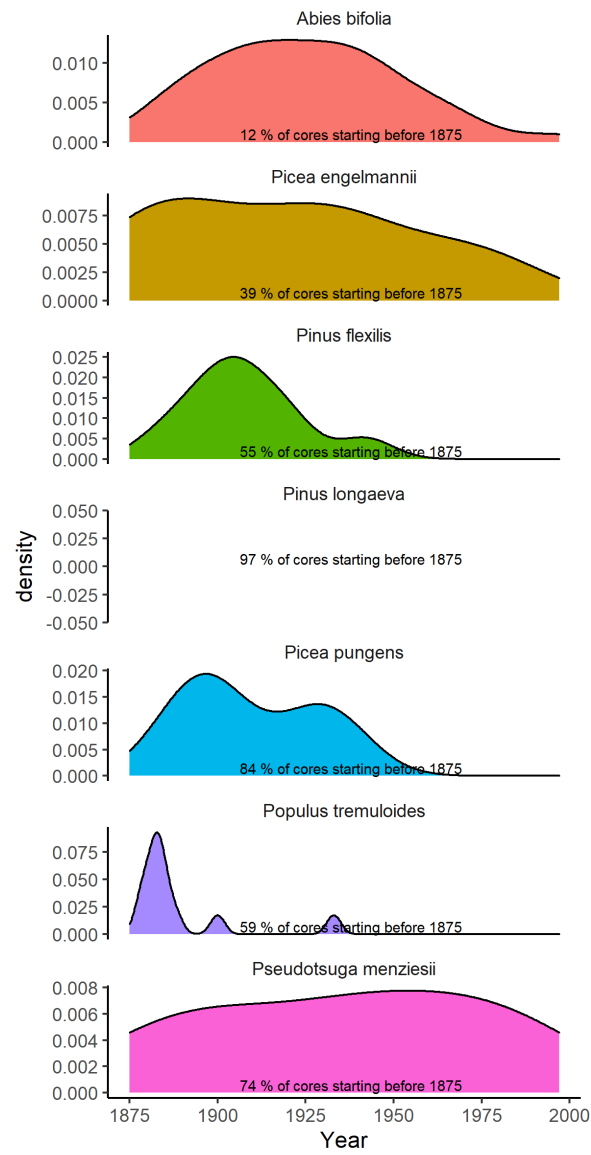


Figure S9. Density plot of core record start years by species for CB. This distribution approximates—but does not entirely match—the age distribution of trees cored. The core record start year can occur after a tree's recruitment year (i.e., year when the tree reached coring height) if the core fails to hit center or if the tree's center is lost to heartrot.

Figure S10. Density plot of core record start years by species for SC.

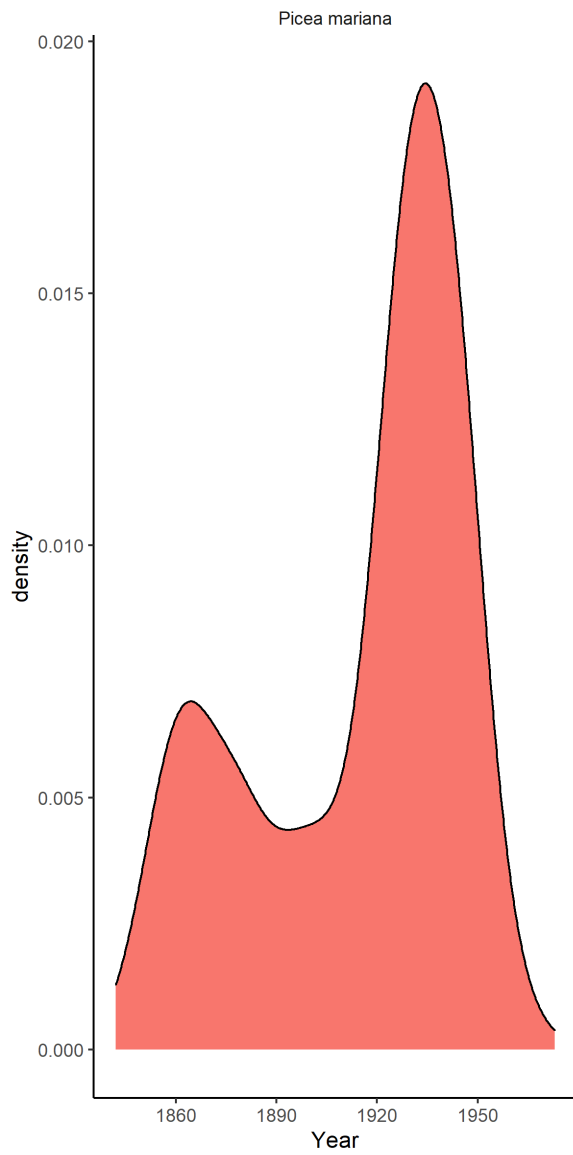
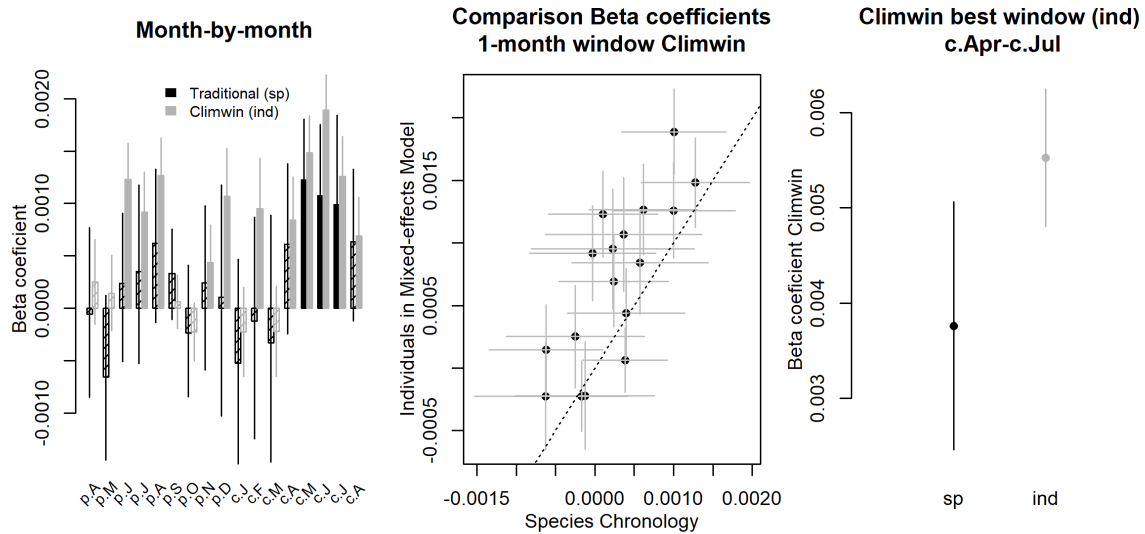


Figure S10. Density plot of core record start years by species for SC. This distribution approximates—but does not entirely match—the age distribution of trees cored. The core record start year can occur after a tree's recruitment year (i.e., year when the tree reached coring height) if the core fails to hit center or if the tree's center is lost to heartrot.

Figure S11. Comparison of our approach with traditional methods of identifying climate signals: *Liriodendron tulipifera* at SCBI.

Precipitation



Potential Evapotranspiration

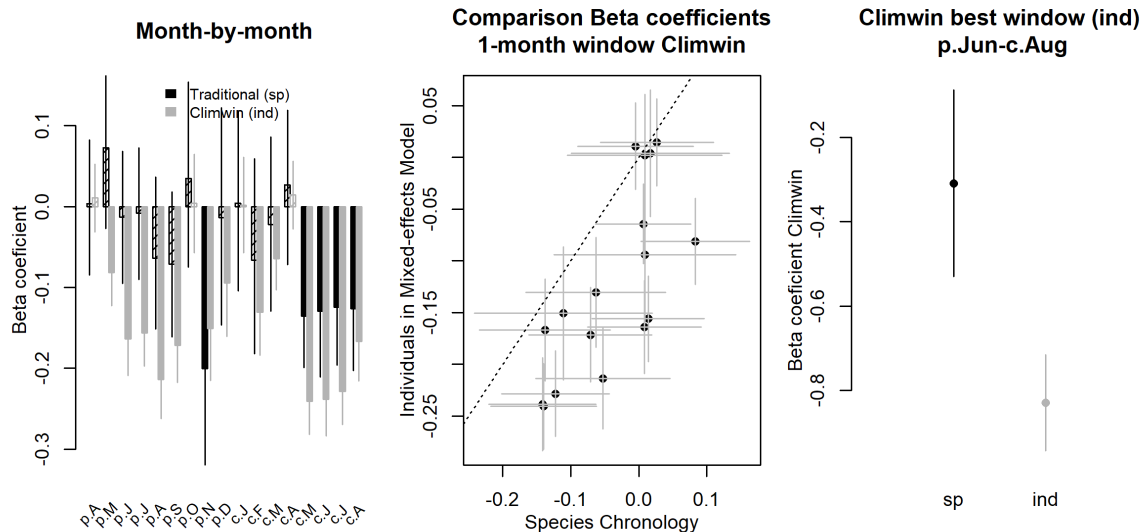
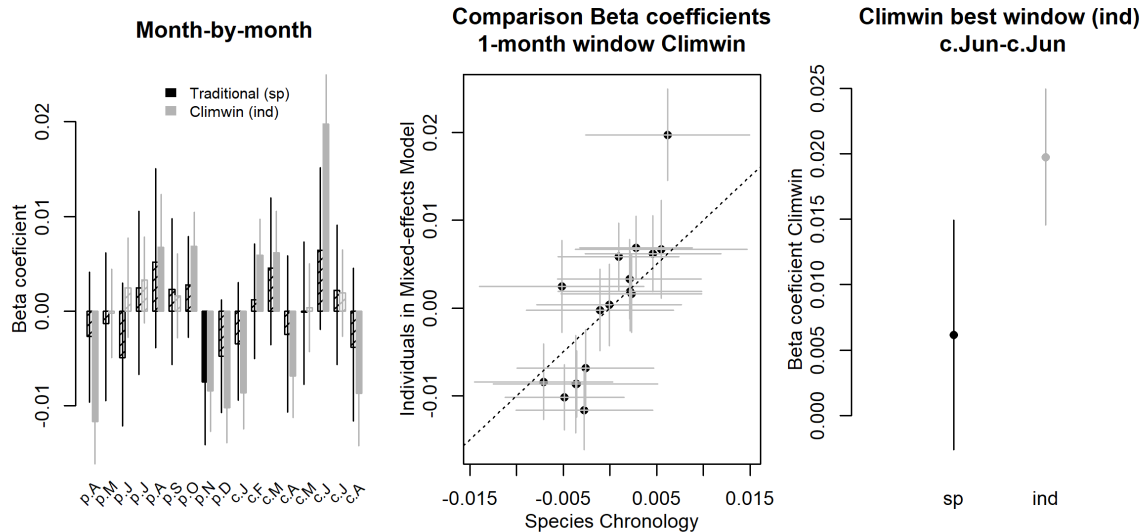


Figure S11. Comparison of our approach with traditional methods of identifying climate signals: *Liriodendron tulipifera* at SCBI. Shown are responses to the precipitation- and temperature-group variables selected as most influential by the *climwin* analysis. Left panels show a month-by-month comparison of *beta* (slope) coefficients for the relationship between tree growth and the monthly climate variable from species-level residual chronologies (traditional approach) and from individual-level analysis in *climwin* (approach presented here). Center panels compare the monthly *beta* coefficient estimates, with the dotted line indicating 1:1 correspondence. Finally, the right panels compare *beta* coefficients for the optimal window selected by *climwin*. Error bars indicate standard error of slope estimates. Note that 1:1 correspondence is not necessarily expected. See Appendix 5 for analysis methods and discussion of expected correspondence.

Figure S12. Comparison of our approach with traditional methods of identifying climate signals: *Abies alba* at Zofin.

Precipitation Day Frequency



Maximum temperature

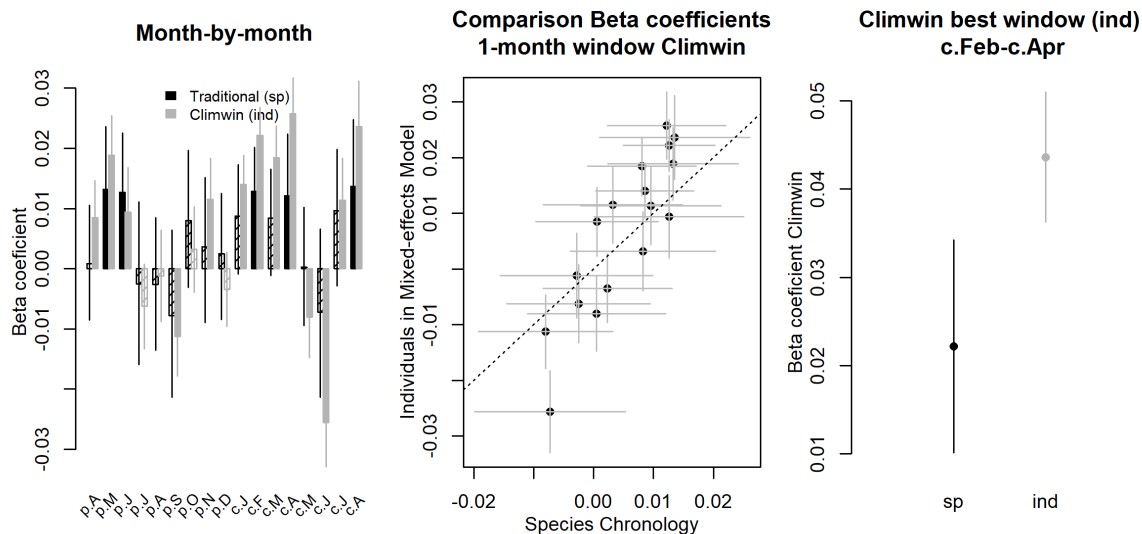
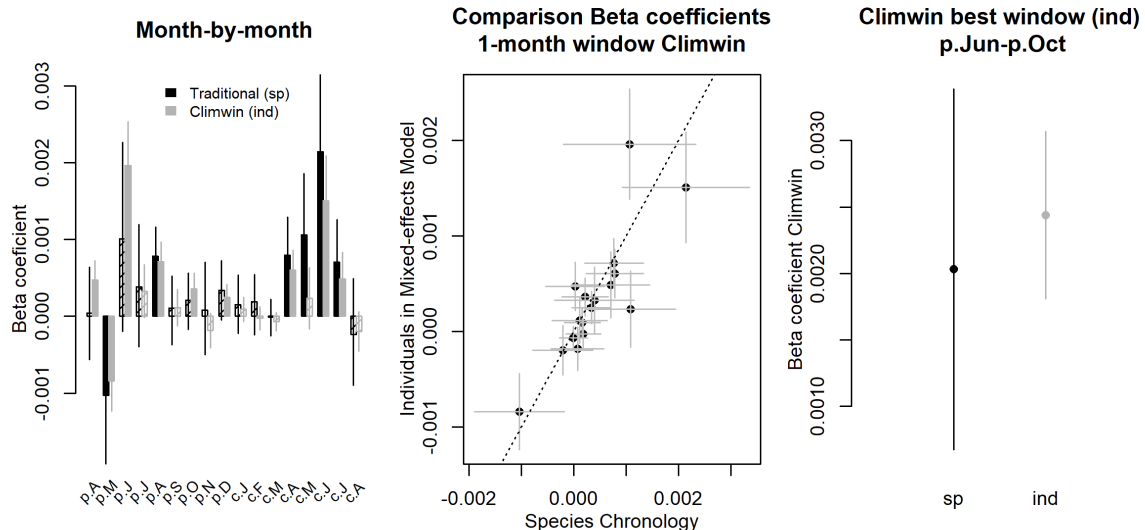


Figure S12. Comparison of our approach with traditional methods of identifying climate signals: *Abies alba* at Zofin. Shown are responses to the precipitation- and temperature-group variables selected as most influential by the *climwin* analysis. Left panels show a month-by-month comparison of *beta* (slope) coefficients for the relationship between tree growth and the monthly climate variable from species-level residual chronologies (traditional approach) and from individual-level analysis in *climwin* (approach presented here). Center panels compare the monthly *beta* coefficient estimates, with the dotted line indicating 1:1 correspondence. Finally, the right panels compare *beta* coefficients for the optimal window selected by *climwin*. Error bars indicate standard error of slope estimates. Note that 1:1 correspondence is not necessarily expected. See Appendix 5 for analysis methods and discussion of expected correspondence.

Figure S13. Comparison of our approach with traditional methods of identifying climate signals: *Pseudotsuga menziesii* at Cedar Breaks.

Precipitation



Maximum temperature

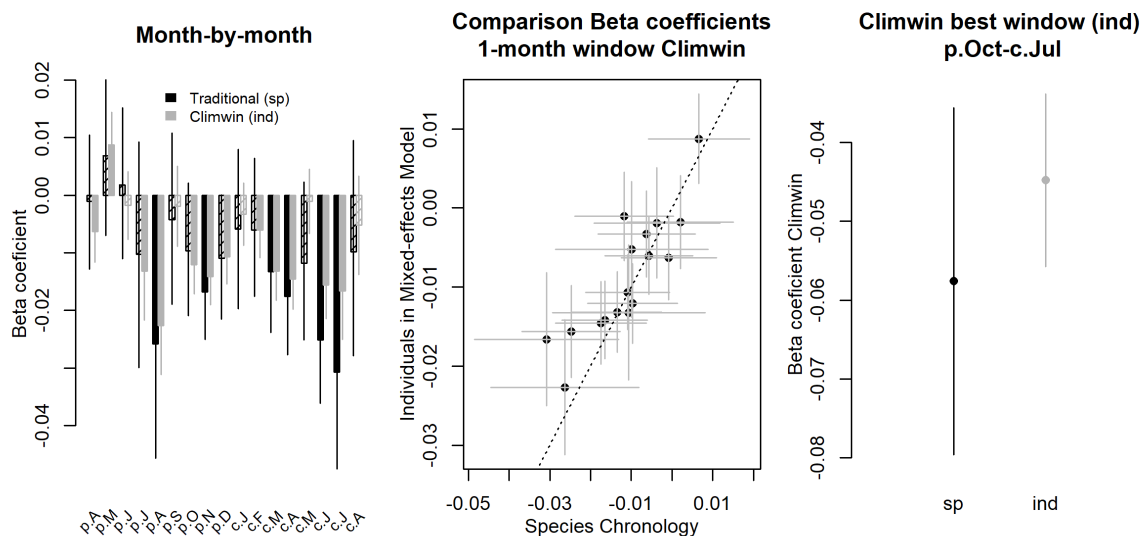
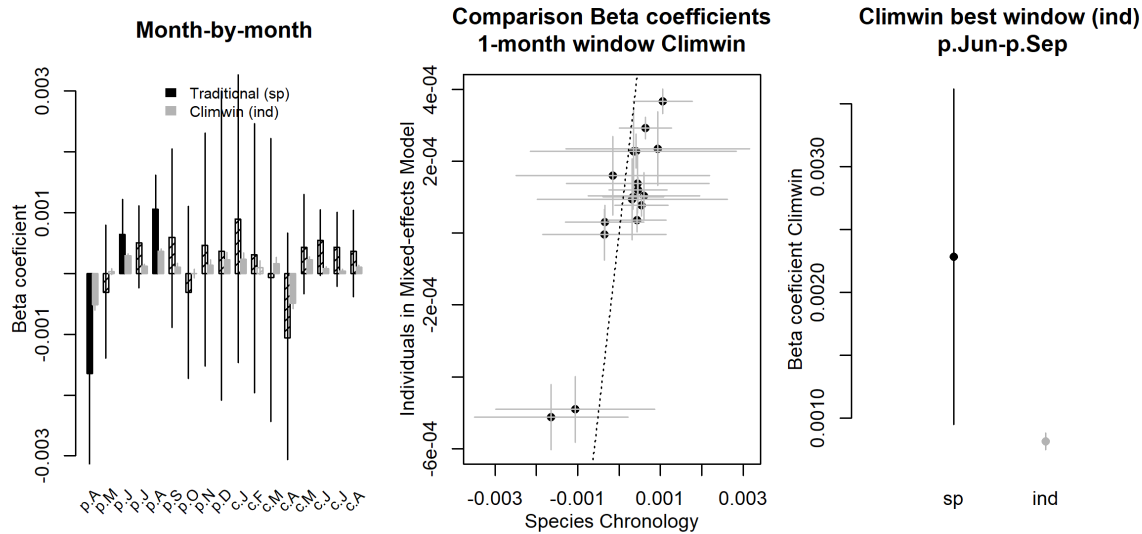


Figure S13. Comparison of our approach with traditional methods of identifying climate signals: *Pseudotsuga menziesii* at Cedar Breaks. Shown are responses to the precipitation- and temperature-group variables selected as most influential by the *climwin* analysis. Left panels show a month-by-month comparison of *beta* (slope) coefficients for the relationship between tree growth and the monthly climate variable from species-level residual chronologies (traditional approach) and from individual-level analysis in *climwin* (approach presented here). Center panels compare the monthly *beta* coefficient estimates, with the dotted line indicating 1:1 correspondence. Finally, the right panels compare *beta* coefficients for the optimal window selected by *climwin*. Error bars indicate standard error of slope estimates. Note that 1:1 correspondence is not necessarily expected. See Appendix 5 for analysis methods and discussion of expected correspondence.

Figure S14. Comparison of our approach with traditional methods of identifying climate signals: *Picea mariana* at Scotty Creek.

Precipitation



Maximum temperature

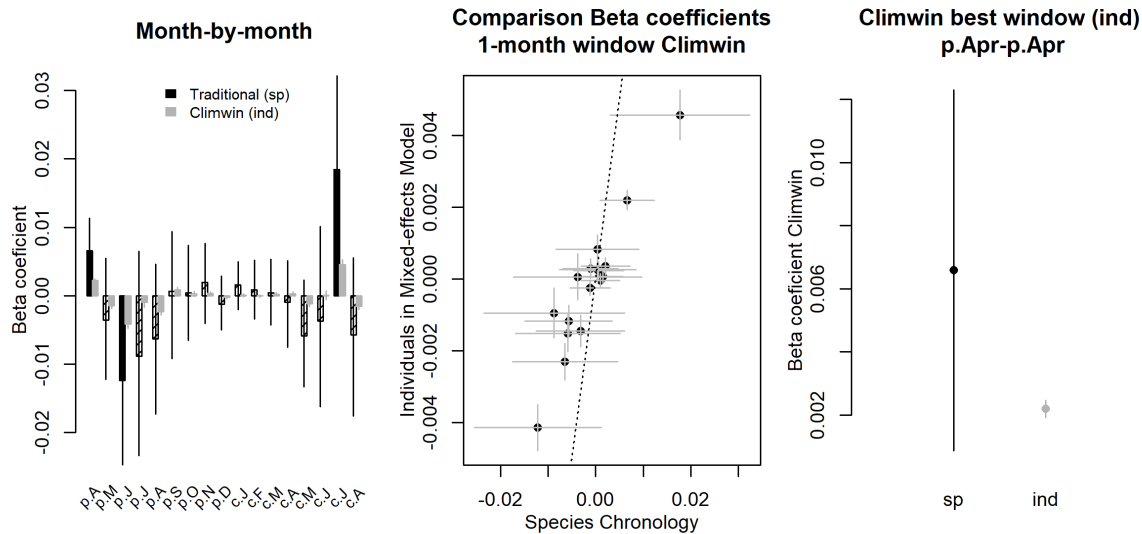


Figure S14. Comparison of our approach with traditional methods of identifying climate signals: *Picea mariana* at Scotty Creek. Shown are responses to the precipitation- and temperature-group variables selected as most influential by the *climwin* analysis. Left panels show a month-by-month comparison of *beta* (slope) coefficients for the relationship between tree growth and the monthly climate variable from species-level residual chronologies (traditional approach) and from individual-level analysis in *climwin* (approach presented here). Center panels compare the monthly *beta* coefficient estimates, with the dotted line indicating 1:1 correspondence. Finally, the right panels compare *beta* coefficients for the optimal window selected by *climwin*. Error bars indicate standard error of slope estimates. Note that 1:1 correspondence is not necessarily expected. See Appendix 5 for analysis methods and discussion of expected correspondence.

Figure S15. Climwin output for water variable group at BCNM.

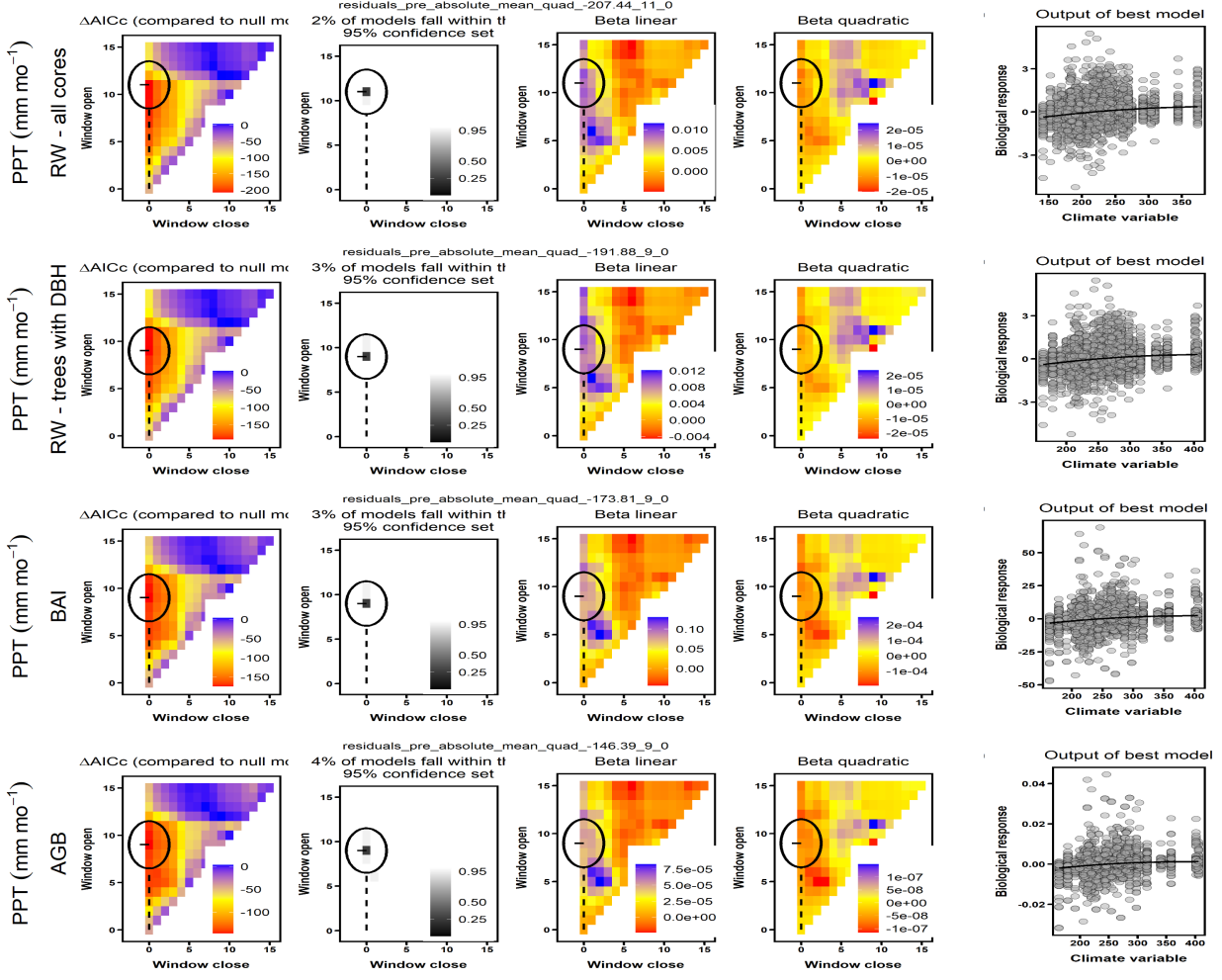


Figure S15. Climwin output for water variable group at BCNM. Rows correspond to the four different models run: (1) all *RW* data, (2) *RW* for the subset of cores for which \$DBH could be reconstructed, (3) *BAI*, and (4) *AGB* growth. The first four columns give statistics for time windows tested in *climwin*, where window open and close indicate months prior to current August. Difference in *AIC* relative to a model with no climate term (first column) is used to select the optimal time window (second column). The third and fourth columns give values of linear and quadratic terms for each time window. The final column shows the correlation of individual-level residuals to the selected climate variable, with the function fit in *climwin* (not the final fit).

Figure S16. Climwin output for temperature variable group at BCNM.

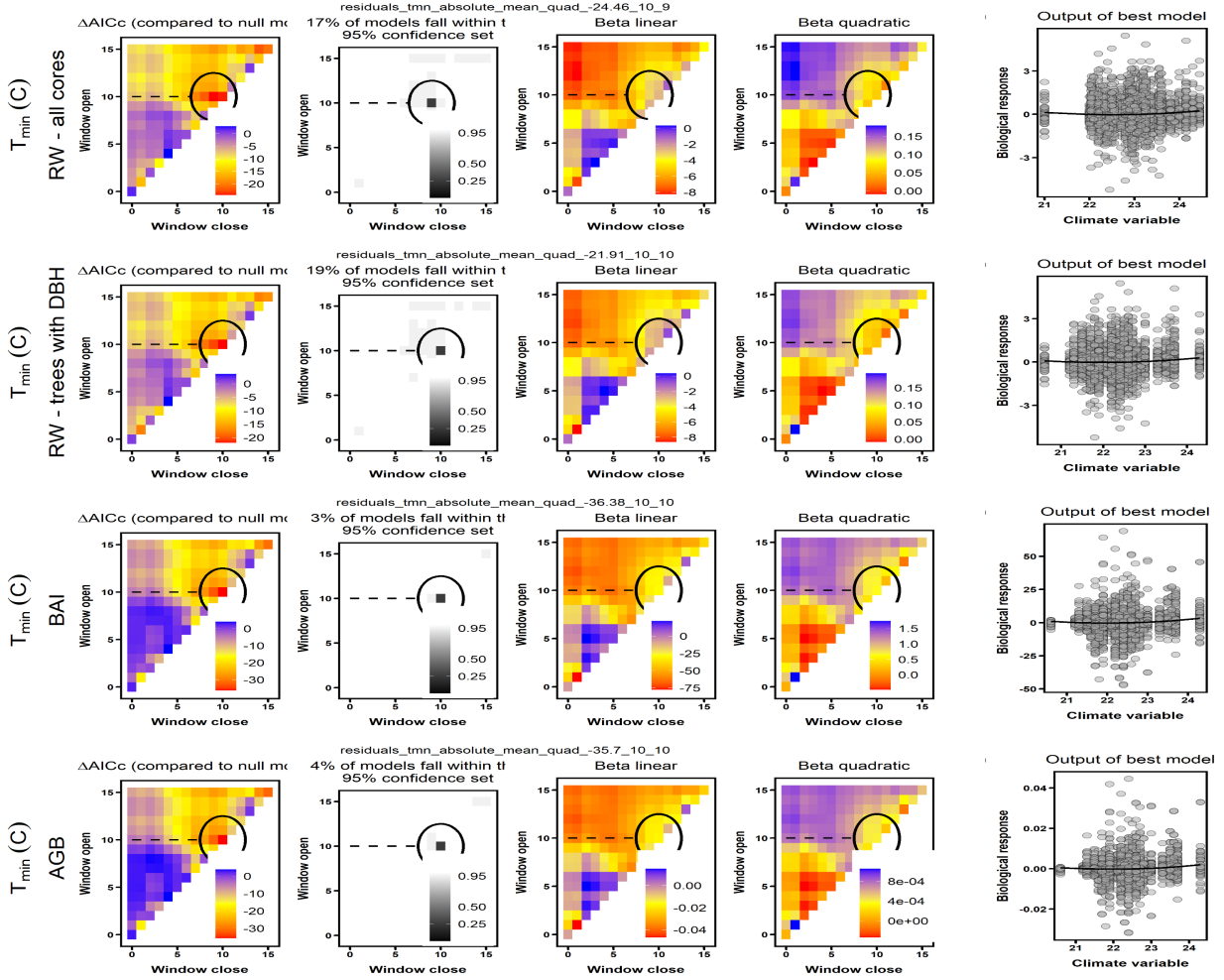


Figure S16. Climwin output for temperature variable group at BCNM. Rows correspond to the four different models run: (1) all *RW* data, (2) *RW* for the subset of cores for which $\$DBH$ could be reconstructed, (3) *BAI*, and (4) *AGB* growth. The first four columns give statistics for time windows tested in *climwin*, where window open and close indicate months prior to current August. Difference in *AIC* relative to a model with no climate term (first column) is used to select the optimal time window (second column). The third and fourth columns give values of linear and quadratic terms for each time window. The final column shows the correlation of individual-level residuals to the selected climate variable, with the function fit in *climwin* (not the final fit).

Figure S17. Climwin output for water variable group at HKK.

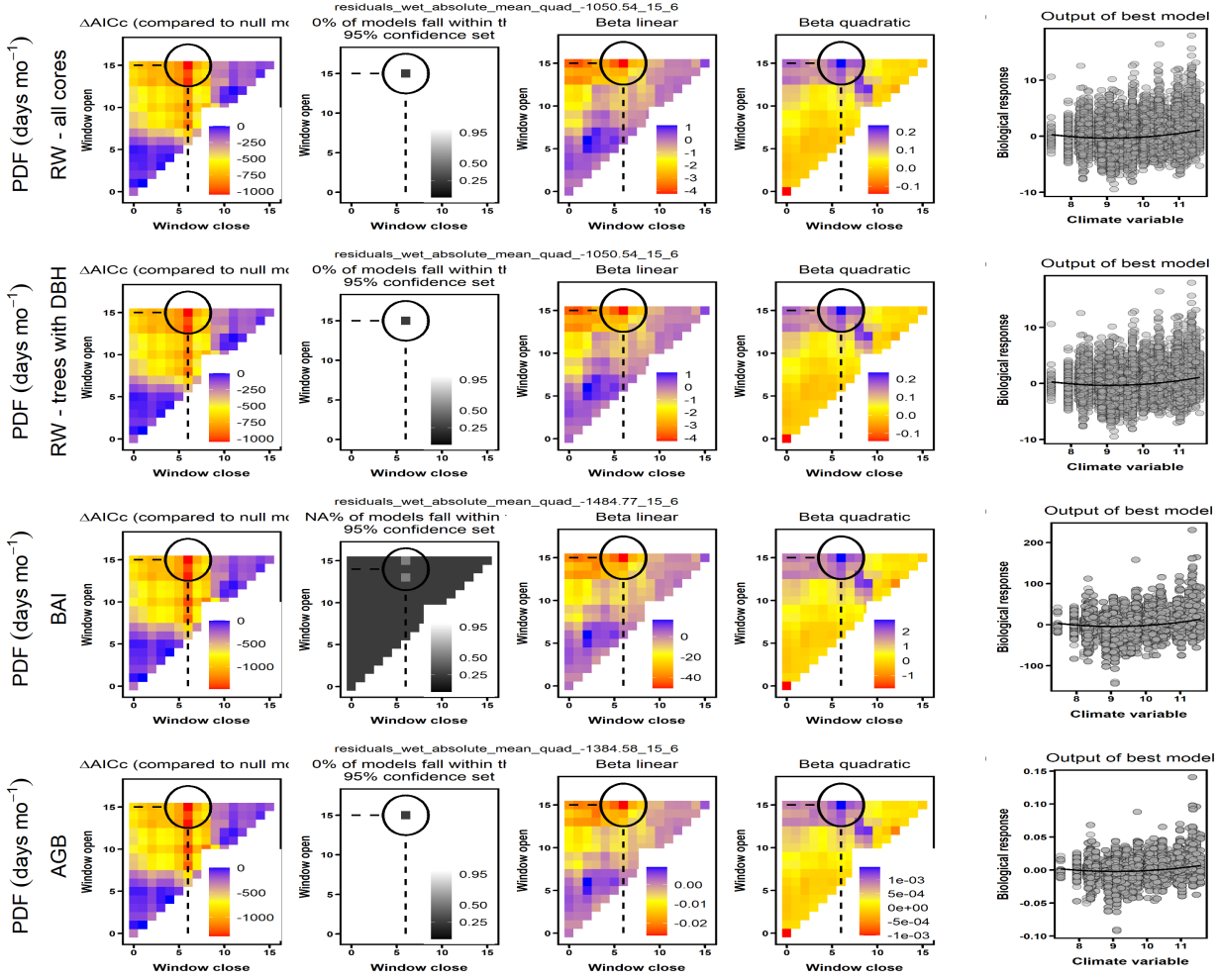


Figure S17. Climwin output for water variable group at HKK. Rows correspond to the four different models run: (1) all *RW* data, (2) *RW* for the subset of cores for which $\$DBH$ could be reconstructed, (3) *BAI*, and (4) *AGB* growth. The first four columns give statistics for time windows tested in *climwin*, where window open and close indicate months prior to current August. Difference in *AIC* relative to a model with no climate term (first column) is used to select the optimal time window (second column). The third and fourth columns give values of linear and quadratic terms for each time window. The final column shows the correlation of individual-level residuals to the selected climate variable, with the function fit in *climwin* (not the final fit).

Figure S18. Climwin output for temperature variable group at HKK.

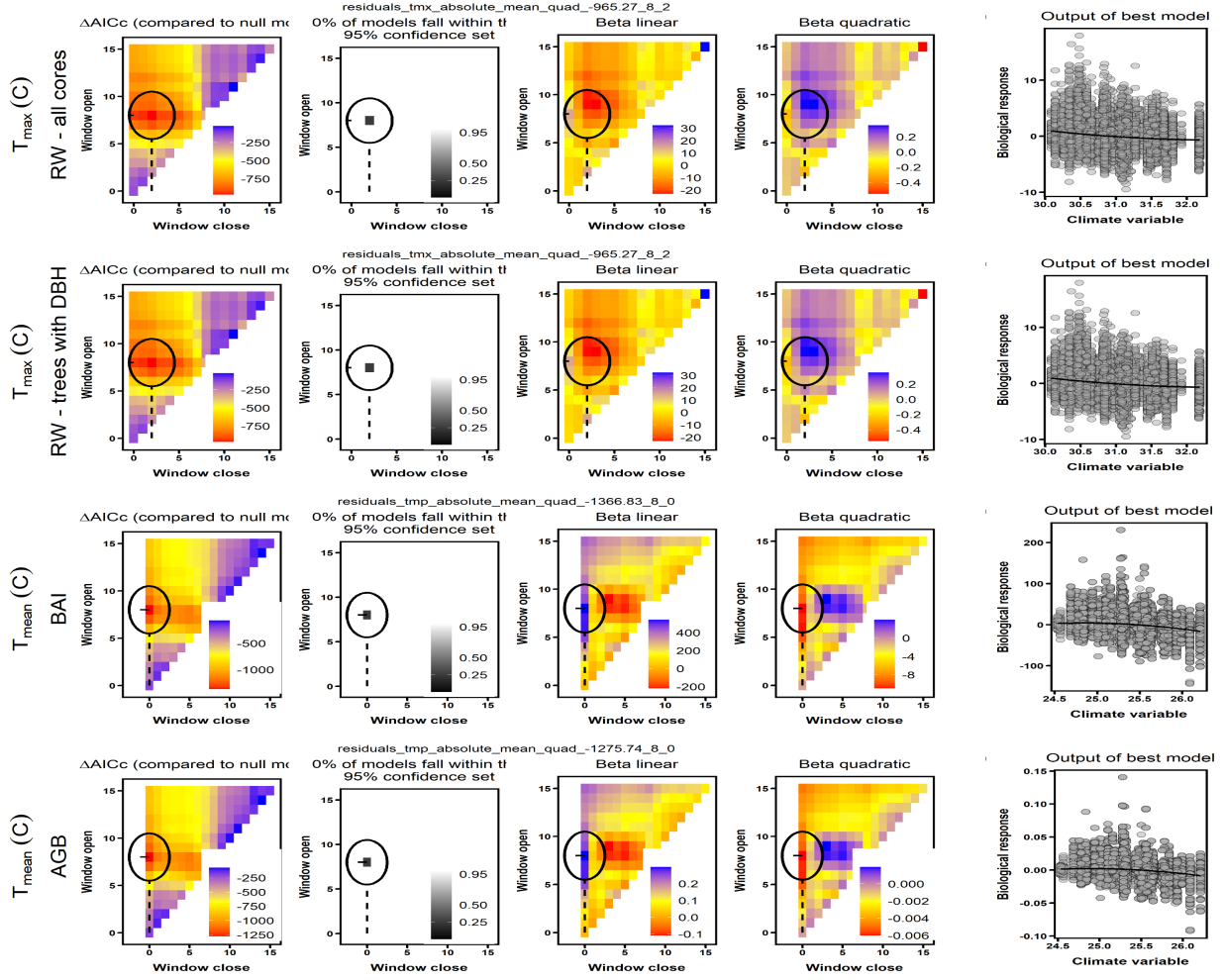


Figure S18. Climwin output for temperature variable group at HKK. Rows correspond to the four different models run: (1) all *RW* data, (2) *RW* for the subset of cores for which $\$DBH$ could be reconstructed, (3) *BAI*, and (4) *AGB* growth. The first four columns give statistics for time windows tested in *climwin*, where window open and close indicate months prior to current August. Difference in *AIC* relative to a model with no climate term (first column) is used to select the optimal time window (second column). The third and fourth columns give values of linear and quadratic terms for each time window. The final column shows the correlation of individual-level residuals to the selected climate variable, with the function fit in *climwin* (not the final fit).

Figure S19. Climwin output for water variable group at SCBI.

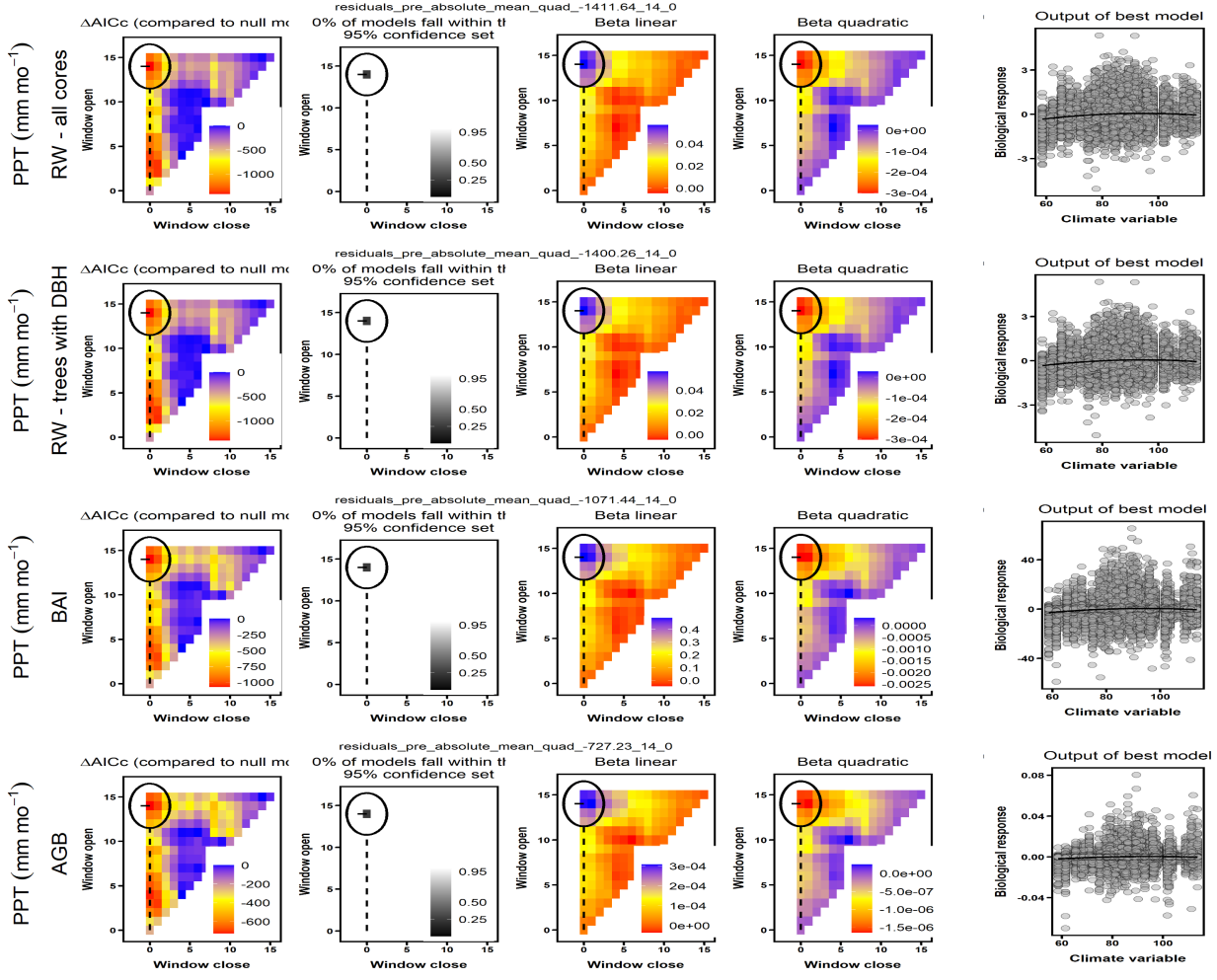


Figure S19. Climwin output for water variable group at SCBI. Rows correspond to the four different models run: (1) all *RW* data, (2) *RW* for the subset of cores for which $\$DBH$ could be reconstructed, (3) *BAI*, and (4) *AGB* growth. The first four columns give statistics for time windows tested in *climwin*, where window open and close indicate months prior to current August. Difference in *AIC* relative to a model with no climate term (first column) is used to select the optimal time window (second column). The third and fourth columns give values of linear and quadratic terms for each time window. The final column shows the correlation of individual-level residuals to the selected climate variable, with the function fit in *climwin* (not the final fit).

Figure S20. Climwin output for temperature variable group at SCBI.

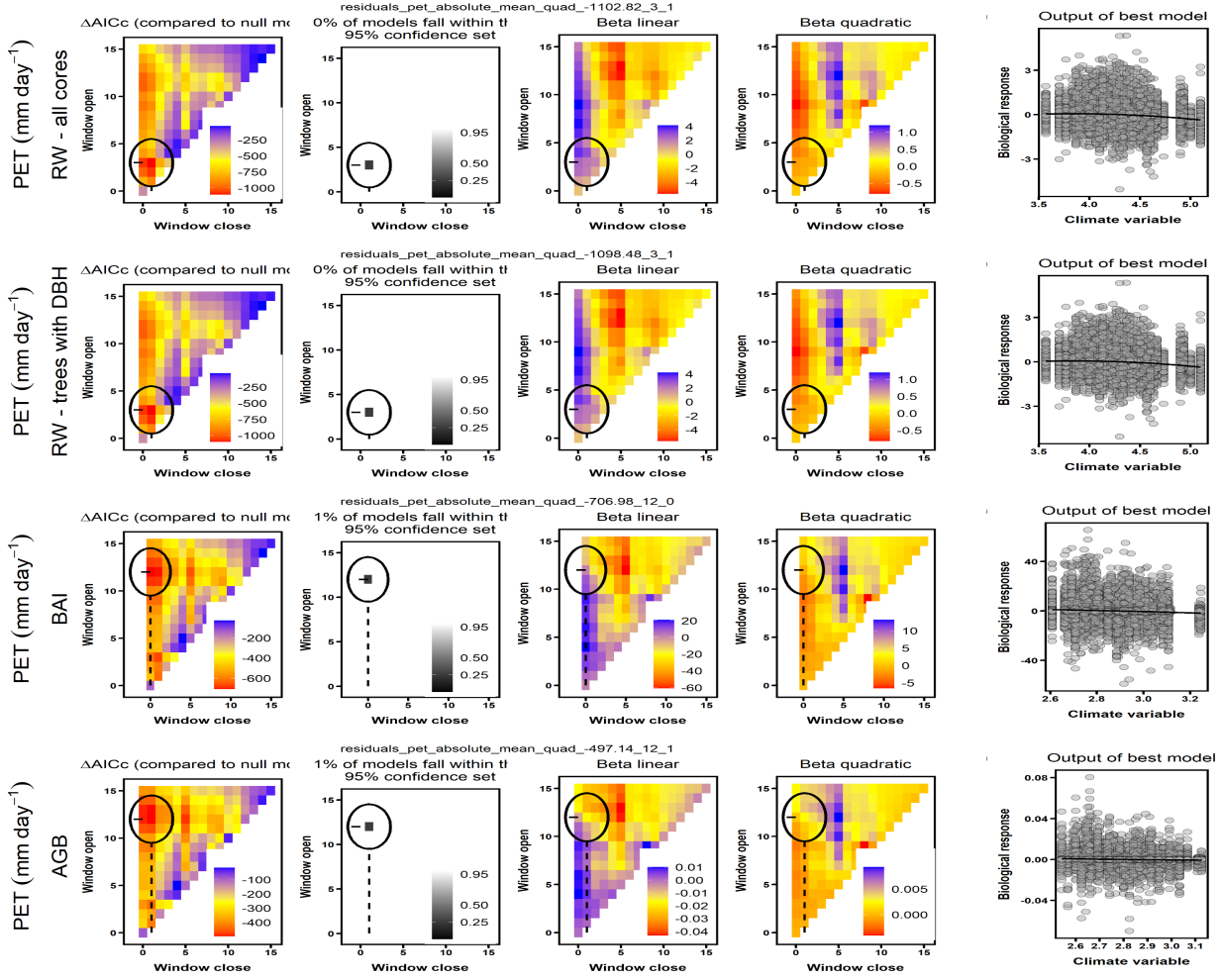


Figure S20. Climwin output for temperature variable group at SCBI. Rows correspond to the four different models run: (1) all *RW* data, (2) *RW* for the subset of cores for which $\$DBH$ could be reconstructed, (3) *BAI*, and (4) *AGB* growth. The first four columns give statistics for time windows tested in *climwin*, where window open and close indicate months prior to current August. Difference in *AIC* relative to a model with no climate term (first column) is used to select the optimal time window (second column). The third and fourth columns give values of linear and quadratic terms for each time window. The final column shows the correlation of individual-level residuals to the selected climate variable, with the function fit in *climwin* (not the final fit).

Figure S21. Climwin output for water variable group at LDW.

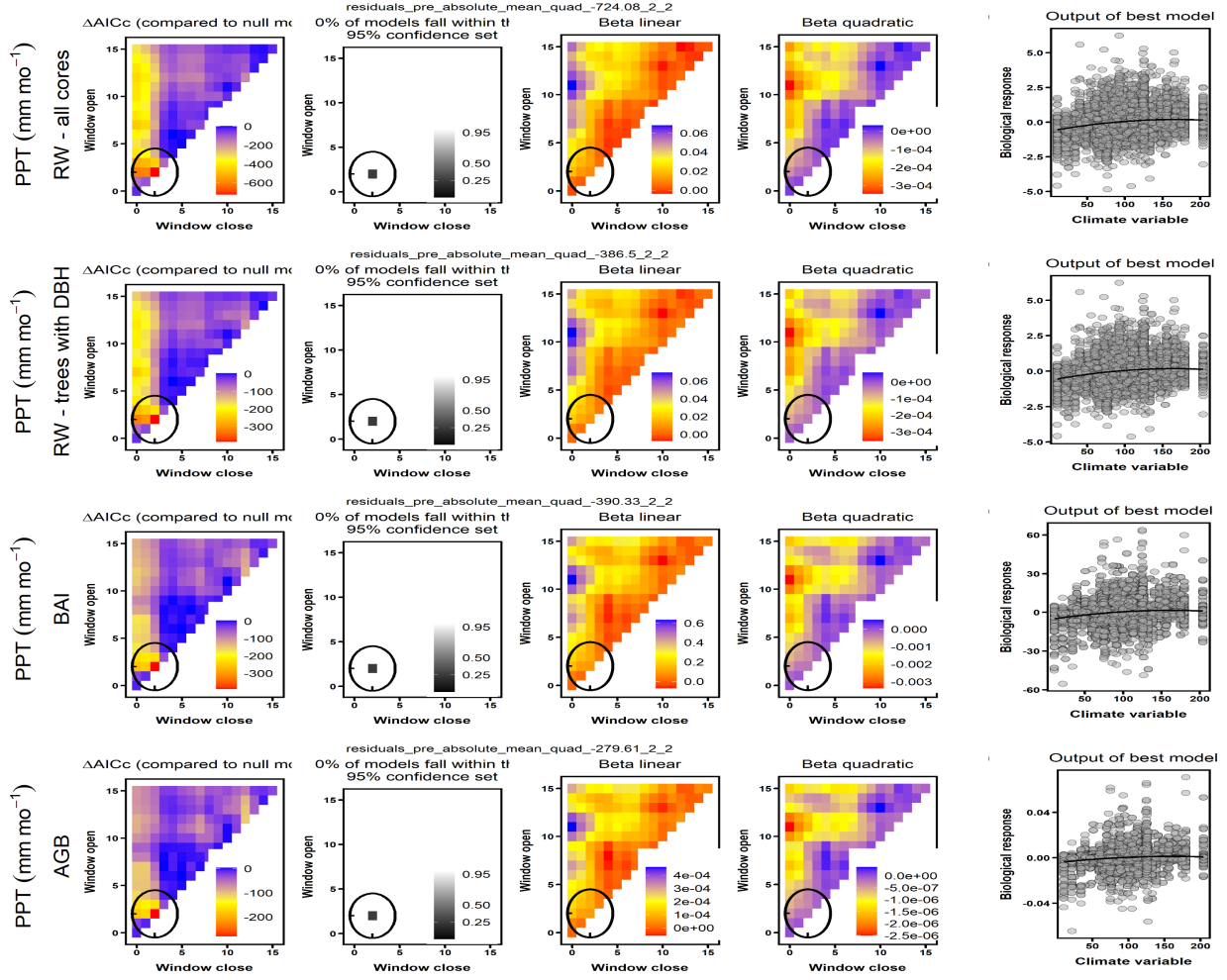


Figure S21. Climwin output for water variable group at LDW. Rows correspond to the four different models run: (1) all *RW* data, (2) *RW* for the subset of cores for which \$DBH could be reconstructed, (3) *BAI*, and (4) *AGB* growth. The first four columns give statistics for time windows tested in *climwin*, where window open and close indicate months prior to current August. Difference in *AIC* relative to a model with no climate term (first column) is used to select the optimal time window (second column). The third and fourth columns give values of linear and quadratic terms for each time window. The final column shows the correlation of individual-level residuals to the selected climate variable, with the function fit in *climwin* (not the final fit).

Figure S22. Climwin output for temperature variable group at LDW.

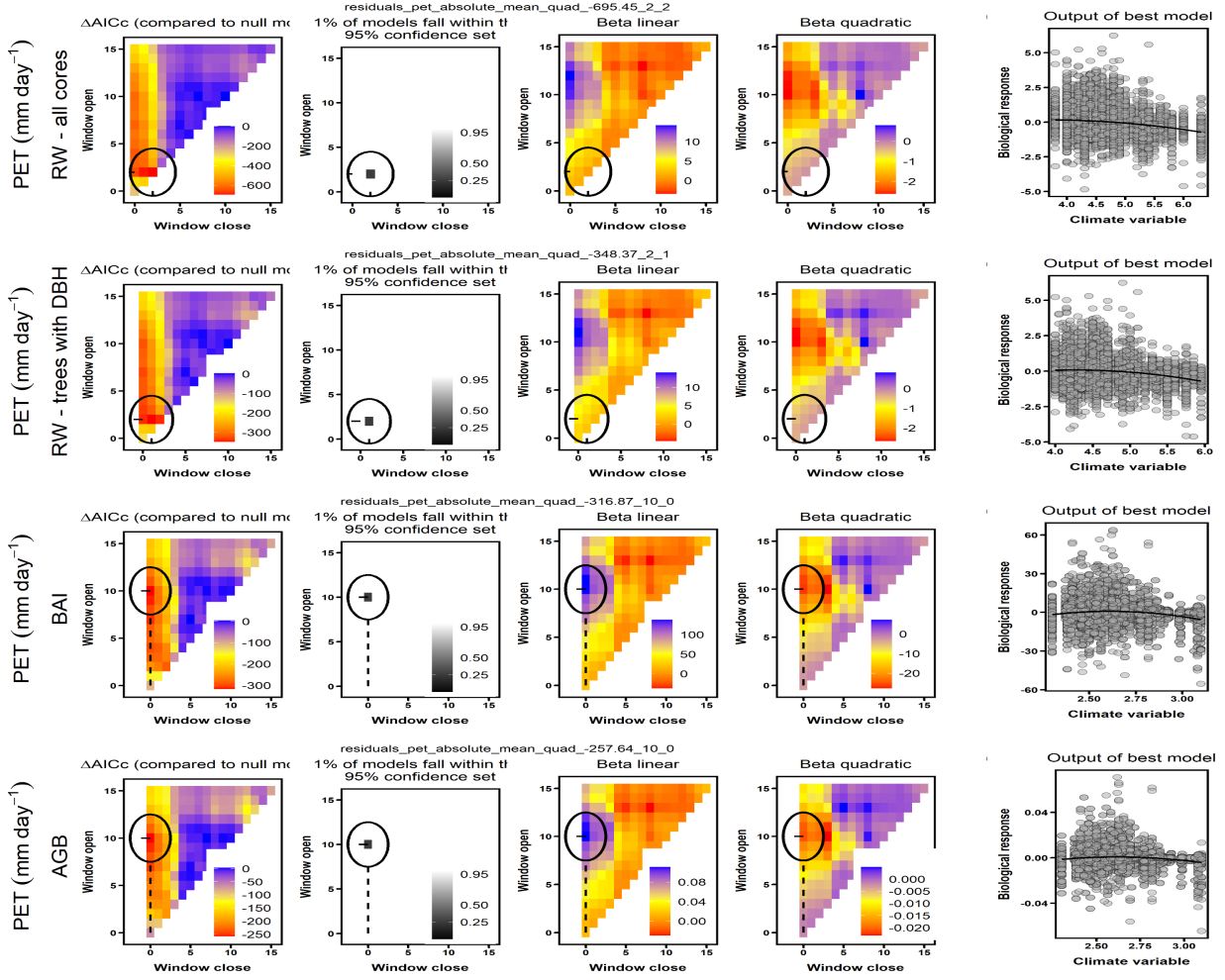


Figure S22. Climwin output for temperature variable group at LDW. Rows correspond to the four different models run: (1) all *RW* data, (2) *RW* for the subset of cores for which $\$DBH$ could be reconstructed, (3) *BAI*, and (4) *AGB* growth. The first four columns give statistics for time windows tested in *climwin*, where window open and close indicate months prior to current August. Difference in *AIC* relative to a model with no climate term (first column) is used to select the optimal time window (second column). The third and fourth columns give values of linear and quadratic terms for each time window. The final column shows the correlation of individual-level residuals to the selected climate variable, with the function fit in *climwin* (not the final fit).

Figure S23. Climwin output for water variable group at HF.

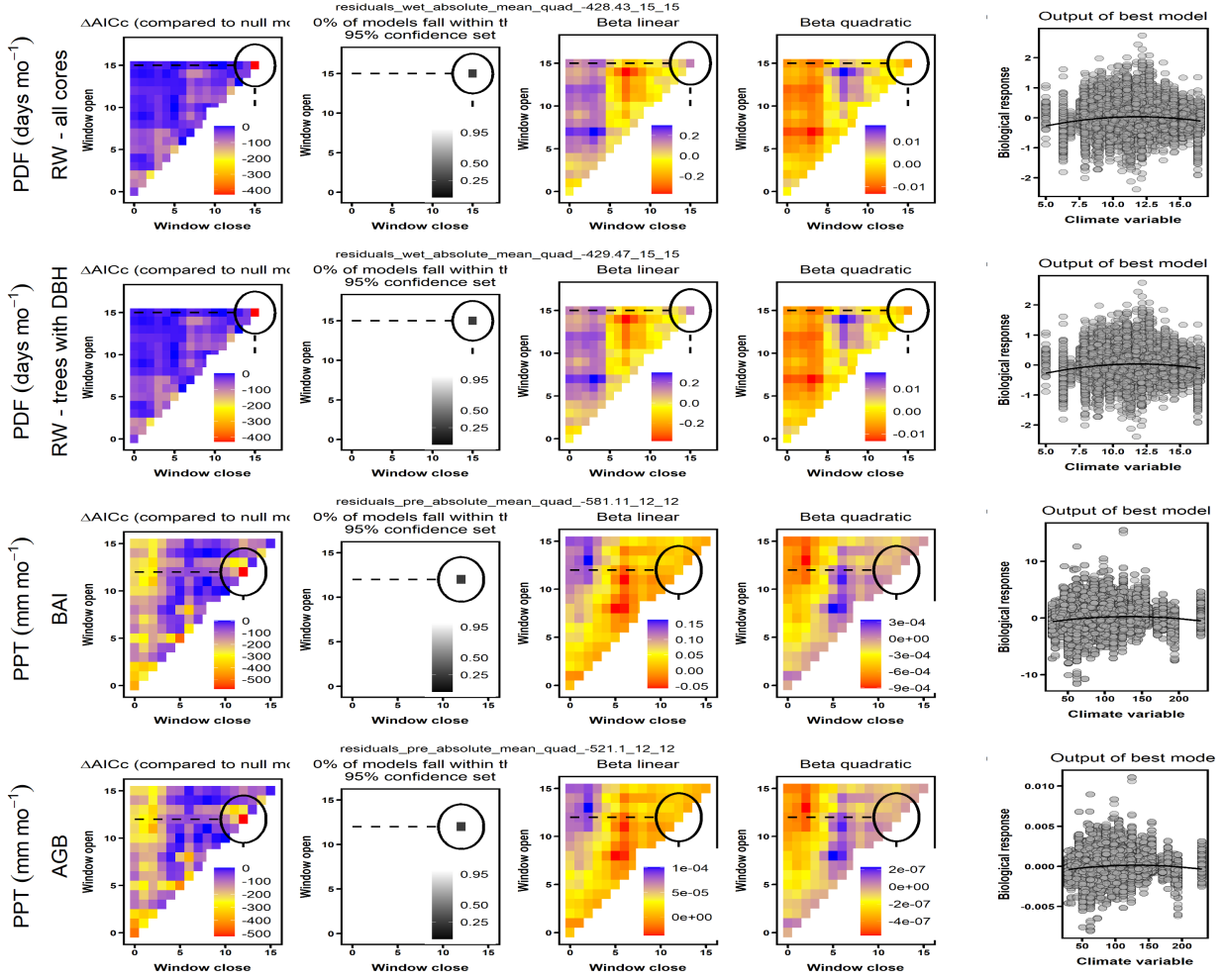


Figure S23. Climwin output for water variable group at HF. Rows correspond to the four different models run: (1) all *RW* data, (2) *RW* for the subset of cores for which \$DBH could be reconstructed, (3) *BAI*, and (4) *AGB* growth. The first four columns give statistics for time windows tested in *climwin*, where window open and close indicate months prior to current August. Difference in *AIC* relative to a model with no climate term (first column) is used to select the optimal time window (second column). The third and fourth columns give values of linear and quadratic terms for each time window. The final column shows the correlation of individual-level residuals to the selected climate variable, with the function fit in *climwin* (not the final fit).

Figure S23. Climwin output for temperature variable group at HF.

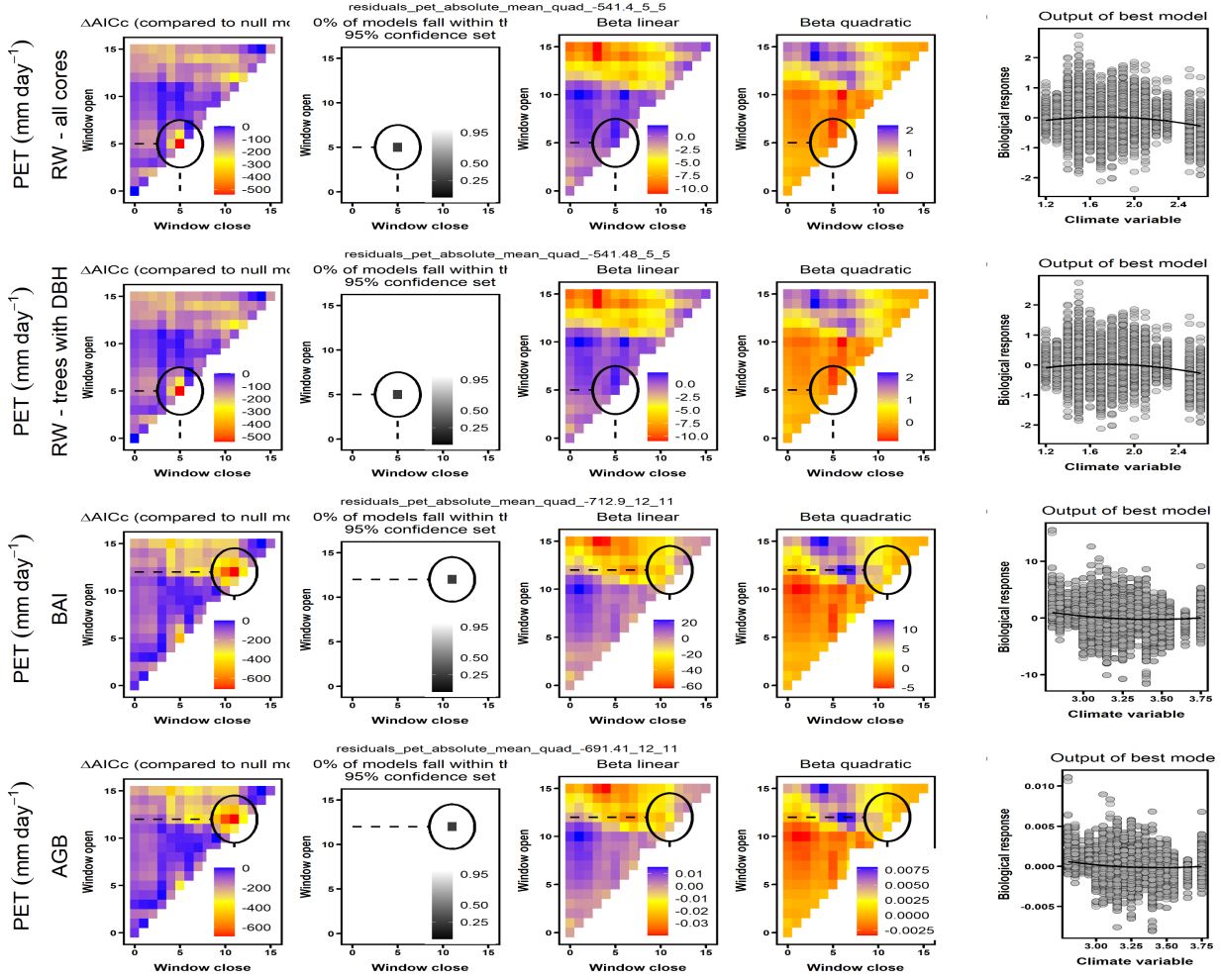


Figure S23. Climwin output for temperature variable group at HF. Rows correspond to the four different models run: (1) all *RW* data, (2) *RW* for the subset of cores for which $\$DBH$ could be reconstructed, (3) *BAI*, and (4) *AGB* growth. The first four columns give statistics for time windows tested in *climwin*, where window open and close indicate months prior to current August. Difference in *AIC* relative to a model with no climate term (first column) is used to select the optimal time window (second column). The third and fourth columns give values of linear and quadratic terms for each time window. The final column shows the correlation of individual-level residuals to the selected climate variable, with the function fit in *climwin* (not the final fit).

Figure S25. Climwin output for water variable group at ZOF.

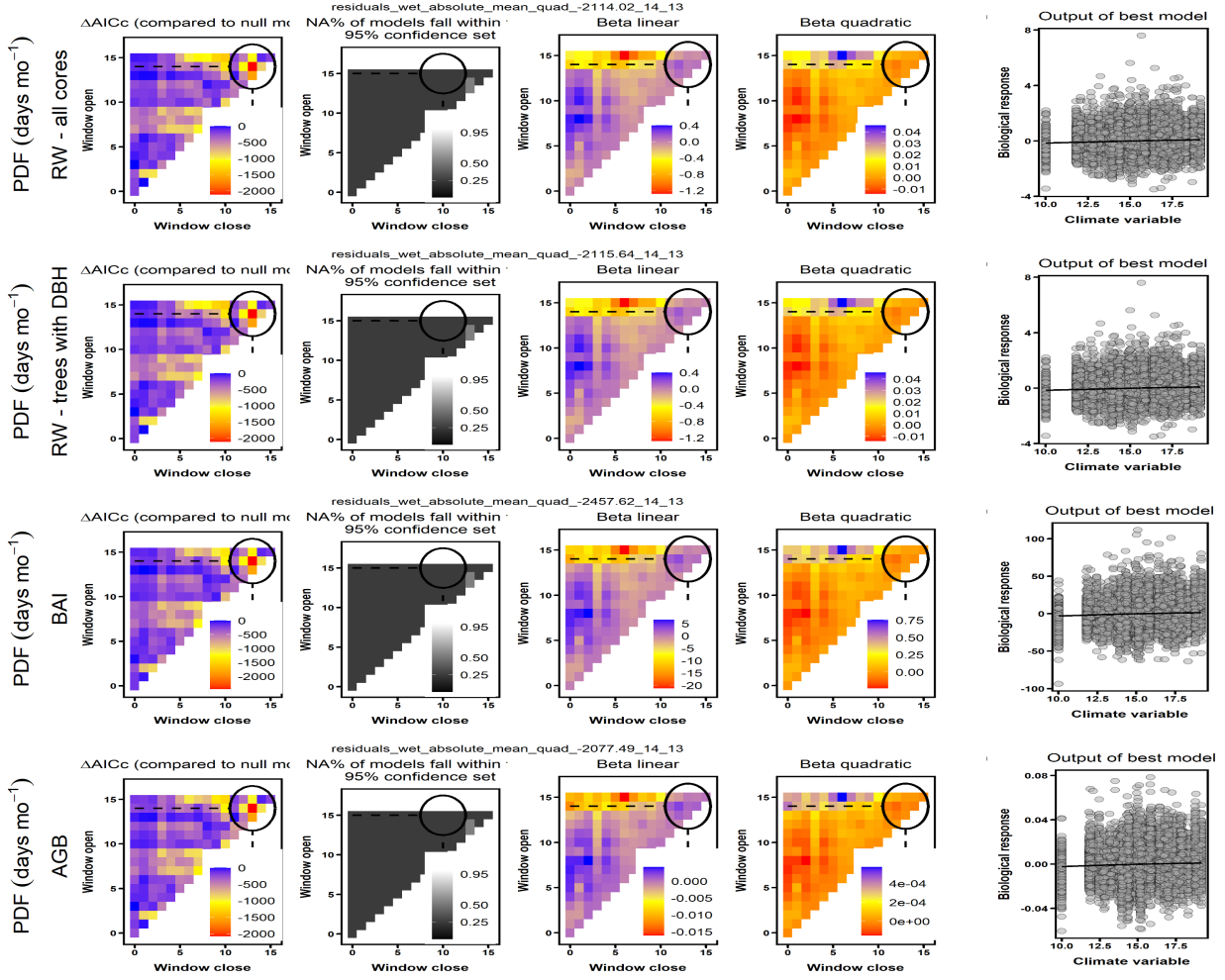


Figure S25. Climwin output for water variable group at ZOF. Rows correspond to the four different models run: (1) all *RW* data, (2) *RW* for the subset of cores for which \$DBH could be reconstructed, (3) *BAI*, and (4) *AGB* growth. The first four columns give statistics for time windows tested in *climwin*, where window open and close indicate months prior to current August. Difference in *AIC* relative to a model with no climate term (first column) is used to select the optimal time window (second column). The third and fourth columns give values of linear and quadratic terms for each time window. The final column shows the correlation of individual-level residuals to the selected climate variable, with the function fit in *climwin* (not the final fit).

Figure S26. Climwin output for temperature variable group at ZOF.

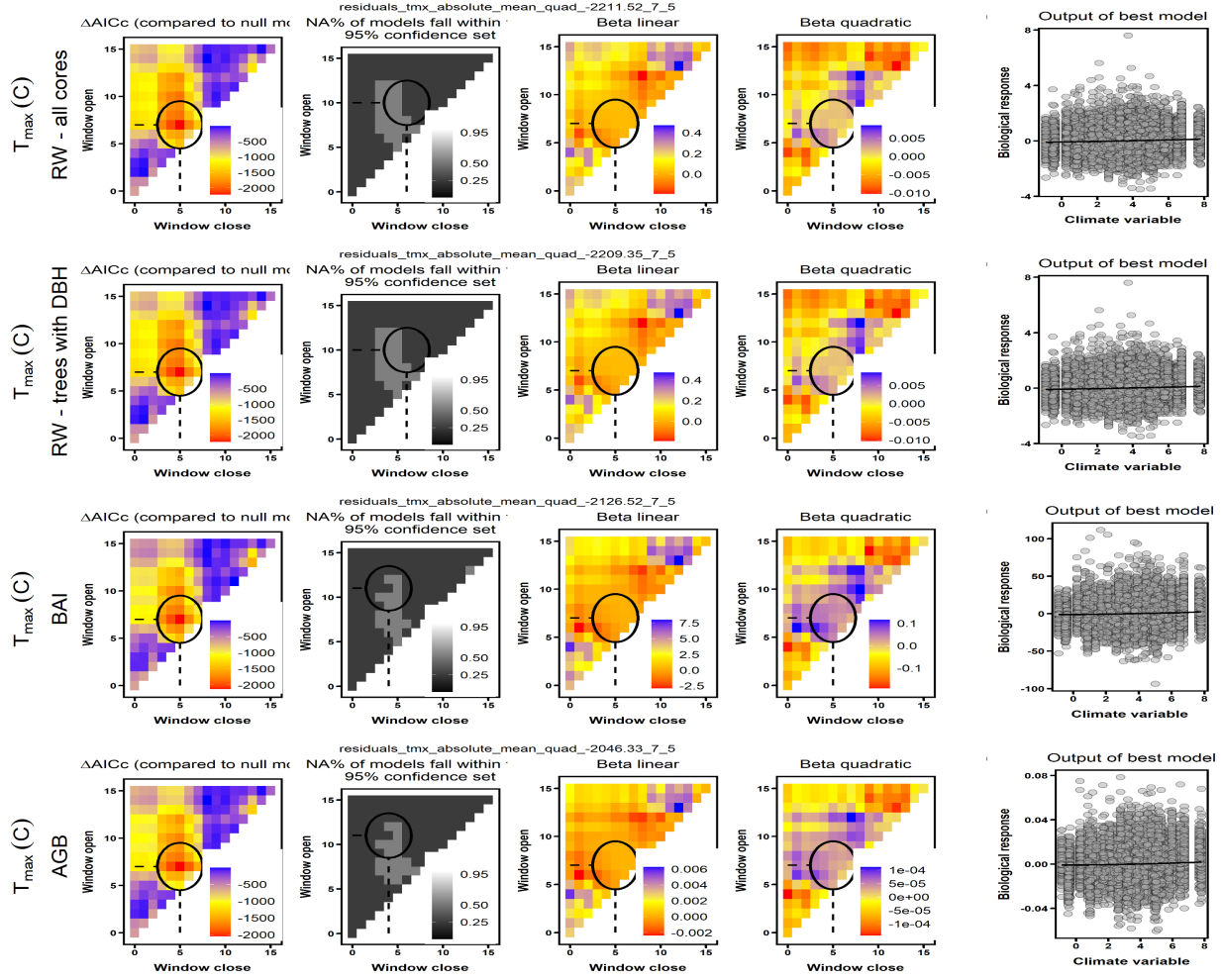


Figure S26. Climwin output for temperature variable group at ZOF. Rows correspond to the four different models run: (1) all *RW* data, (2) *RW* for the subset of cores for which $\$DBH$ could be reconstructed, (3) *BAI*, and (4) *AGB* growth. The first four columns give statistics for time windows tested in *climwin*, where window open and close indicate months prior to current August. Difference in *AIC* relative to a model with no climate term (first column) is used to select the optimal time window (second column). The third and fourth columns give values of linear and quadratic terms for each time window. The final column shows the correlation of individual-level residuals to the selected climate variable, with the function fit in *climwin* (not the final fit).

Figure S27. Climwin output for water variable group at NIO.

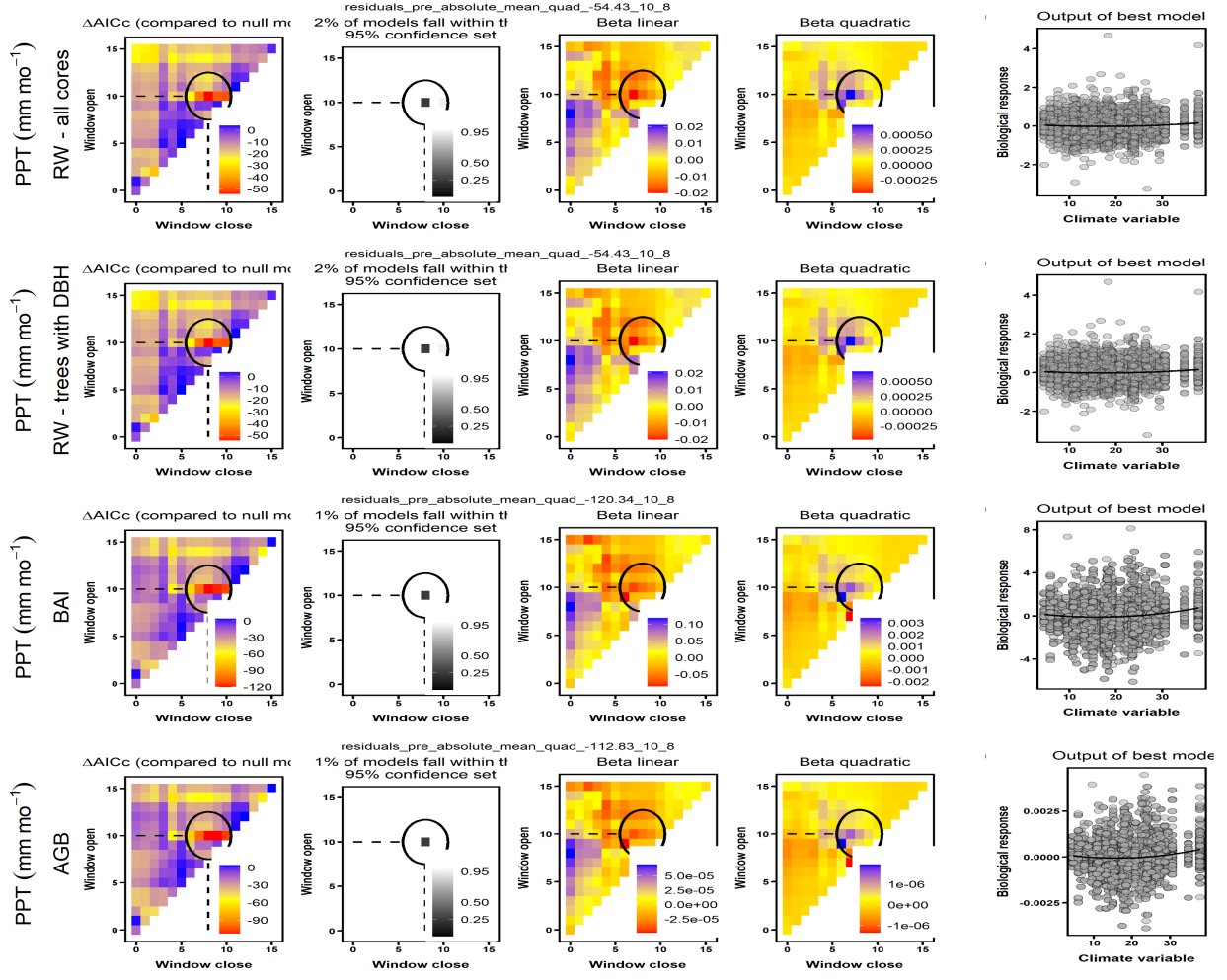


Figure S27. Climwin output for water variable group at NIO. Rows correspond to the four different models run: (1) all *RW* data, (2) *RW* for the subset of cores for which \$DBH could be reconstructed, (3) *BAI*, and (4) *AGB* growth. The first four columns give statistics for time windows tested in *climwin*, where window open and close indicate months prior to current August. Difference in *AIC* relative to a model with no climate term (first column) is used to select the optimal time window (second column). The third and fourth columns give values of linear and quadratic terms for each time window. The final column shows the correlation of individual-level residuals to the selected climate variable, with the function fit in *climwin* (not the final fit).

Figure S28. Climwin output for temperature variable group at NIO.

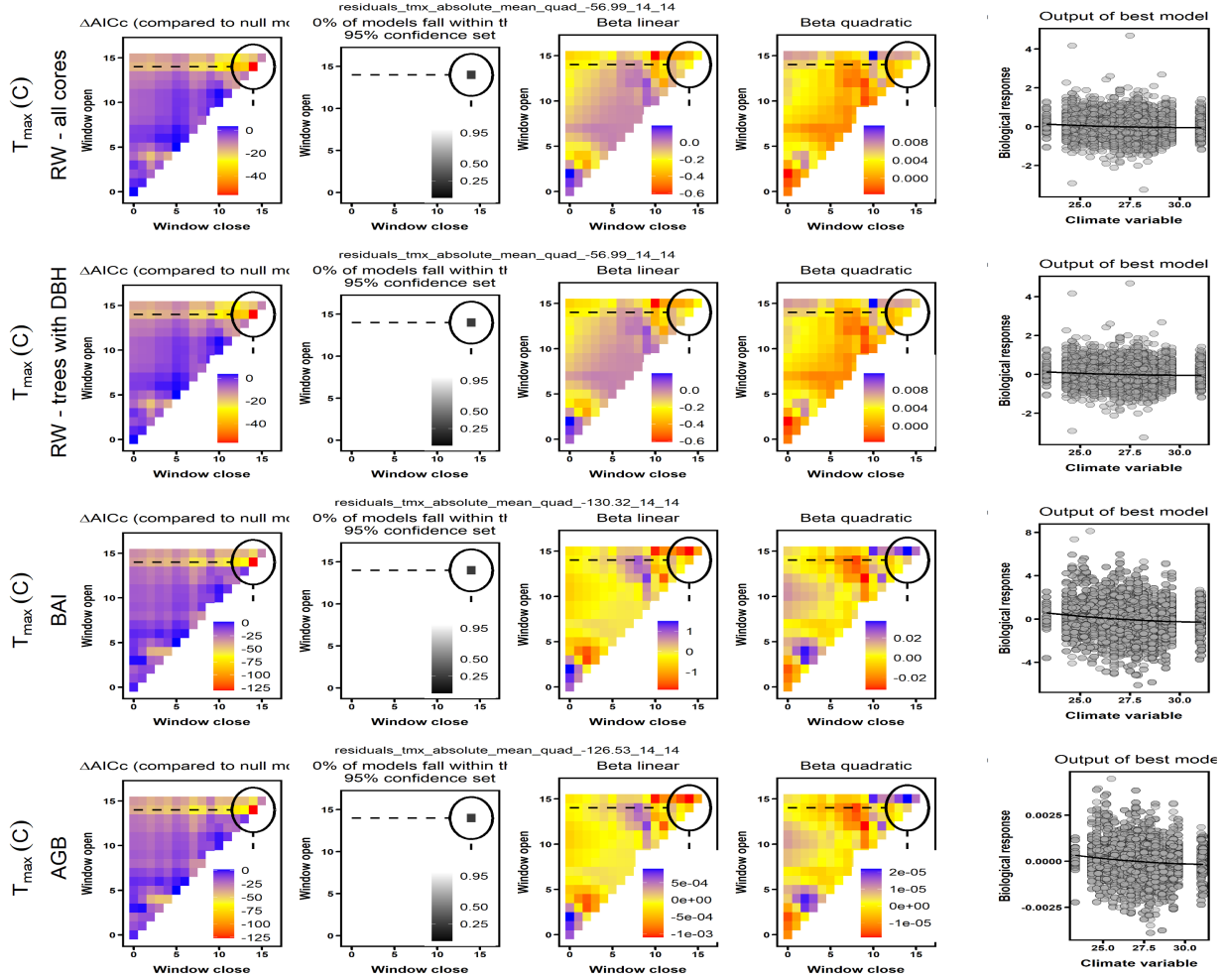


Figure S28. Climwin output for temperature variable group at NIO. Rows correspond to the four different models run: (1) all *RW* data, (2) *RW* for the subset of cores for which $\$DBH$ could be reconstructed, (3) *BAI*, and (4) *AGB* growth. The first four columns give statistics for time windows tested in *climwin*, where window open and close indicate months prior to current August. Difference in *AIC* relative to a model with no climate term (first column) is used to select the optimal time window (second column). The third and fourth columns give values of linear and quadratic terms for each time window. The final column shows the correlation of individual-level residuals to the selected climate variable, with the function fit in *climwin* (not the final fit).

Figure S29. Climwin output for water variable group at LT.

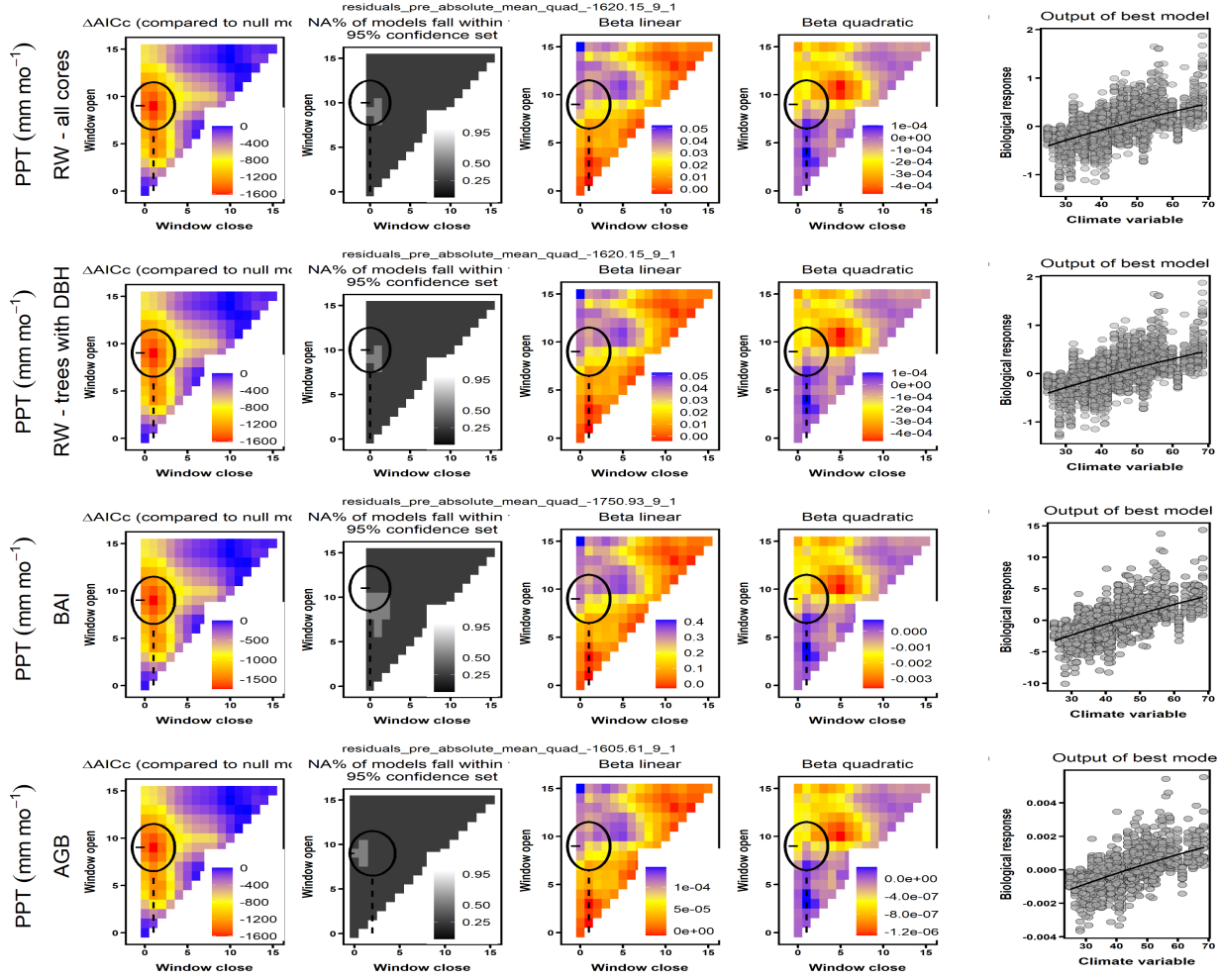


Figure S29. Climwin output for water variable group at LT. Rows correspond to the four different models run: (1) all *RW* data, (2) *RW* for the subset of cores for which \$DBH could be reconstructed, (3) *BAI*, and (4) *AGB* growth. The first four columns give statistics for time windows tested in *climwin*, where window open and close indicate months prior to current August. Difference in *AIC* relative to a model with no climate term (first column) is used to select the optimal time window (second column). The third and fourth columns give values of linear and quadratic terms for each time window. The final column shows the correlation of individual-level residuals to the selected climate variable, with the function fit in *climwin* (not the final fit).

Figure S30. Climwin output for temperature variable group at LT.

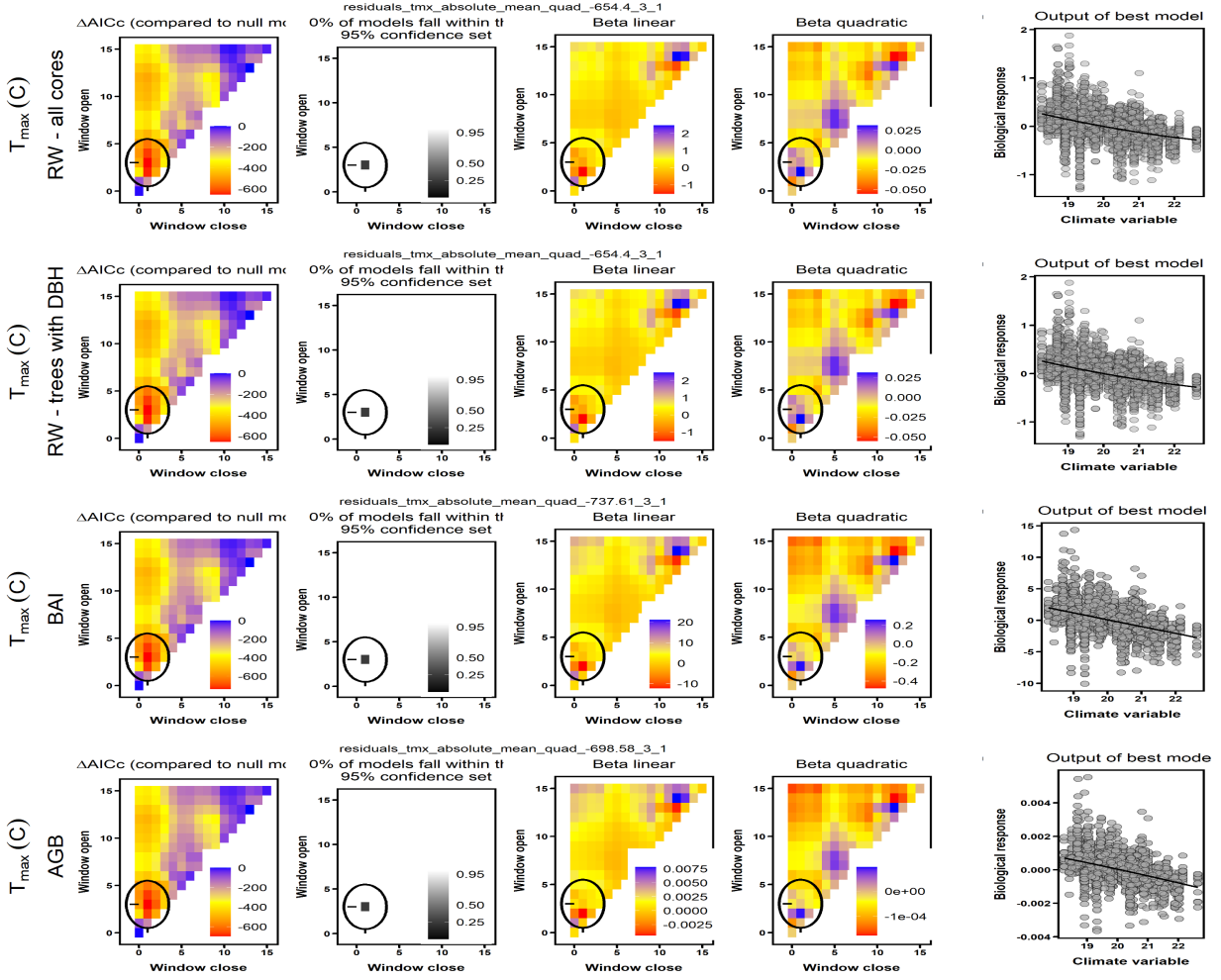


Figure S30. Climwin output for temperature variable group at LT. Rows correspond to the four different models run: (1) all *RW* data, (2) *RW* for the subset of cores for which $\$DBH$ could be reconstructed, (3) *BAI*, and (4) *AGB* growth. The first four columns give statistics for time windows tested in *climwin*, where window open and close indicate months prior to current August. Difference in *AIC* relative to a model with no climate term (first column) is used to select the optimal time window (second column). The third and fourth columns give values of linear and quadratic terms for each time window. The final column shows the correlation of individual-level residuals to the selected climate variable, with the function fit in *climwin* (not the final fit).

Figure S31. Climwin output for water variable group at CB.

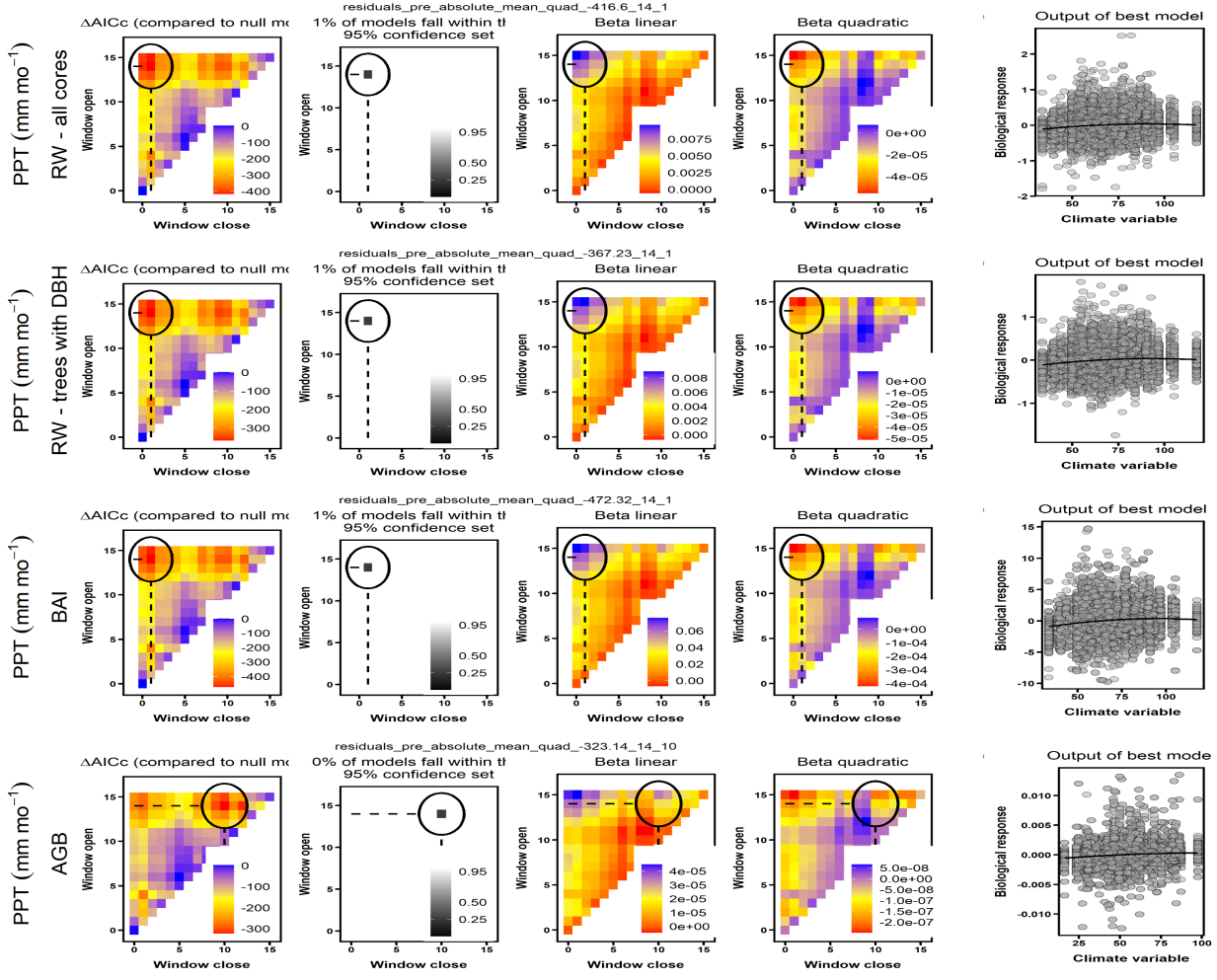


Figure S31. Climwin output for water variable group at CB. Rows correspond to the four different models run: (1) all *RW* data, (2) *RW* for the subset of cores for which \$DBH could be reconstructed, (3) *BAI*, and (4) *AGB* growth. The first four columns give statistics for time windows tested in *climwin*, where window open and close indicate months prior to current August. Difference in *AIC* relative to a model with no climate term (first column) is used to select the optimal time window (second column). The third and fourth columns give values of linear and quadratic terms for each time window. The final column shows the correlation of individual-level residuals to the selected climate variable, with the function fit in *climwin* (not the final fit).

Figure S32. Climwin output for temperature variable group at CB.

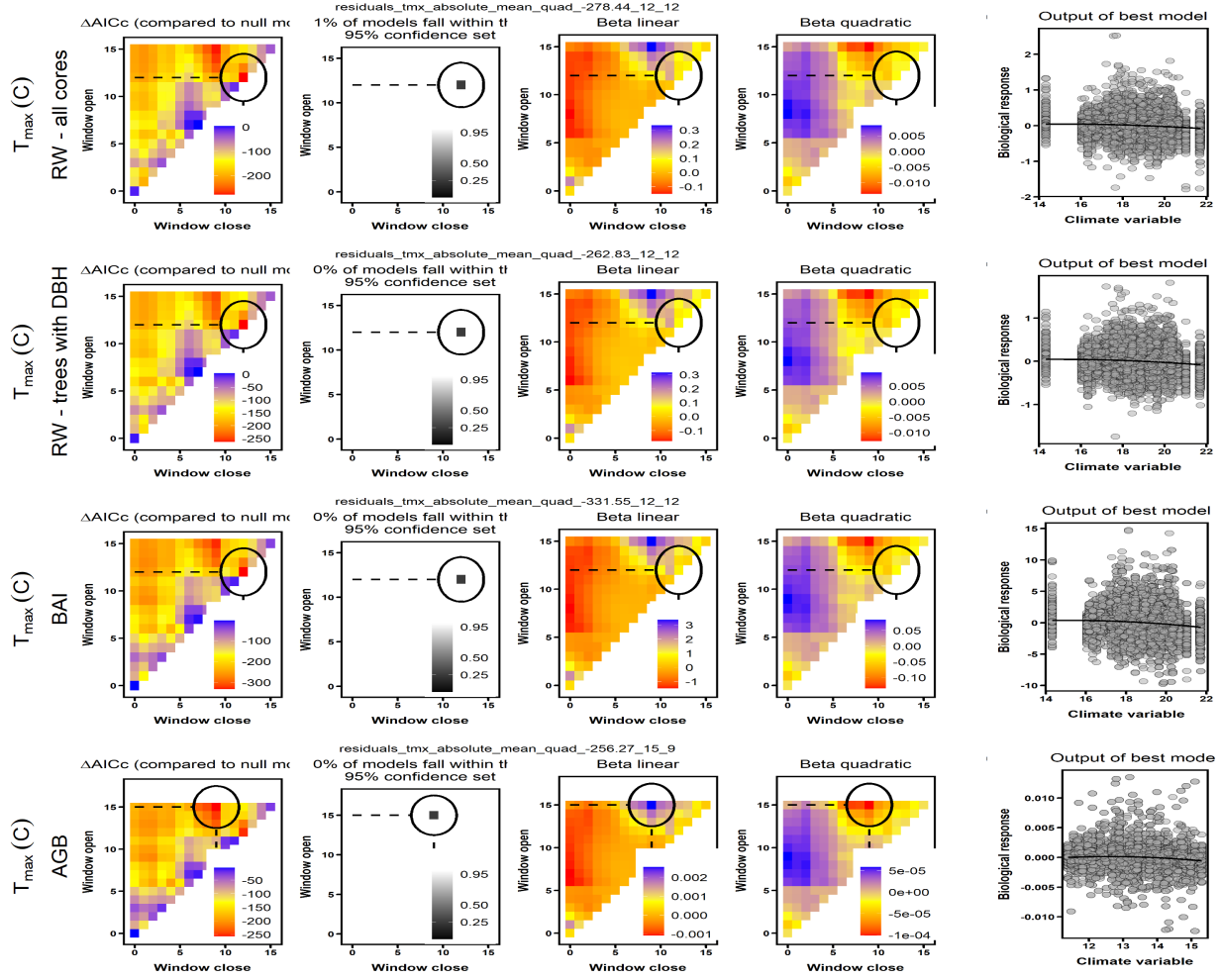


Figure S32. Climwin output for temperature variable group at CB. Rows correspond to the four different models run: (1) all *RW* data, (2) *RW* for the subset of cores for which \$DBH could be reconstructed, (3) *BAI*, and (4) *AGB* growth. The first four columns give statistics for time windows tested in *climwin*, where window open and close indicate months prior to current August. Difference in *AIC* relative to a model with no climate term (first column) is used to select the optimal time window (second column). The third and fourth columns give values of linear and quadratic terms for each time window. The final column shows the correlation of individual-level residuals to the selected climate variable, with the function fit in *climwin* (not the final fit).

Figure S33. Climwin output for water variable group at SC.

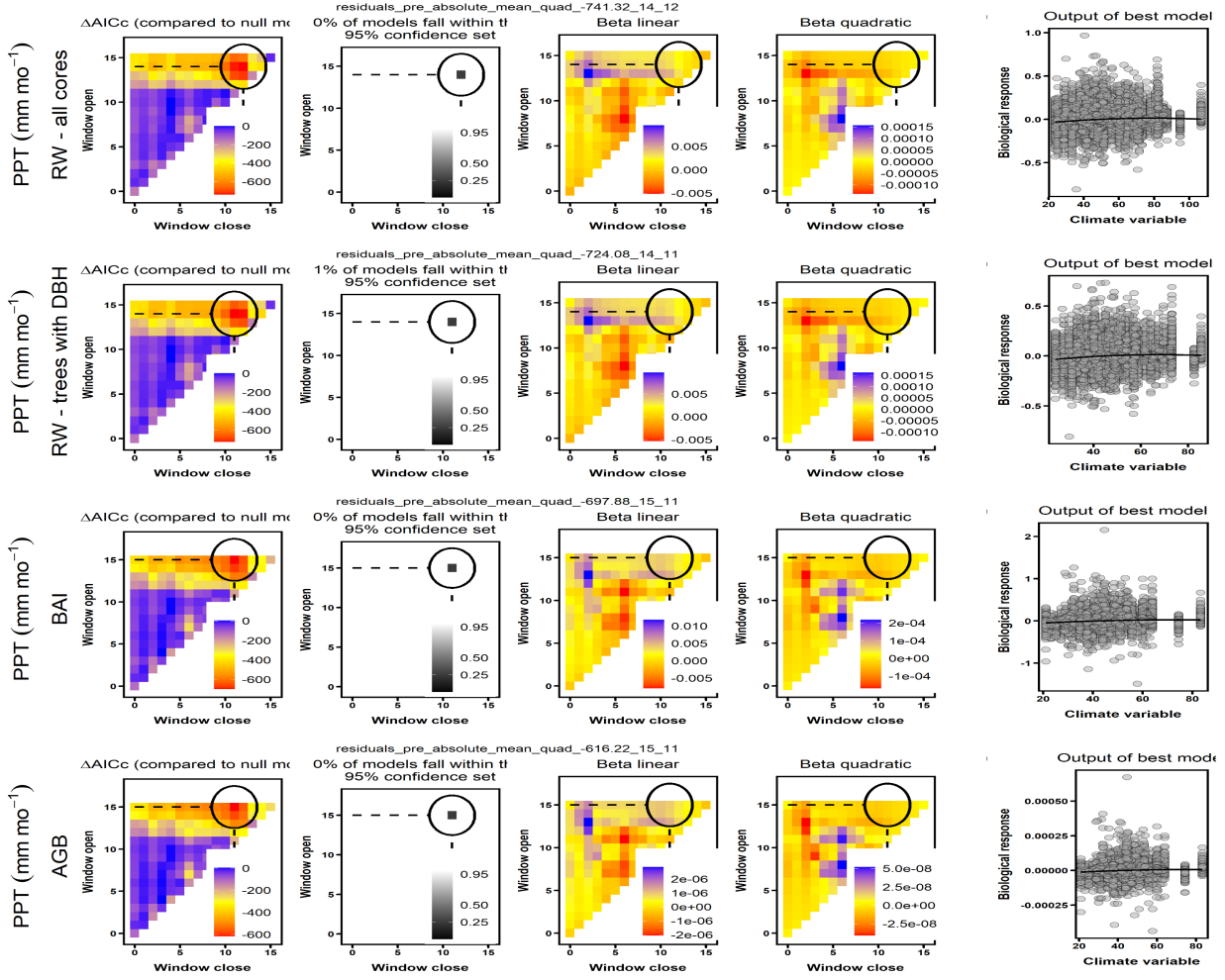


Figure S33. Climwin output for water variable group at SC. Rows correspond to the four different models run: (1) all *RW* data, (2) *RW* for the subset of cores for which \$DBH could be reconstructed, (3) *BAI*, and (4) *AGB* growth. The first four columns give statistics for time windows tested in *climwin*, where window open and close indicate months prior to current August. Difference in *AIC* relative to a model with no climate term (first column) is used to select the optimal time window (second column). The third and fourth columns give values of linear and quadratic terms for each time window. The final column shows the correlation of individual-level residuals to the selected climate variable, with the function fit in *climwin* (not the final fit).

Figure S34. Climwin output for temperature variable group at SC.

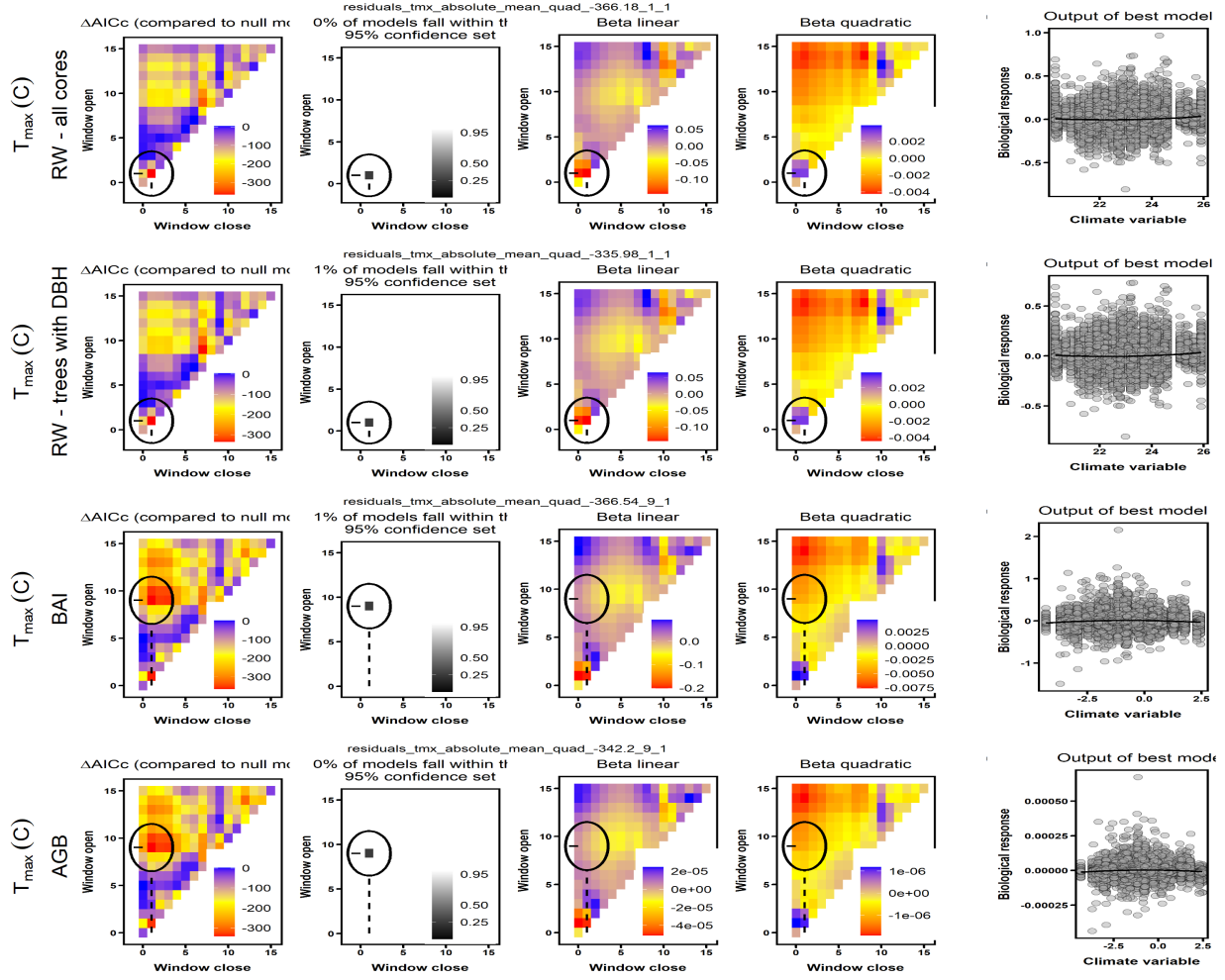


Figure S34. Climwin output for temperature variable group at SC. Rows correspond to the four different models run: (1) all *RW* data, (2) *RW* for the subset of cores for which $\$DBH$ could be reconstructed, (3) *BAI*, and (4) *AGB* growth. The first four columns give statistics for time windows tested in *climwin*, where window open and close indicate months prior to current August. Difference in *AIC* relative to a model with no climate term (first column) is used to select the optimal time window (second column). The third and fourth columns give values of linear and quadratic terms for each time window. The final column shows the correlation of individual-level residuals to the selected climate variable, with the function fit in *climwin* (not the final fit).

Figure S35. Best GLS models including climate and *DBH* for BCNM

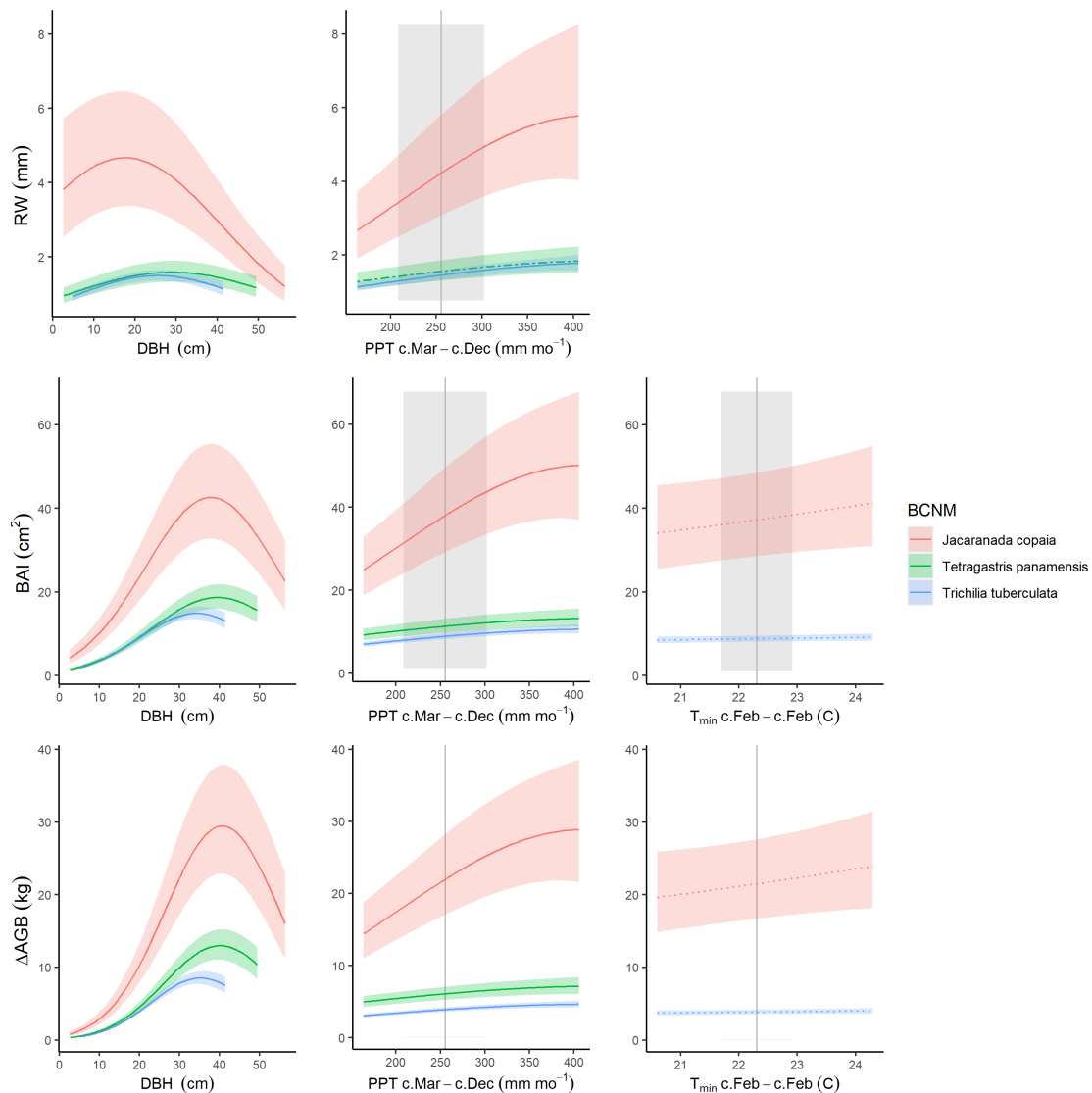


Figure S35. Best GLS models including climate and *DBH* for BCNM for all three growth metrics examined here. For each species that met the criteria for inclusion in the analysis, relationships are plotted if included in top model. For each relationship shown, other terms in the model are held constant at their median. Best-fit polynomials are plotted with solid lines when both first- and second-order terms are significant (t-test's p-value <0.05), dashed lines when only one term is significant, and dotted lines when neither is significant. *Climwin*-selected climate variables are coded on the x-axes as the climate variable name followed by the range of months (p=previous year, c=current year) over which it is most influential. Vertical grey lines indicate the long-term mean for the climate variable, shading indicates 1 SD.

Figure S36. Best GLS models including climate, DBH, and year for BCNM

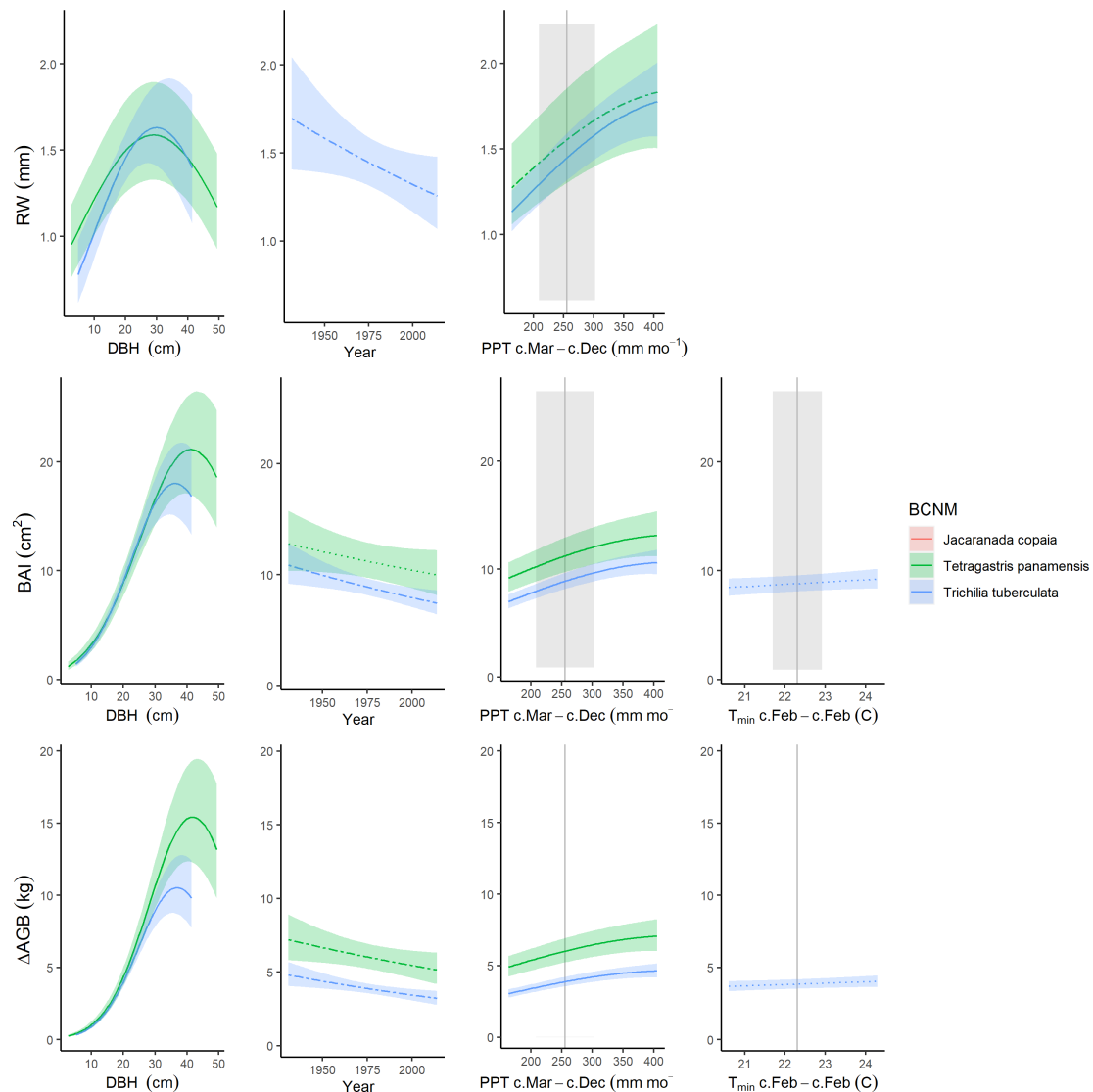


Figure S36. Best GLS models including climate, DBH, and year for BCNM for all three growth metrics examined here. For each species that met the criteria for inclusion in the analysis, relationships are plotted if included in top model. For each relationship shown, other terms in the model are held constant at their median. Best-fit polynomials are plotted with solid lines when both first- and second-order terms are significant (*t*-test's p-value <0.05), dashed lines when only one term is significant, and dotted lines when neither is significant. *Climwin*-selected climate variables are coded on the x-axes as the climate variable name followed by the range of months (p=previous year, c=current year) over which it is most influential. Vertical grey lines indicate the long-term mean for the climate variable, shading indicates 1 SD.

Figure S37. Best GLS models including climate and *DBH* for HKK

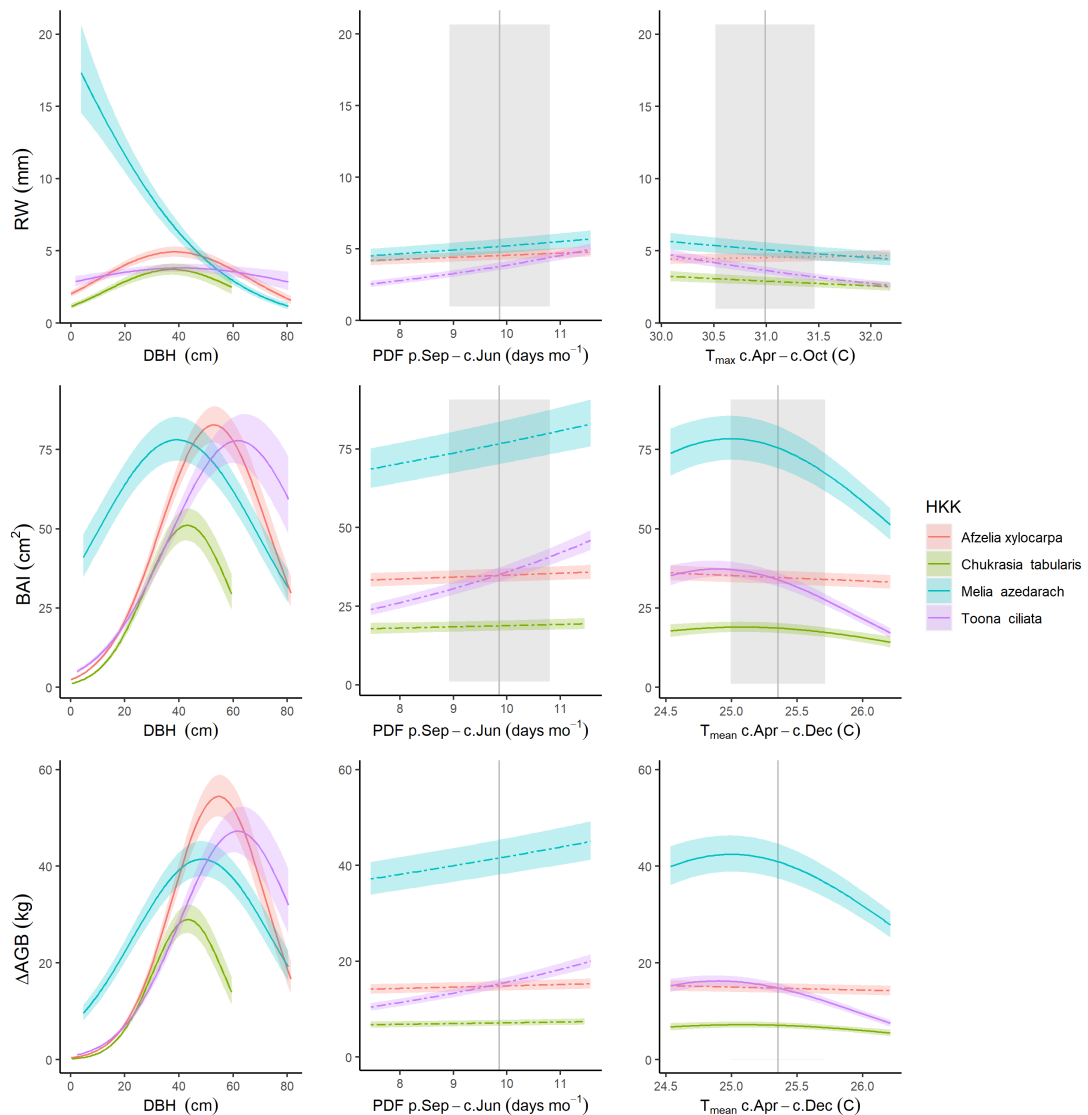


Figure S37. Best GLS models including climate and *DBH* for HKK for all three growth metrics examined here. For each species that met the criteria for inclusion in the analysis, relationships are plotted if included in top model. For each relationship shown, other terms in the model are held constant at their median. Best-fit polynomials are plotted with solid lines when both first- and second-order terms are significant (*t*-test's *p*-value <0.05), dashed lines when only one term is significant, and dotted lines when neither is significant. *Climwin*-selected climate variables are coded on the x-axes as the climate variable name followed by the range of months (*p*=previous year, *c*=current year) over which it is most influential. Vertical grey lines indicate the long-term mean for the climate variable, shading indicates 1 SD.

Figure S38. Best GLS models including climate, DBH, and year for HKK

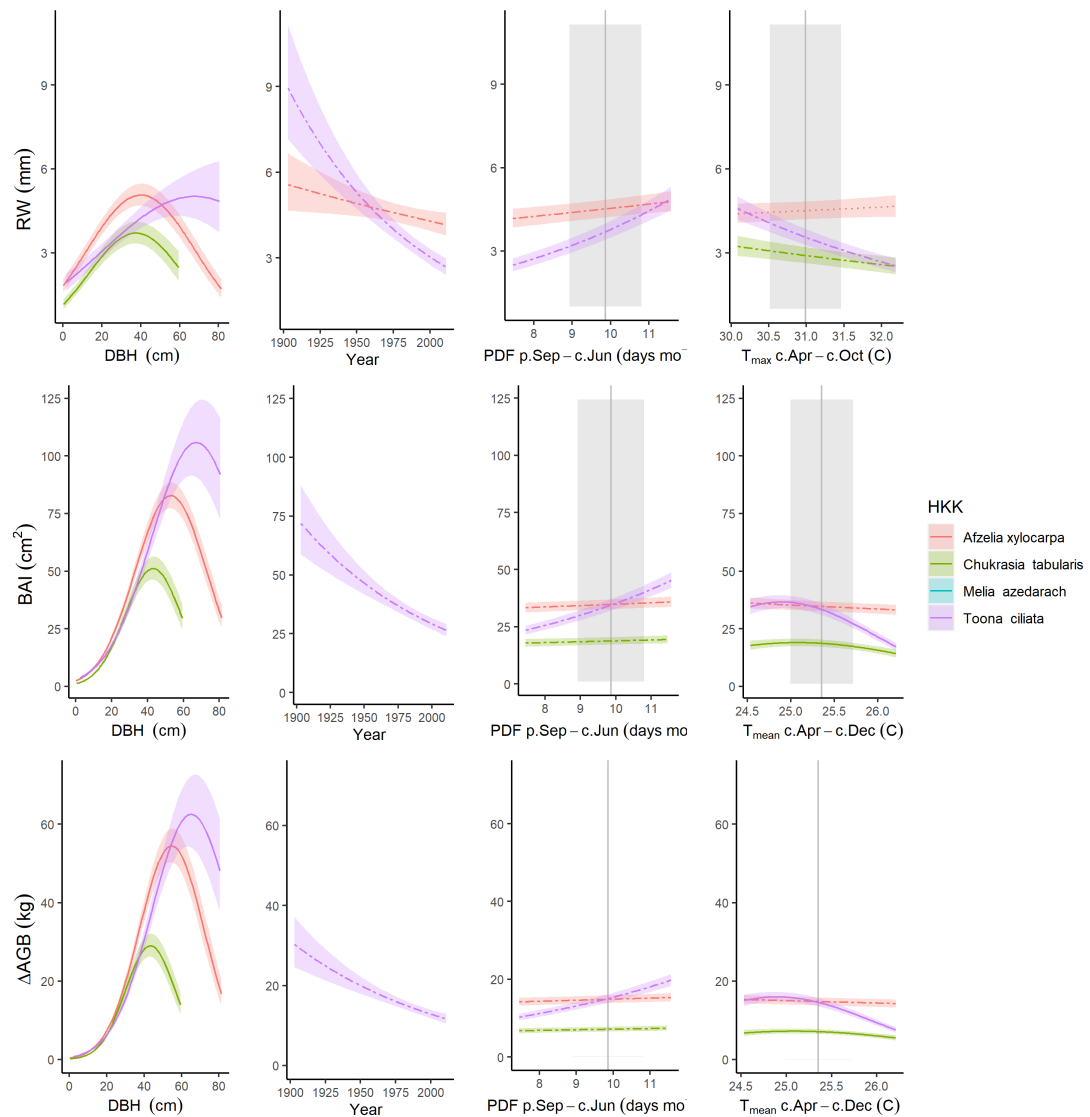


Figure S38. Best GLS models including climate, DBH, and year for HKK for all three growth metrics examined here. For each species that met the criteria for inclusion in the analysis, relationships are plotted if included in top model. For each relationship shown, other terms in the model are held constant at their median. Best-fit polynomials are plotted with solid lines when both first- and second-order terms are significant (t-test's p-value <0.05), dashed lines when only one term is significant, and dotted lines when neither is significant. Transparent ribbons indicate 95% confidence intervals. *Climwin*-selected climate variables are coded on the x-axes as the climate variable name followed by the range of months (p=previous year, c=current year) over which it is most influential. Vertical grey lines indicate the long-term mean for the climate variable, shading indicates 1 SD.

Figure S39. Best GLS models including climate and *DBH* for SCBI

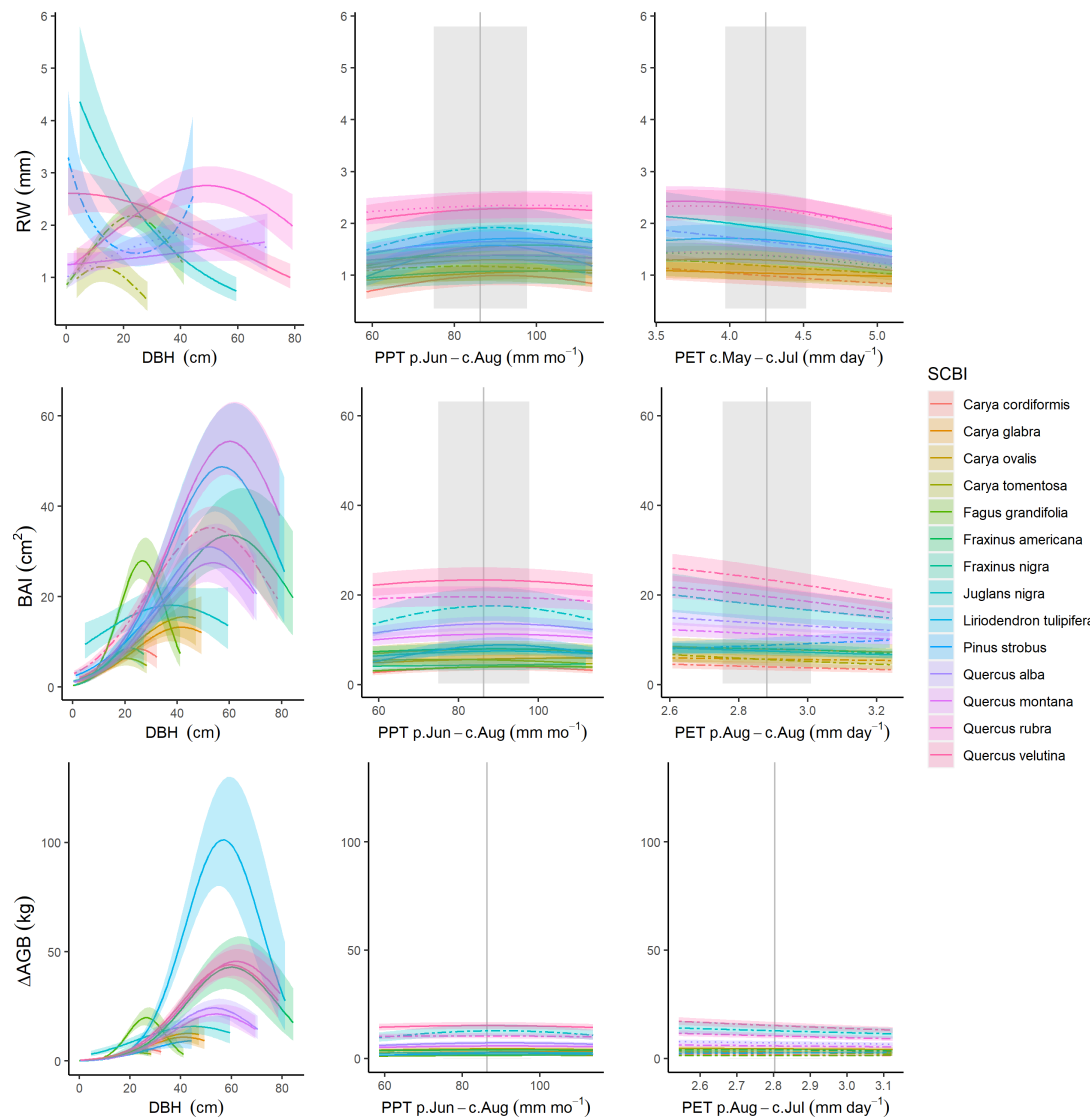


Figure S39. Best GLS models including climate and *DBH* for SCBI for all three growth metrics examined here. For each species that met the criteria for inclusion in the analysis, relationships are plotted if included in top model. For each relationship shown, other terms in the model are held constant at their median. Best-fit polynomials are plotted with solid lines when both first- and second-order terms are significant (*t*-test's *p*-value <0.05), dashed lines when only one term is significant, and dotted lines when neither is significant. *Climwin*-selected climate variables are coded on the x-axes as the climate variable name followed by the range of months (*p*=previous year, *c*=current year) over which it is most influential. Vertical grey lines indicate the long-term mean for the climate variable, shading indicates 1 SD.

Figure S40. Best GLS models including climate, DBH, and year for SCBI

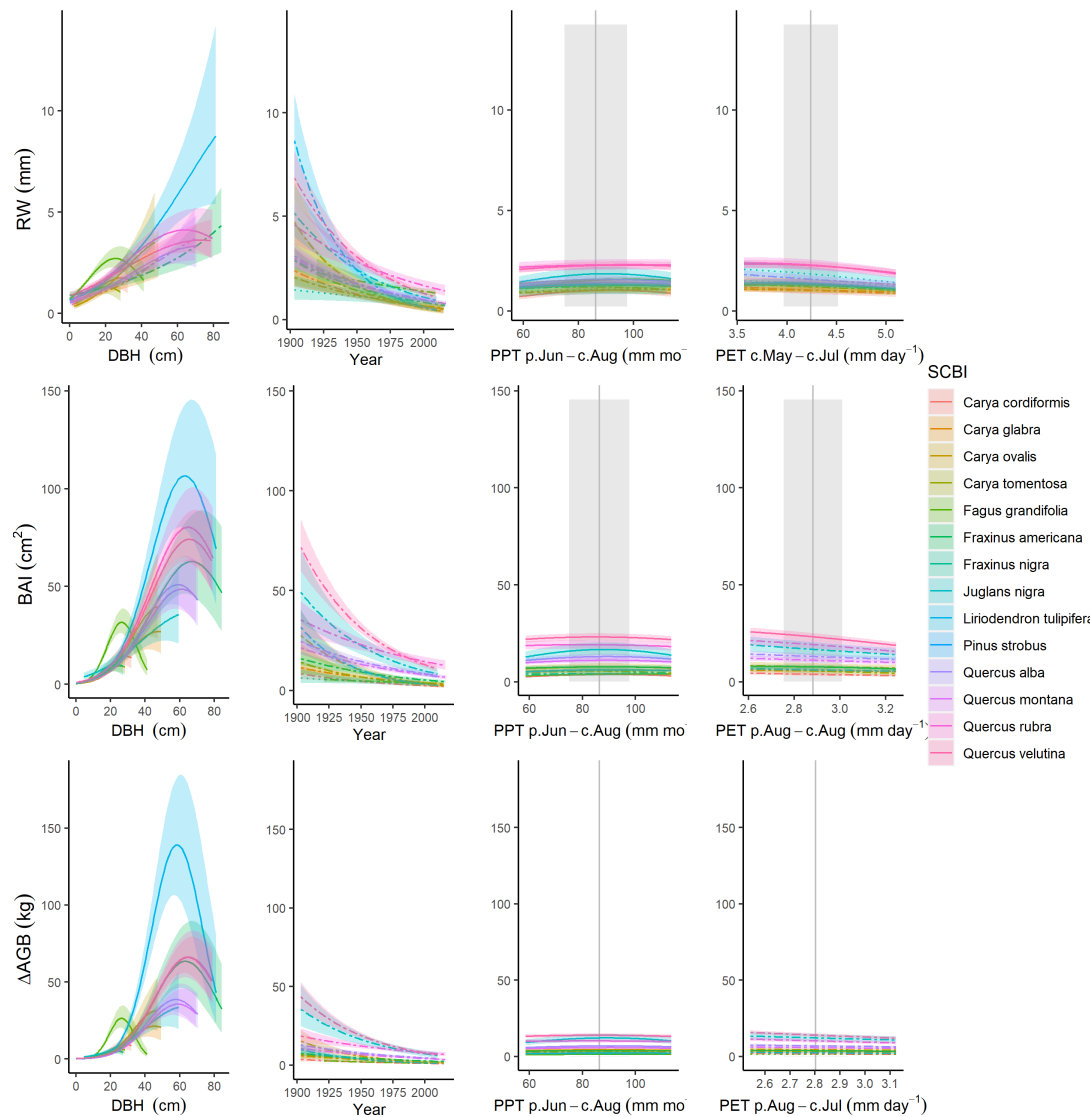


Figure S40. Best GLS models including climate, DBH, and year for SCBI for all three growth metrics examined here. For each species that met the criteria for inclusion in the analysis, relationships are plotted if included in top model. For each relationship shown, other terms in the model are held constant at their median. Best-fit polynomials are plotted with solid lines when both first- and second-order terms are significant (t-test's p-value <0.05), dashed lines when only one term is significant, and dotted lines when neither is significant. Transparent ribbons indicate 95% confidence intervals. *Climwin*-selected climate variables are coded on the x-axes as the climate variable name followed by the range of months (p=previous year, c=current year) over which it is most influential. Vertical grey lines indicate the long-term mean for the climate variable, shading indicates 1 SD.

Figure S41. Best GLS models including climate and *DBH* for LDW

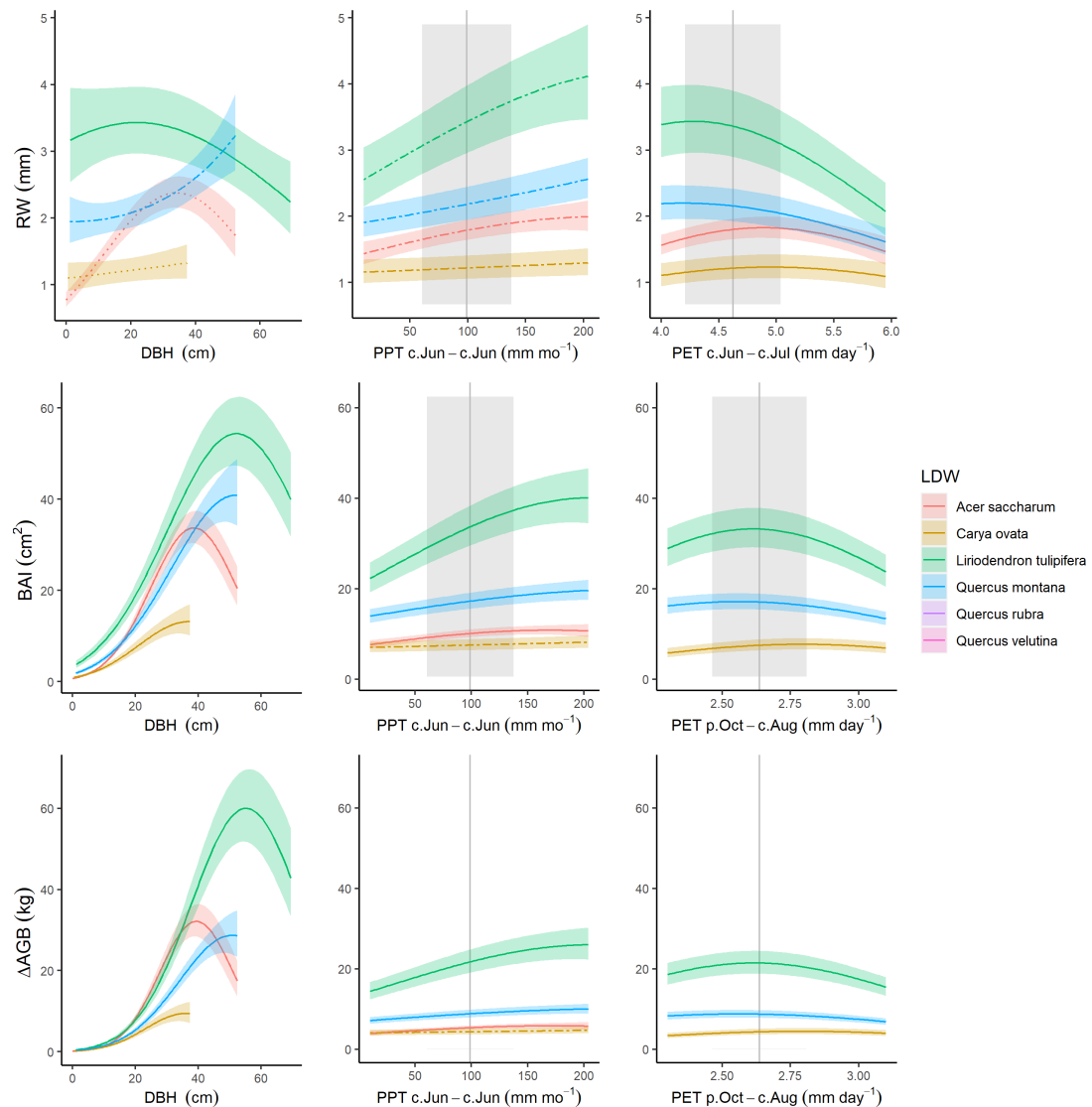


Figure S41. Best GLS models including climate and *DBH* for LDW for all three growth metrics examined here. For each species that met the criteria for inclusion in the analysis, relationships are plotted if included in top model. For each relationship shown, other terms in the model are held constant at their median. Best-fit polynomials are plotted with solid lines when both first- and second-order terms are significant (t-test's p-value <0.05), dashed lines when only one term is significant, and dotted lines when neither is significant. Transparent ribbons indicate 95% confidence intervals. *Climwin*-selected climate variables are coded on the x-axes as the climate variable name followed by the range of months (p=previous year, c=current year) over which it is most influential. Vertical grey lines indicate the long-term mean for the climate variable, shading indicates 1 SD.

Figure S42. Best GLS models including climate, DBH, and year for LDW

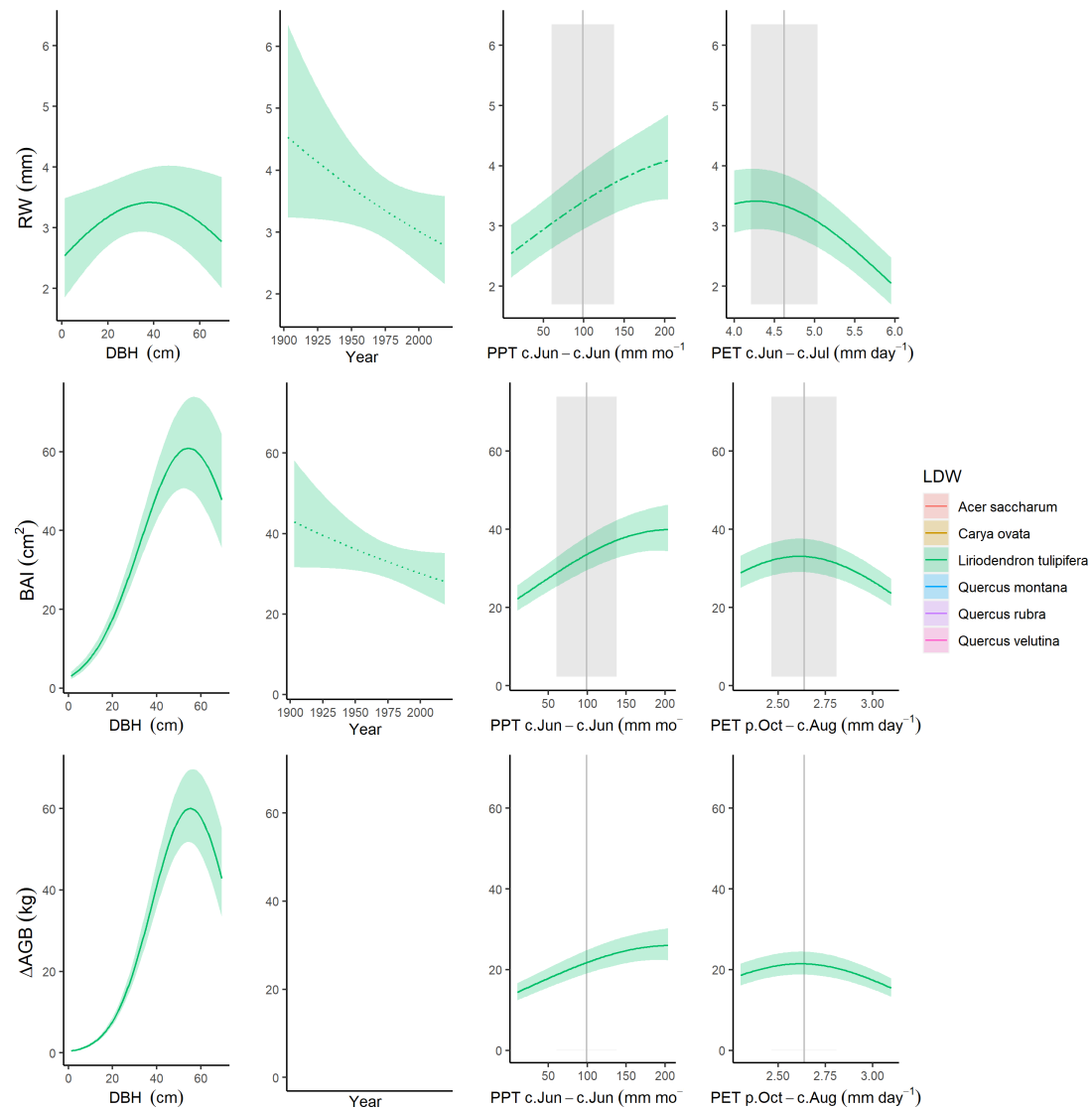


Figure S42. Best GLS models including climate, DBH, and year for LDW for all three growth metrics examined here. For each species that met the criteria for inclusion in the analysis, relationships are plotted if included in top model. For each relationship shown, other terms in the model are held constant at their median. Best-fit polynomials are plotted with solid lines when both first- and second-order terms are significant (*t*-test's p-value <0.05), dashed lines when only one term is significant, and dotted lines when neither is significant. Transparent ribbons indicate 95% confidence intervals. *Climwin*-selected climate variables are coded on the x-axes as the climate variable name followed by the range of months (p=previous year, c=current year) over which it is most influential. Vertical grey lines indicate the long-term mean for the climate variable, shading indicates 1 SD.

Figure S43. Best GLS models including climate and *DBH* for HF

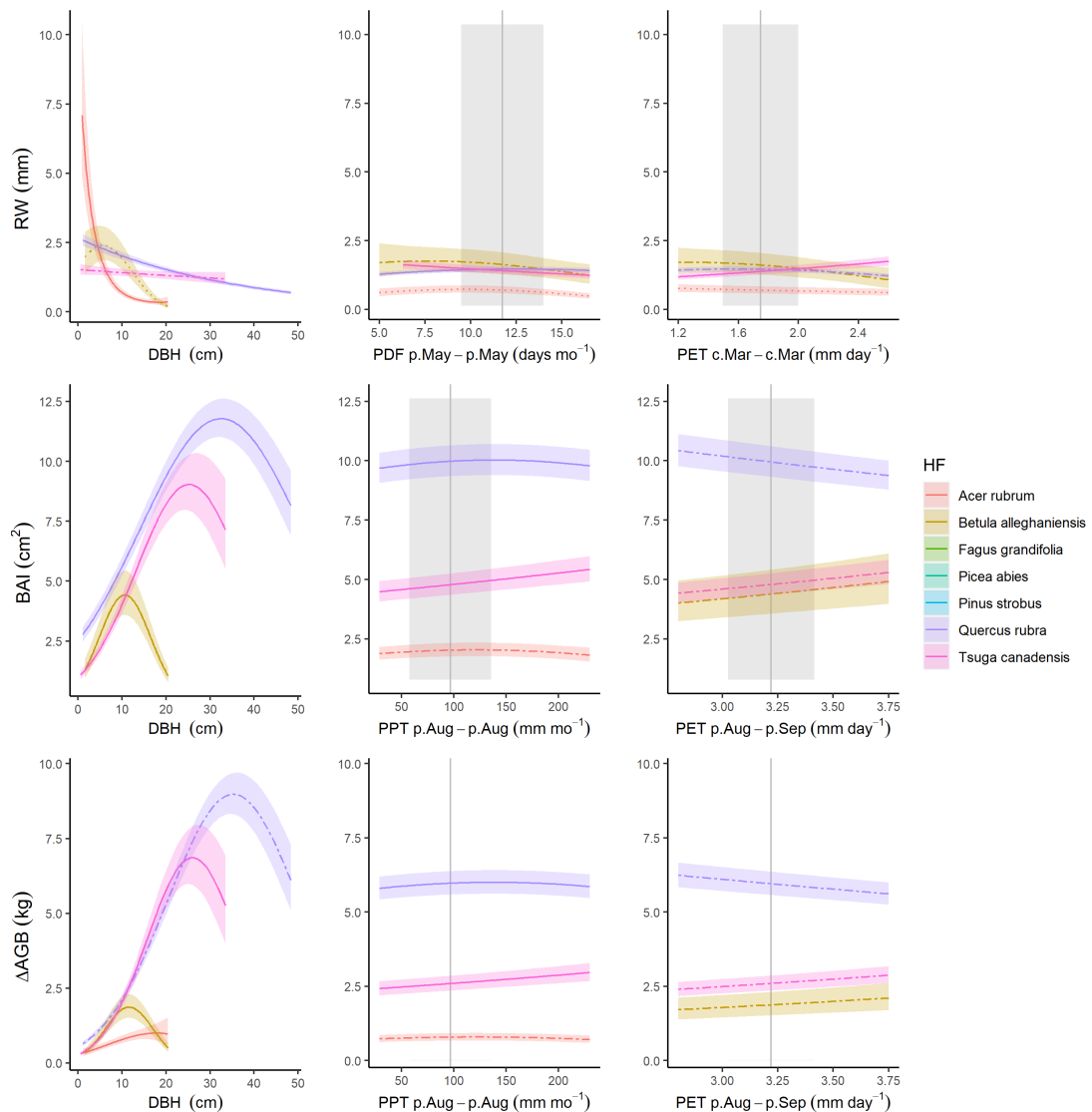


Figure S43. Best GLS models including climate and *DBH* for HF for all three growth metrics examined here. For each species that met the criteria for inclusion in the analysis, relationships are plotted if included in top model. For each relationship shown, other terms in the model are held constant at their median. Best-fit polynomials are plotted with solid lines when both first- and second-order terms are significant (*t*-test's *p*-value <0.05), dashed lines when only one term is significant, and dotted lines when neither is significant. Transparent ribbons indicate 95% confidence intervals. *Climwin*-selected climate variables are coded on the x-axes as the climate variable name followed by the range of months (*p*=previous year, *c*=current year) over which it is most influential. Vertical grey lines indicate the long-term mean for the climate variable, shading indicates 1 SD.

Figure S44. Best GLS models including climate, DBH, and year for HF

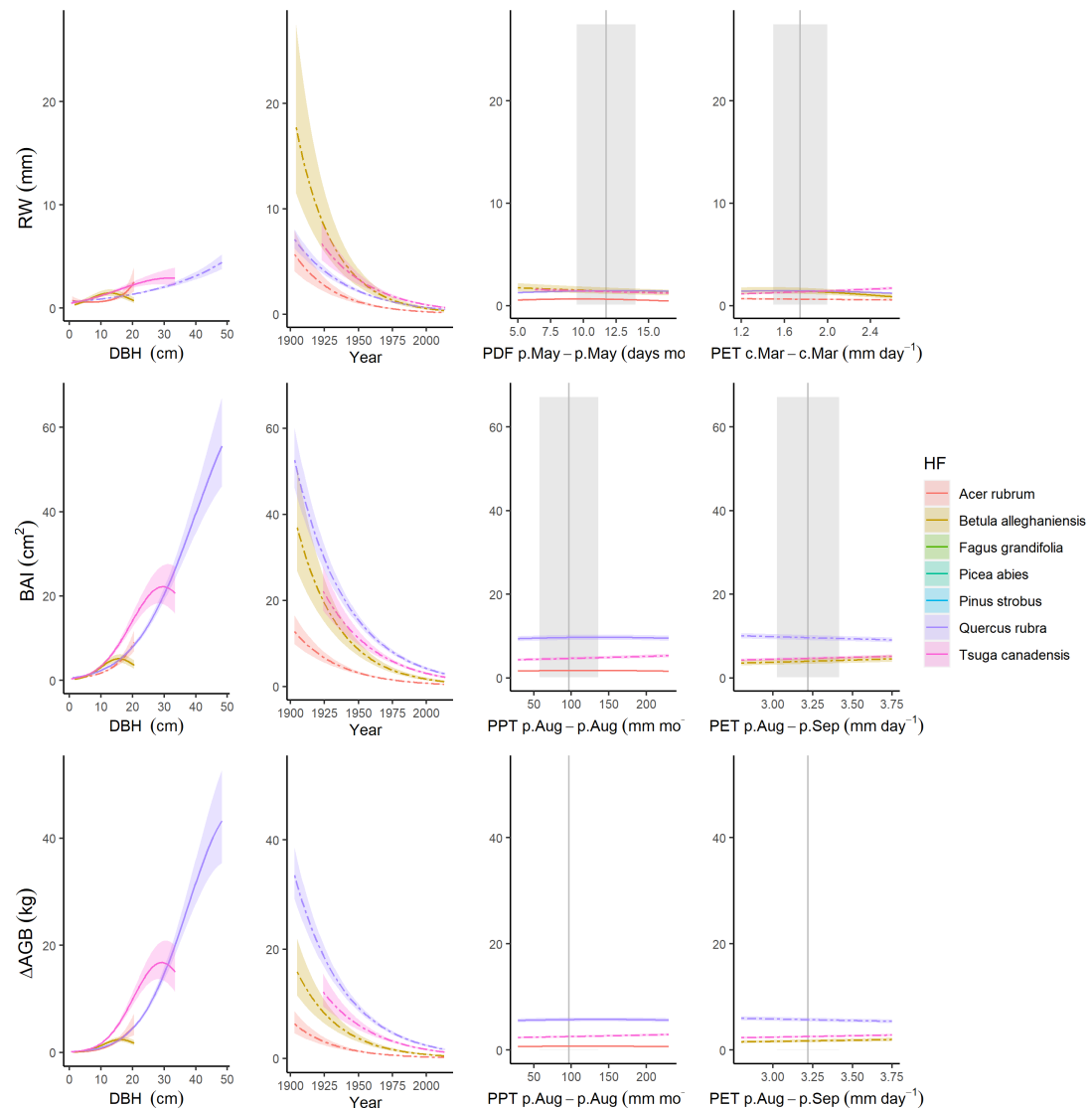


Figure S44. Best GLS models including climate, DBH, and year for HF for all three growth metrics examined here. For each species that met the criteria for inclusion in the analysis, relationships are plotted if included in top model. For each relationship shown, other terms in the model are held constant at their median. Best-fit polynomials are plotted with solid lines when both first- and second-order terms are significant (t-test's p-value <0.05), dashed lines when only one term is significant, and dotted lines when neither is significant. Transparent ribbons indicate 95% confidence intervals. *Climwin*-selected climate variables are coded on the x-axes as the climate variable name followed by the range of months (p=previous year, c=current year) over which it is most influential. Vertical grey lines indicate the long-term mean for the climate variable, shading indicates 1 SD.

Figure S45. Best GLS models including climate and DBH for ZOF

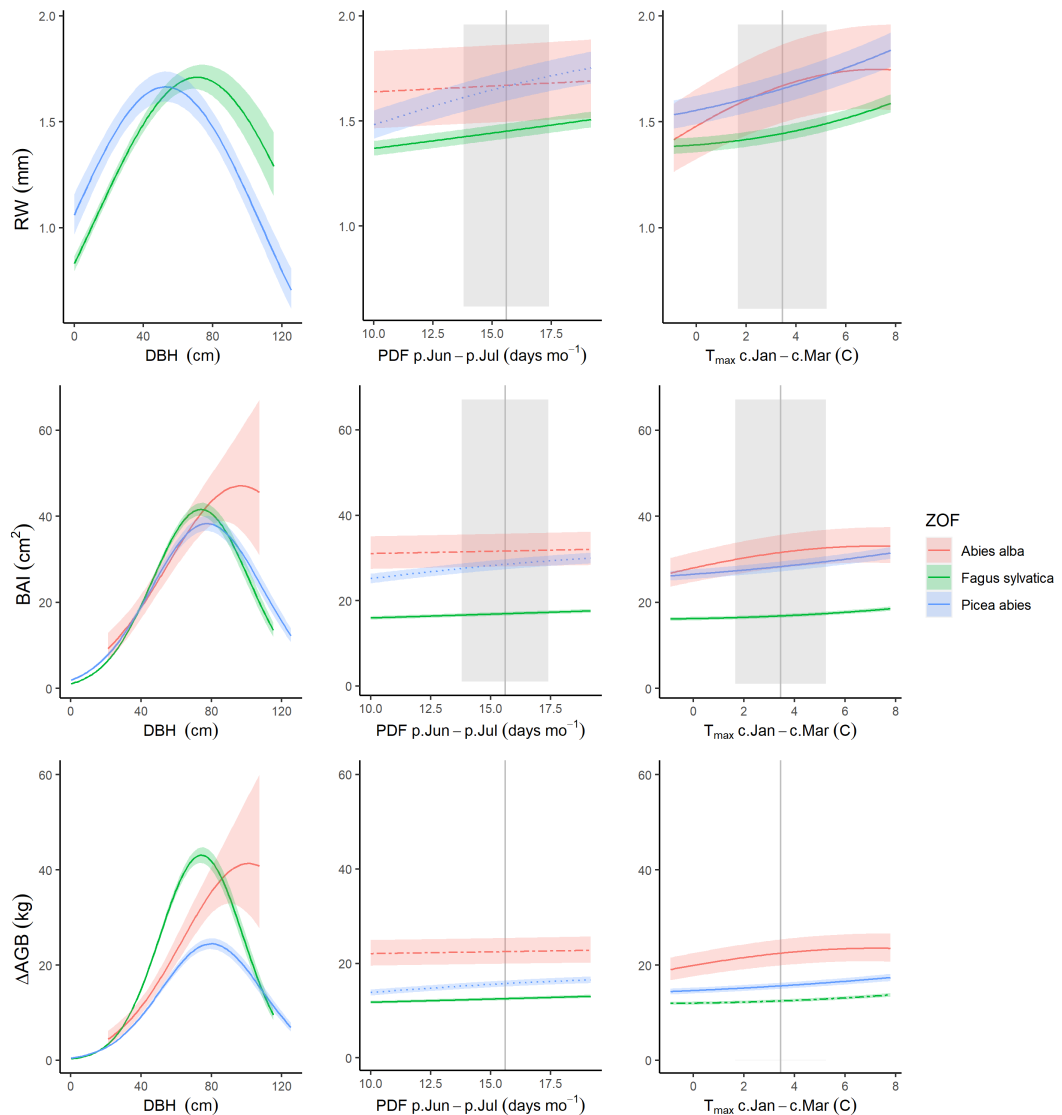


Figure S45. Best GLS models including climate and DBH for ZOF for all three growth metrics examined here. For each species that met the criteria for inclusion in the analysis, relationships are plotted if included in top model. For each relationship shown, other terms in the model are held constant at their median. Best-fit polynomials are plotted with solid lines when both first- and second-order terms are significant (t-test's p-value <0.05), dashed lines when only one term is significant, and dotted lines when neither is significant. Transparent ribbons indicate 95% confidence intervals. *Climwin*-selected climate variables are coded on the x-axes as the climate variable name followed by the range of months (p=previous year, c=current year) over which it is most influential. Vertical grey lines indicate the long-term mean for the climate variable, shading indicates 1 SD.

Figure S46. Best GLS models including climate, DBH, and year for ZOF

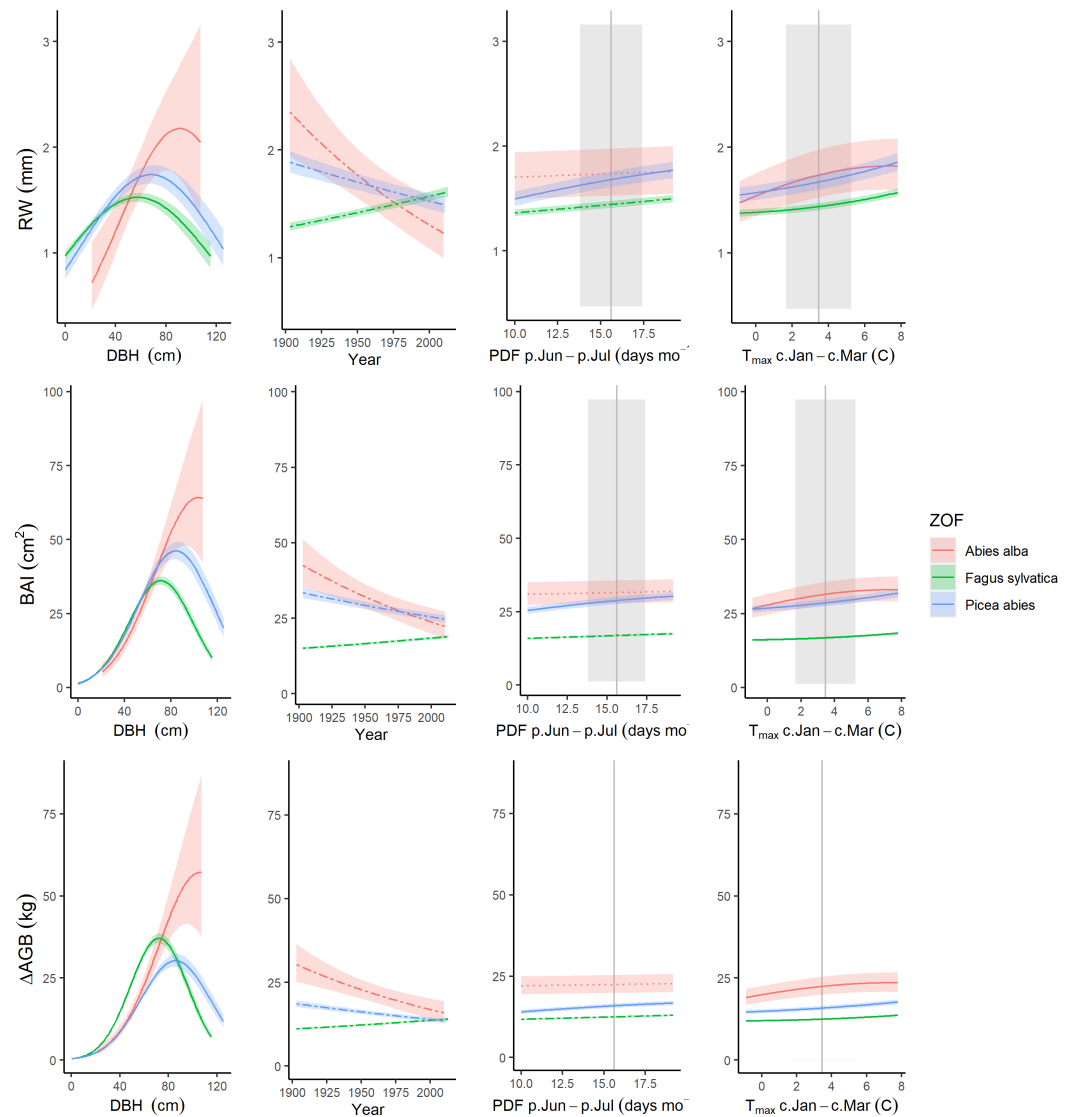


Figure S46. Best GLS models including climate, DBH, and year for ZOF for all three growth metrics examined here. For each species that met the criteria for inclusion in the analysis, relationships are plotted if included in top model. For each relationship shown, other terms in the model are held constant at their median. Best-fit polynomials are plotted with solid lines when both first- and second-order terms are significant (*t*-test's *p*-value <0.05), dashed lines when only one term is significant, and dotted lines when neither is significant. Transparent ribbons indicate 95% confidence intervals. *Climwin*-selected climate variables are coded on the x-axes as the climate variable name followed by the range of months (p=previous year, c=current year) over which it is most influential. Vertical grey lines indicate the long-term mean for the climate variable, shading indicates 1 SD.

Figure S47. Best GLS models including climate and *DBH* for NIO

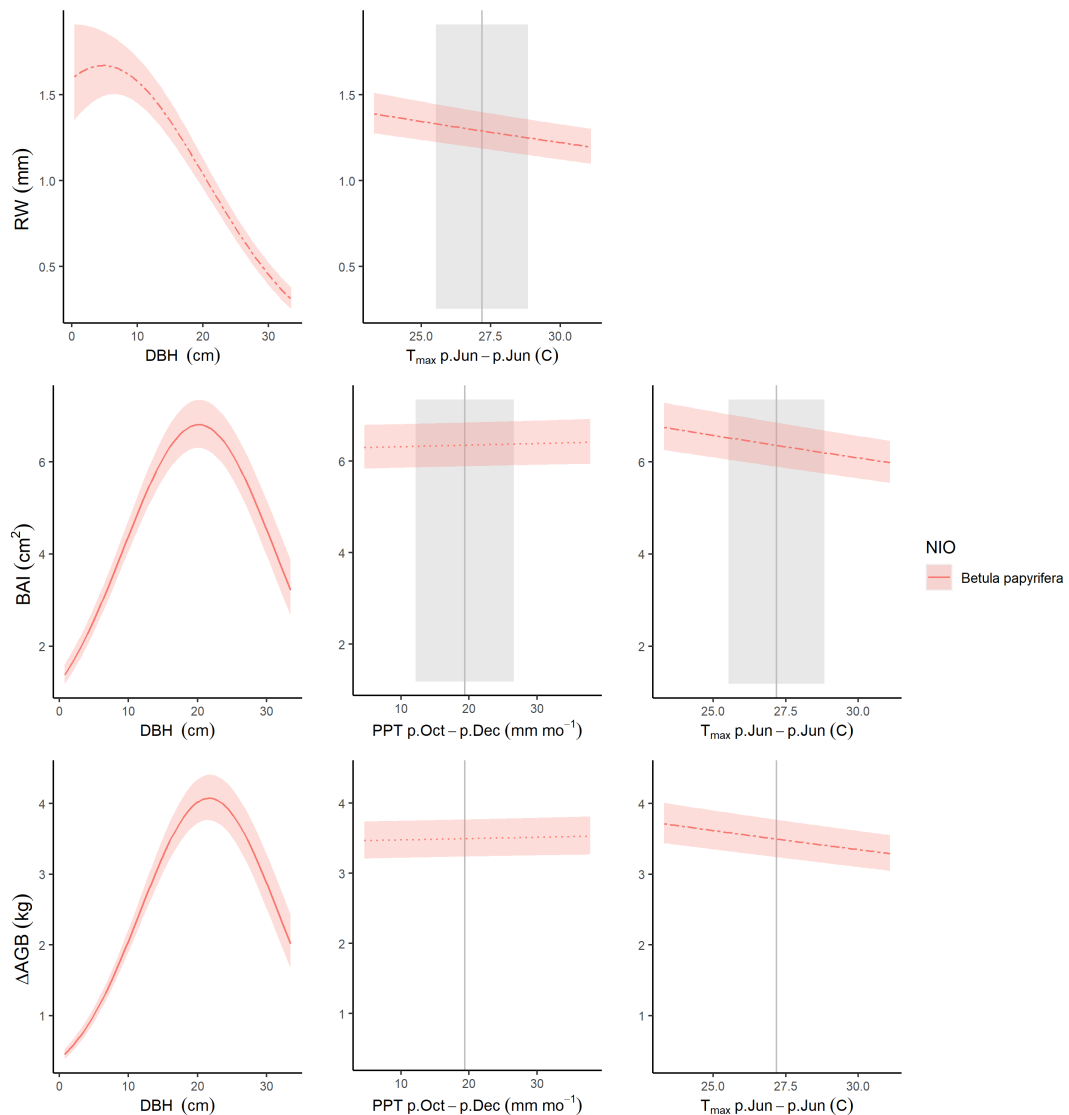


Figure S47. Best GLS models including climate and *DBH* for NIO for all three growth metrics examined here. For each species that met the criteria for inclusion in the analysis, relationships are plotted if included in top model. For each relationship shown, other terms in the model are held constant at their median. Best-fit polynomials are plotted with solid lines when both first- and second-order terms are significant (t-test's p-value <0.05), dashed lines when only one term is significant, and dotted lines when neither is significant. Transparent ribbons indicate 95% confidence intervals. *Climwin*-selected climate variables are coded on the x-axes as the climate variable name followed by the range of months (p=previous year, c=current year) over which it is most influential. Vertical grey lines indicate the long-term mean for the climate variable, shading indicates 1 SD.

Figure S48. Best GLS models including climate, DBH, and year for NIO

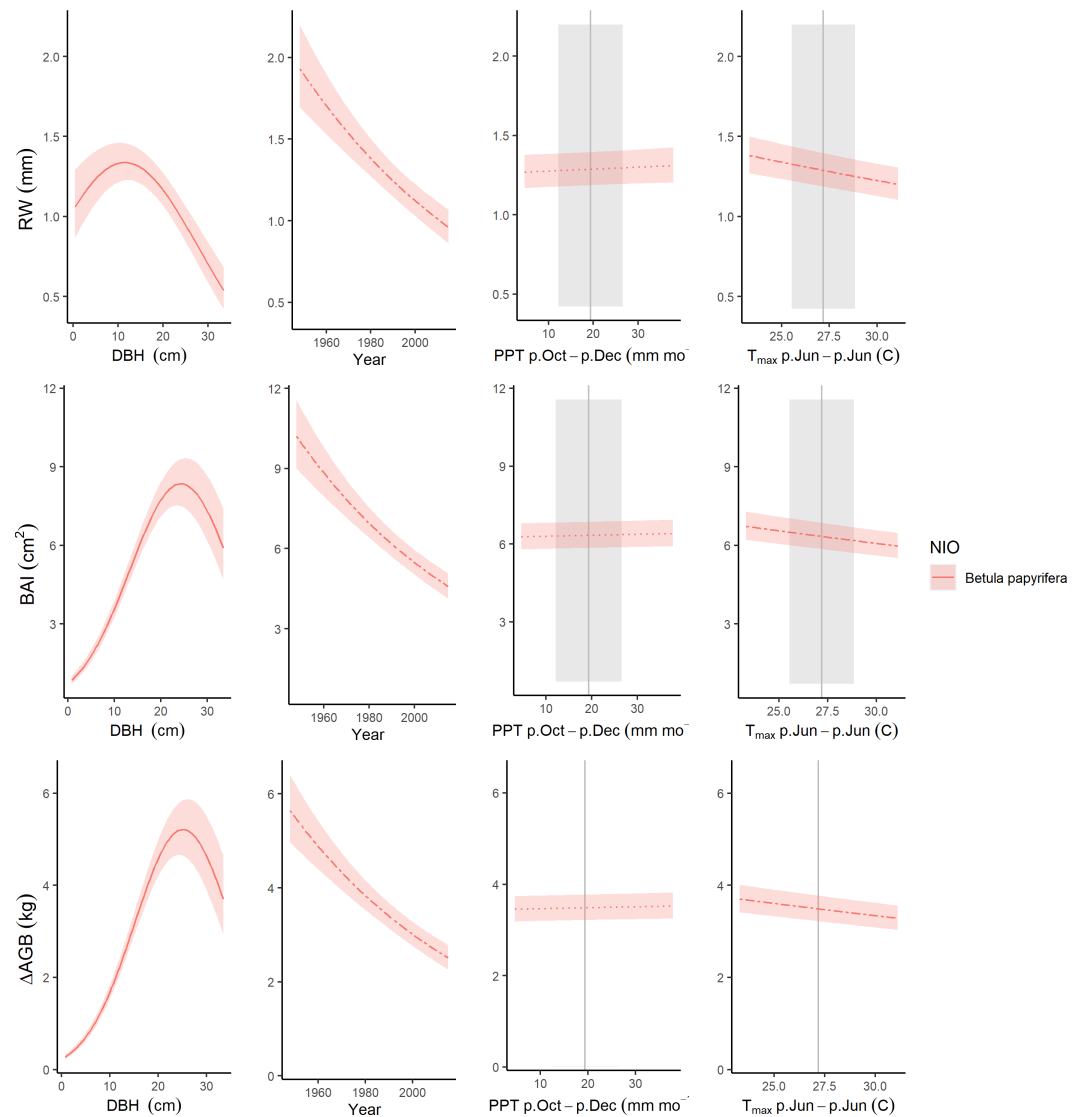


Figure S48. Best GLS models including climate, DBH, and year for NIO for all three growth metrics examined here. For each species that met the criteria for inclusion in the analysis, relationships are plotted if included in top model. For each relationship shown, other terms in the model are held constant at their median. Best-fit polynomials are plotted with solid lines when both first- and second-order terms are significant (*t*-test's *p*-value <0.05), dashed lines when only one term is significant, and dotted lines when neither is significant. Transparent ribbons indicate 95% confidence intervals. *Climwin*-selected climate variables are coded on the x-axes as the climate variable name followed by the range of months (p=previous year, c=current year) over which it is most influential. Vertical grey lines indicate the long-term mean for the climate variable, shading indicates 1 SD.

Figure S49. Best GLS models including climate and *DBH* for LT

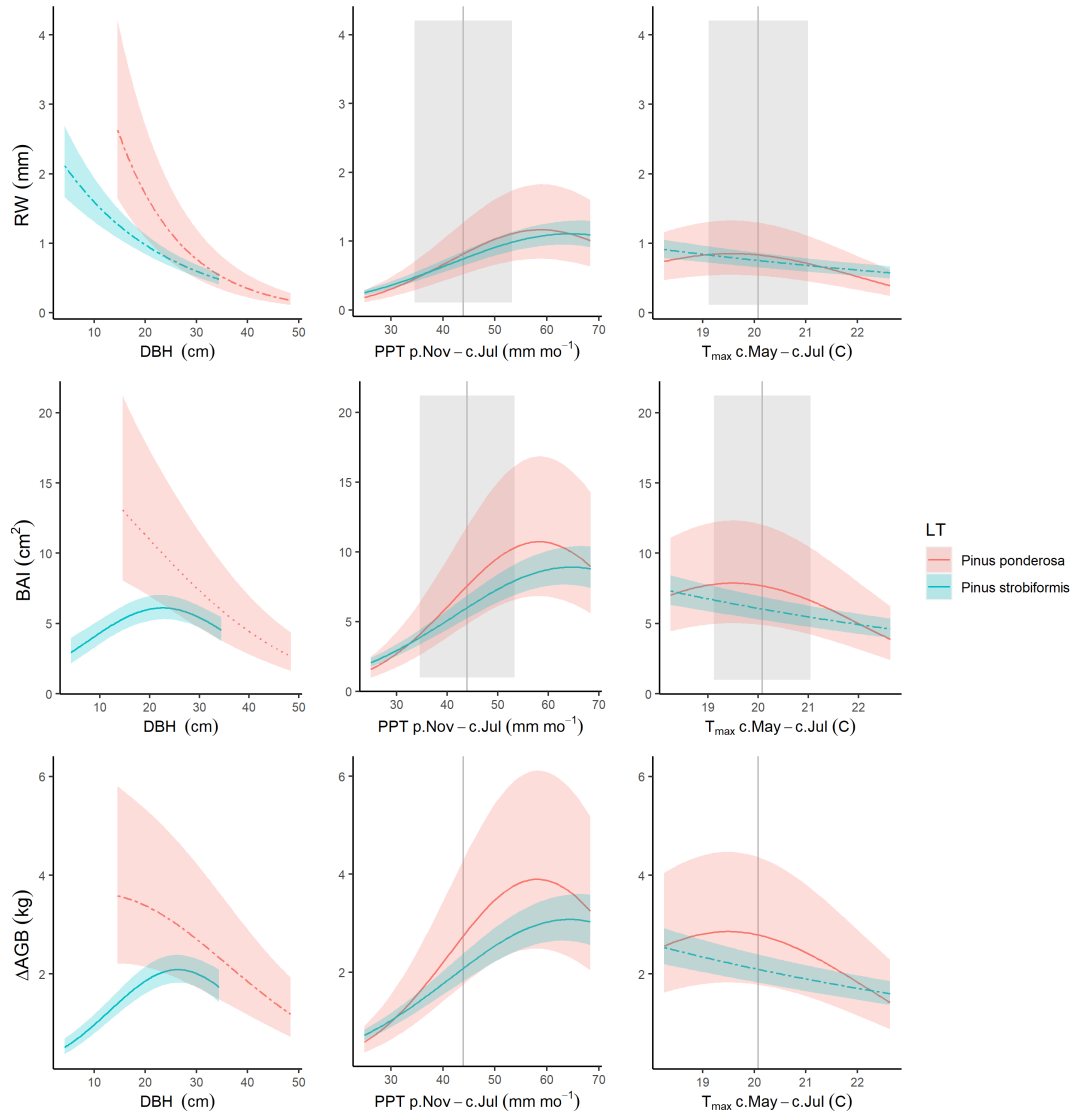


Figure S49. Best GLS models including climate and *DBH* for LT for all three growth metrics examined here. For each species that met the criteria for inclusion in the analysis, relationships are plotted if included in top model. For each relationship shown, other terms in the model are held constant at their median. Best-fit polynomials are plotted with solid lines when both first- and second-order terms are significant (t-test's p-value <0.05), dashed lines when only one term is significant, and dotted lines when neither is significant. *Climwin*-selected climate variables are coded on the x-axes as the climate variable name followed by the range of months (p=previous year, c=current year) over which it is most influential. Vertical grey lines indicate the long-term mean for the climate variable, shading indicates 1 SD.

Figure S50. Best GLS models including climate, DBH, and year for LT

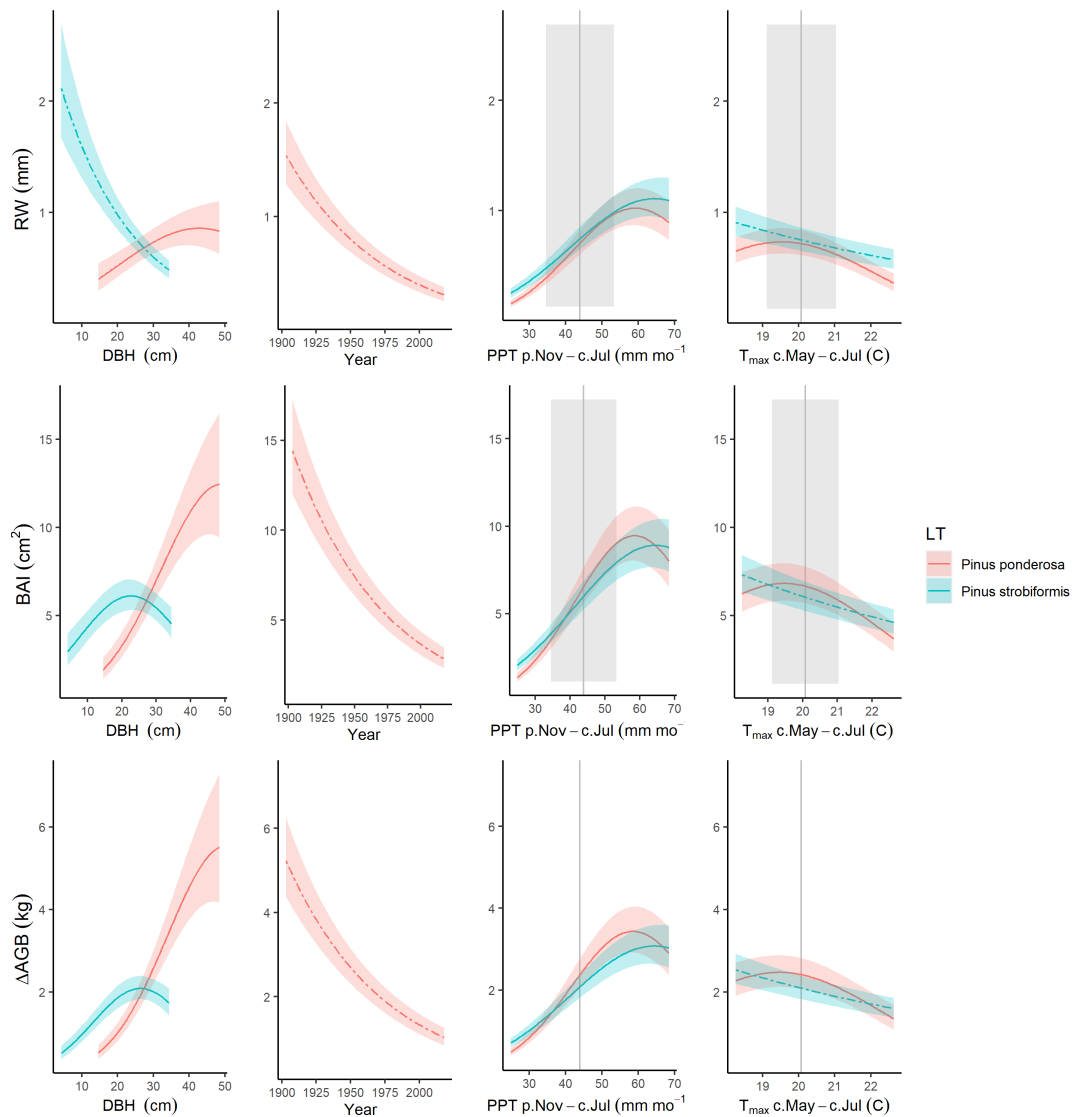


Figure S50. Best GLS models including climate, DBH, and year for LT for all three growth metrics examined here. For each species that met the criteria for inclusion in the analysis, relationships are plotted if included in top model. For each relationship shown, other terms in the model are held constant at their median. Best-fit polynomials are plotted with solid lines when both first- and second-order terms are significant (t-test's p-value <0.05), dashed lines when only one term is significant, and dotted lines when neither is significant. Transparent ribbons indicate 95% confidence intervals. *Climwin*-selected climate variables are coded on the x-axes as the climate variable name followed by the range of months (p=previous year, c=current year) over which it is most influential. Vertical grey lines indicate the long-term mean for the climate variable, shading indicates 1 SD.

Figure S51. Best GLS models including climate and *DBH* for CB

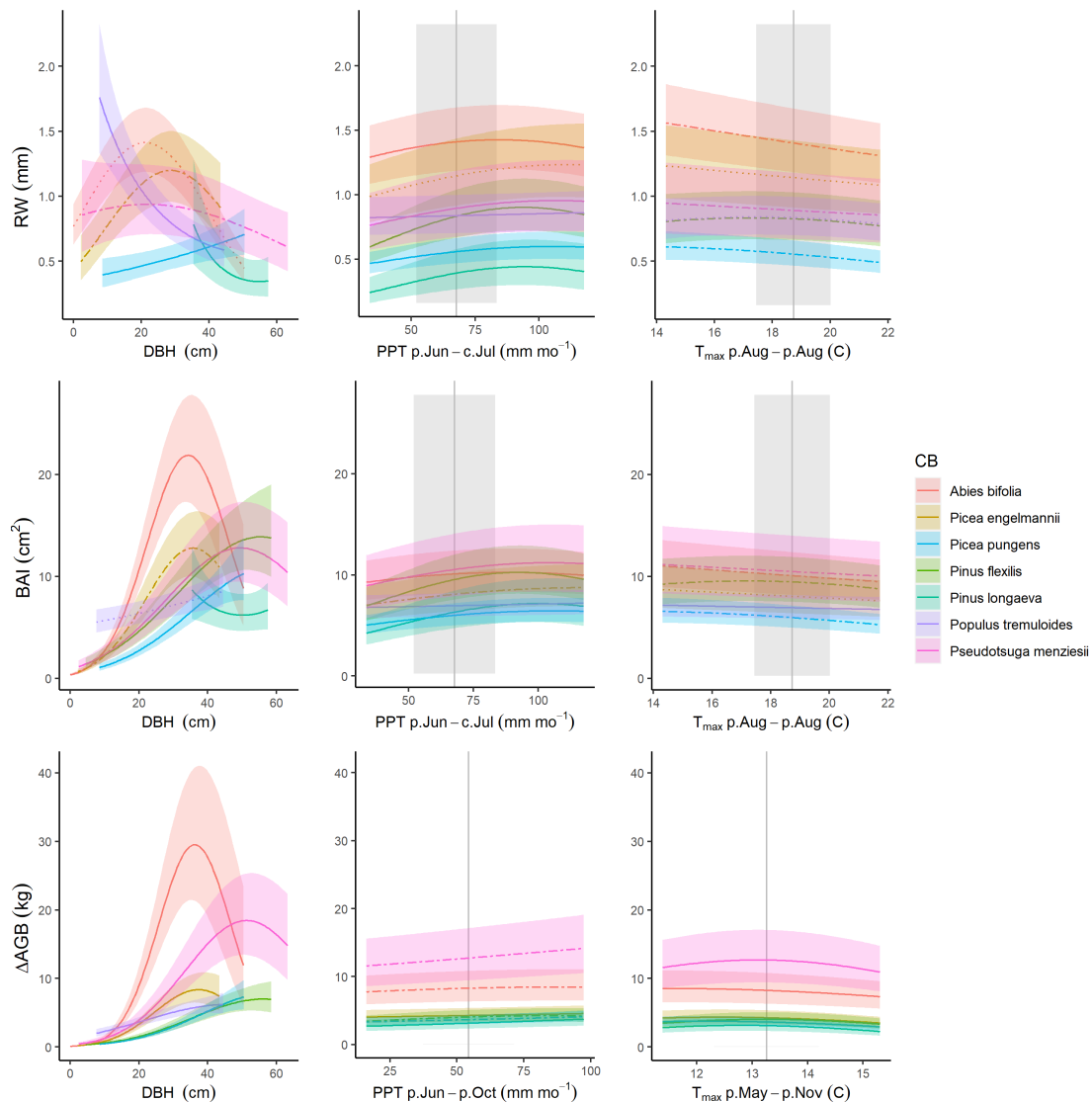


Figure S51. Best GLS models including climate and *DBH* for CB for all three growth metrics examined here. For each species that met the criteria for inclusion in the analysis, relationships are plotted if included in top model. For each relationship shown, other terms in the model are held constant at their median. Best-fit polynomials are plotted with solid lines when both first- and second-order terms are significant (t-test's p-value <0.05), dashed lines when only one term is significant, and dotted lines when neither is significant. Transparent ribbons indicate 95% confidence intervals. *Climwin*-selected climate variables are coded on the x-axes as the climate variable name followed by the range of months (p=previous year, c=current year) over which it is most influential. Vertical grey lines indicate the long-term mean for the climate variable, shading indicates 1 SD.

Figure S52. Best GLS models including climate, DBH, and year for CB

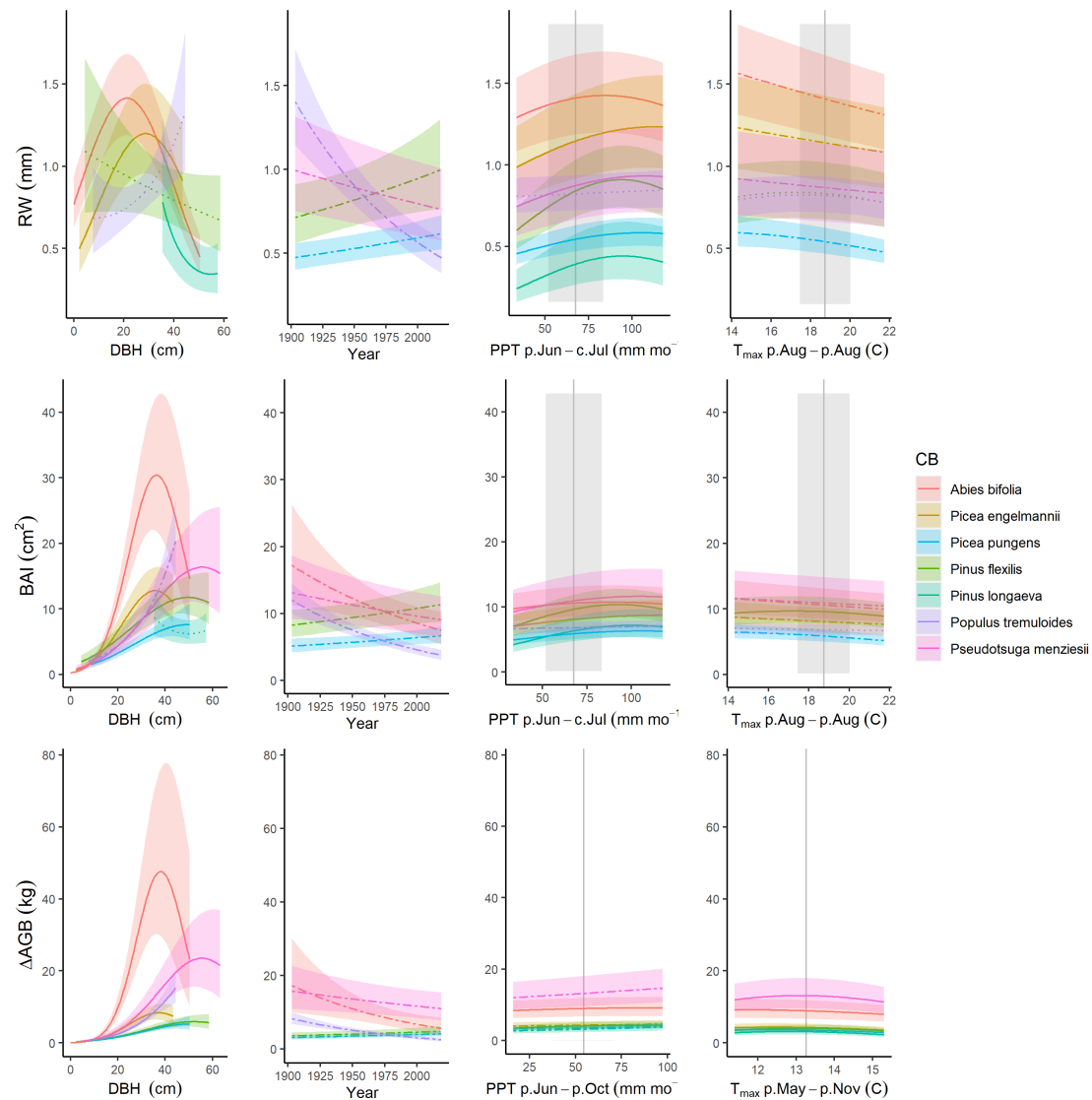


Figure S52. Best GLS models including climate, DBH, and year for CB for all three growth metrics examined here. For each species that met the criteria for inclusion in the analysis, relationships are plotted if included in top model. For each relationship shown, other terms in the model are held constant at their median. Best-fit polynomials are plotted with solid lines when both first- and second-order terms are significant (t -test's p -value <0.05), dashed lines when only one term is significant, and dotted lines when neither is significant. Transparent ribbons indicate 95% confidence intervals. *Climwin*-selected climate variables are coded on the x-axes as the climate variable name followed by the range of months (p=previous year, c=current year) over which it is most influential. Vertical grey lines indicate the long-term mean for the climate variable, shading indicates 1 SD.

Figure S53. Best GLS models including climate and *DBH* for SC

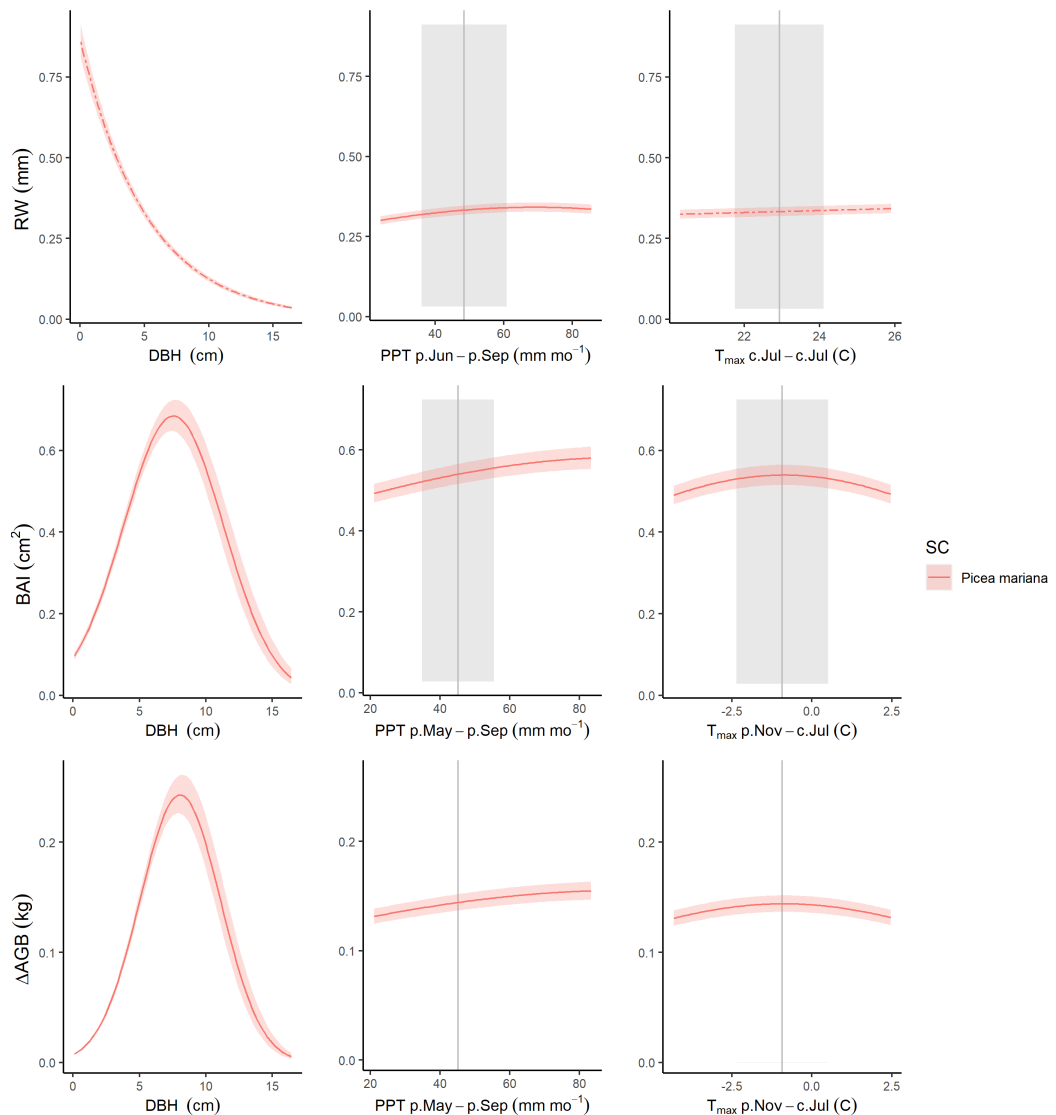


Figure S53. Best GLS models including climate and *DBH* for SC for all three growth metrics examined here. For each species that met the criteria for inclusion in the analysis, relationships are plotted if included in top model. For each relationship shown, other terms in the model are held constant at their median. Best-fit polynomials are plotted with solid lines when both first- and second-order terms are significant (t-test's p-value <0.05), dashed lines when only one term is significant, and dotted lines when neither is significant. Transparent ribbons indicate 95% confidence intervals. *Climwin*-selected climate variables are coded on the x-axes as the climate variable name followed by the range of months (p=previous year, c=current year) over which it is most influential. Vertical grey lines indicate the long-term mean for the climate variable, shading indicates 1 SD.

Figure S54. Best GLS models including climate, DBH, and year for SC

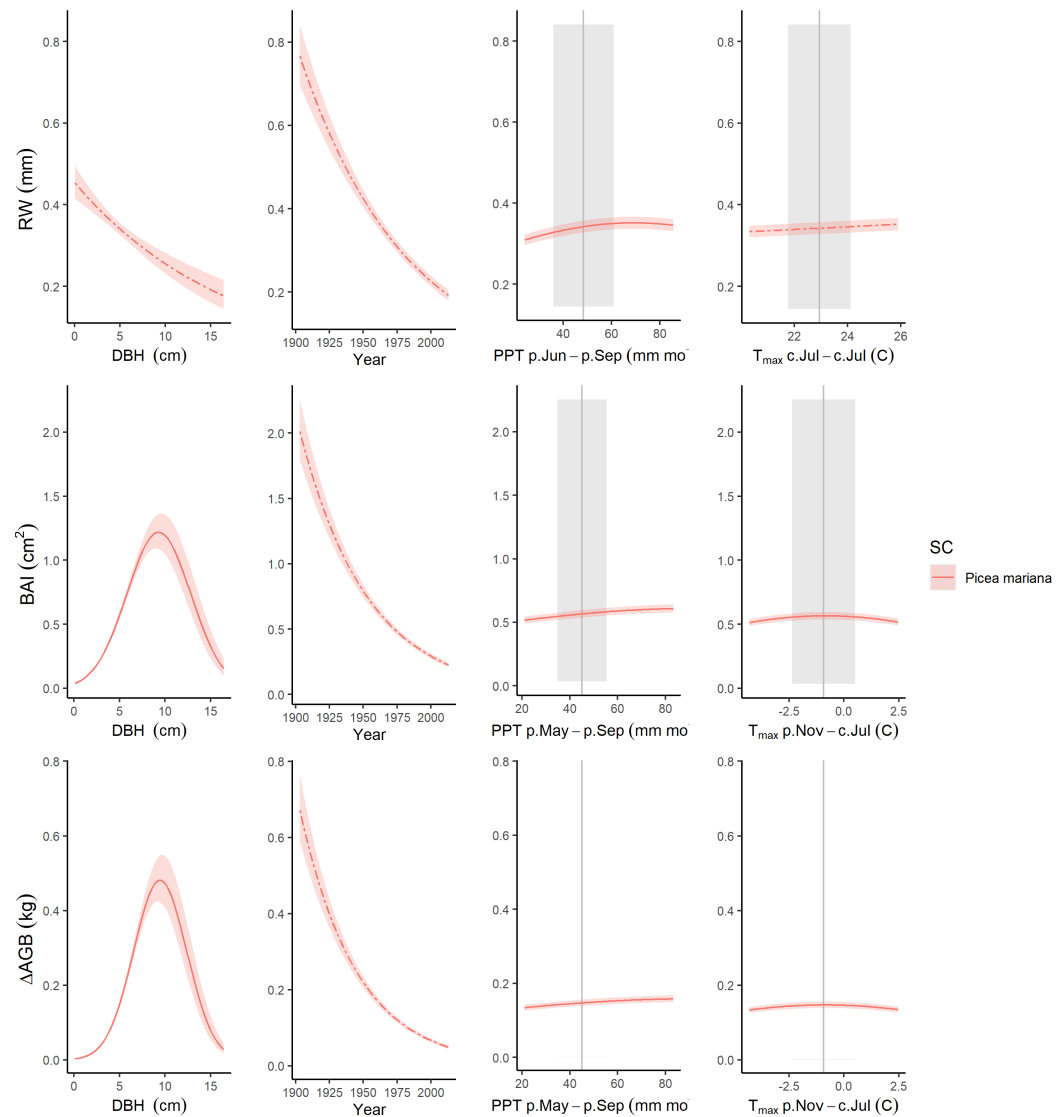
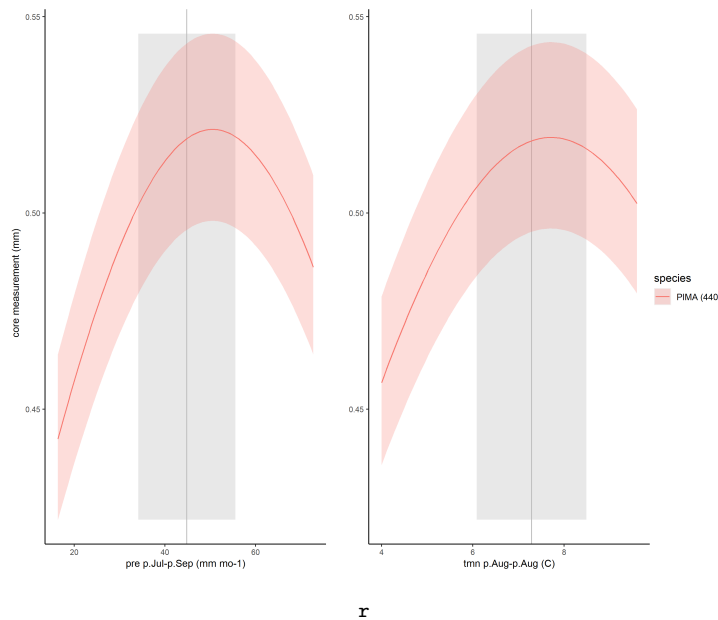


Figure S54. Best GLS models including climate, DBH, and year for SC for all three growth metrics examined here. For each species that met the criteria for inclusion in the analysis, relationships are plotted if included in top model. For each relationship shown, other terms in the model are held constant at their median. Best-fit polynomials are plotted with solid lines when both first- and second-order terms are significant (t -test's p -value <0.05), dashed lines when only one term is significant, and dotted lines when neither is significant. Transparent ribbons indicate 95% confidence intervals. *Climwin*-selected climate variables are coded on the x-axes as the climate variable name followed by the range of months (p=previous year, c=current year) over which it is most influential. Vertical grey lines indicate the long-term mean for the climate variable, shading indicates 1 SD.

Figure S55. Climate responses at SC before and after 1970.

(a) pre-1970



(b) post-1970

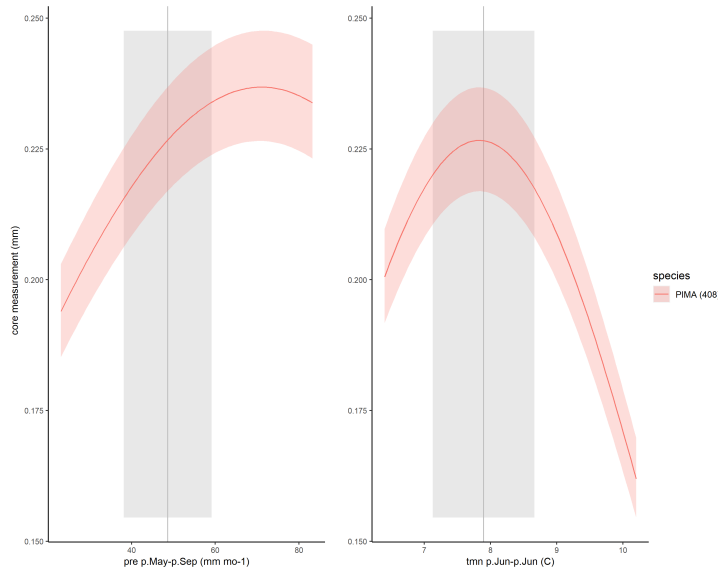


Figure S55. Climate responses at SC before and after 1970. *Climwin*-selected climate variables are coded on the x-axes as the climate variable name followed by the range of months (p=previous year, c=current year) over which it is most influential. For each relationship shown, other terms in the model are held constant at their median. Best-fit polynomials are plotted with solid lines when both first- and second-order terms are significant (t-test's p-value <0.05), dashed lines when only one term is significant, and dotted lines when neither is significant. Transparent ribbons indicate 95% confidence intervals. Vertical grey lines indicate the long-term mean for the climate variable, shading indicates 1 SD.

Figure S56. All significant climate - DBH interactions with RW as the response metric.

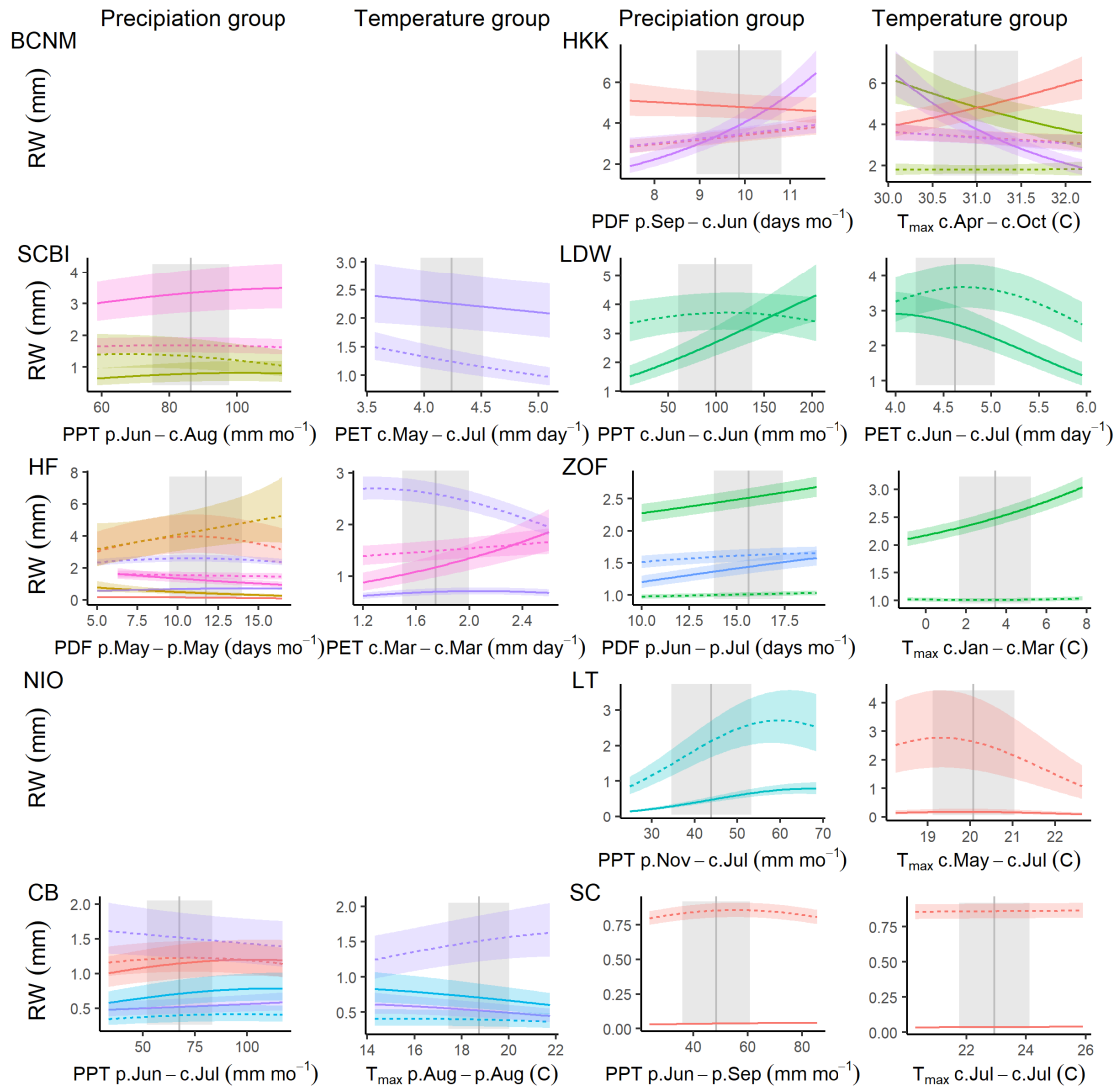


Figure S56. All significant climate - DBH interactions with *RW* as the response metric. Shown are modeled response functions at the minimum and maximum and maximum ends of the DBH range. Other terms in the model are held constant at their median. Transparent ribbons indicate 95% confidence intervals. Vertical grey lines indicate the long-term mean for the climate variable, shading indicates 1 SD.

Figure S57. All significant climate - DBH interactions with RW as the response metric.

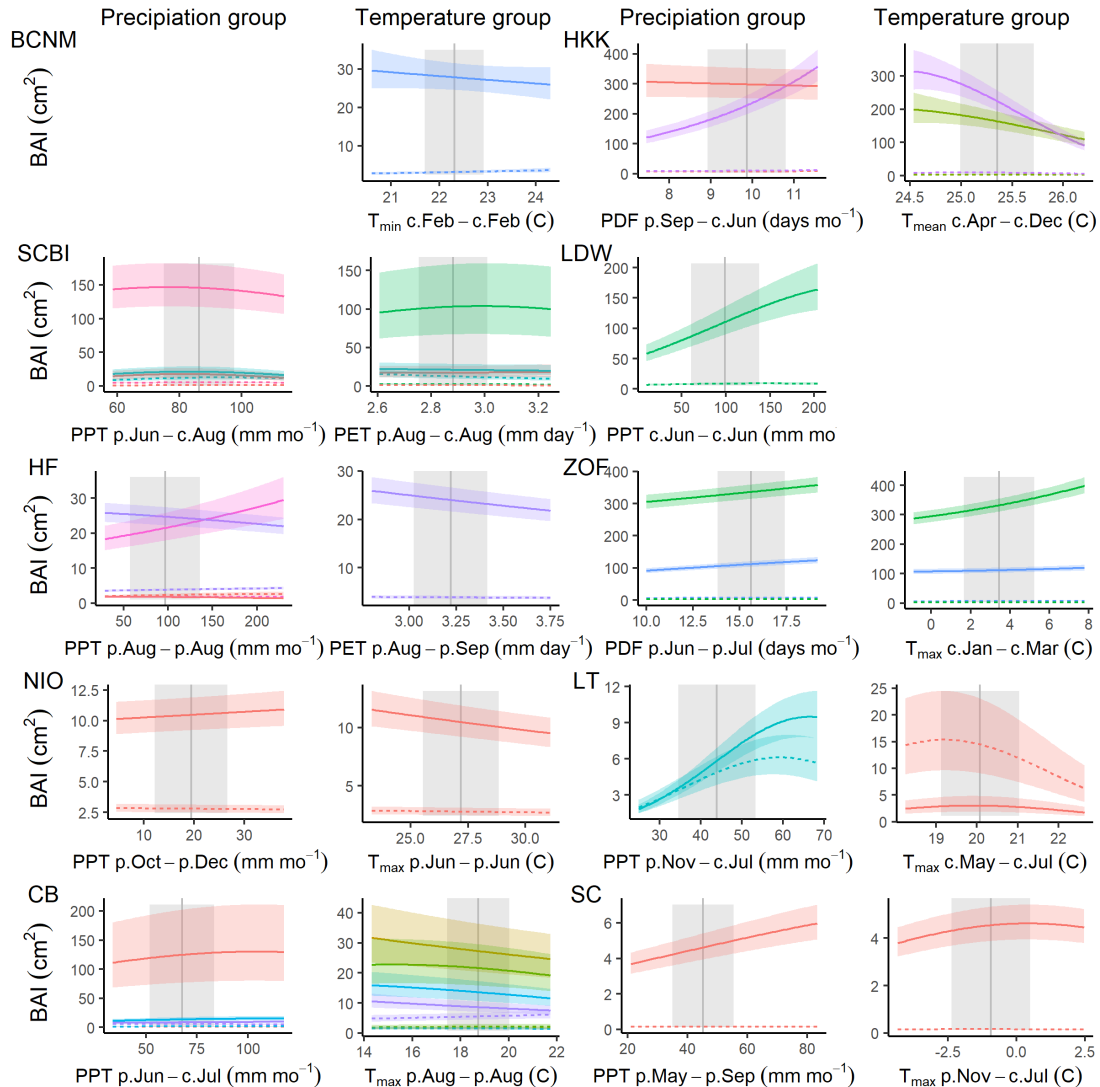


Figure S57. All significant climate - DBH interactions with RW as the response metric. Shown are modeled response functions at the minimum and maximum and maximum ends of the DBH range. Other terms in the model are held constant at their median. Transparent ribbons indicate 95% confidence intervals. Vertical grey lines indicate the long-term mean for the climate variable, shading indicates 1 SD.

Figure S58. Relationships between DBH and BAI by decade for BCNM.

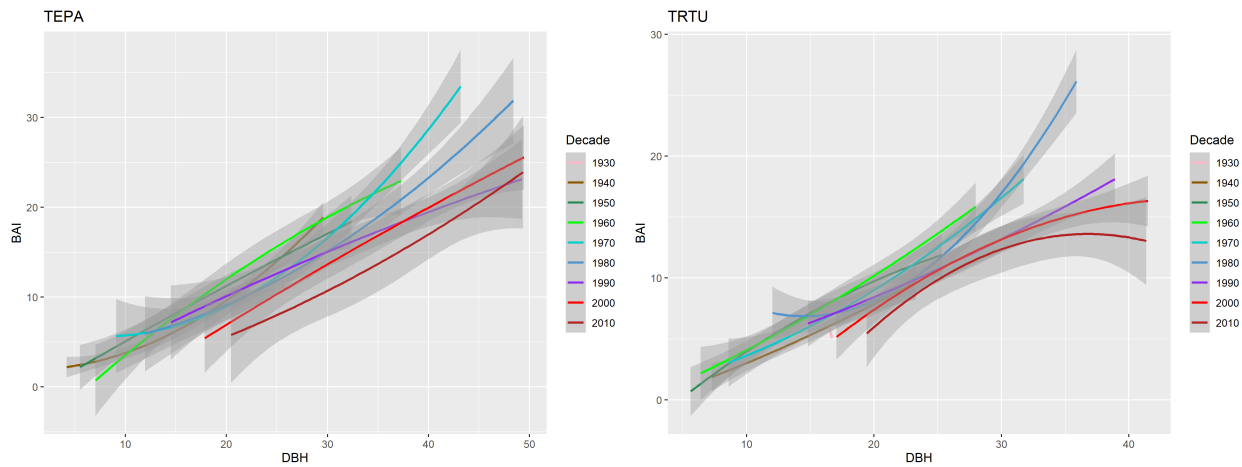


Figure S58. Relationships between DBH and BAI by decade for BCNM. Plot visualizes the data included in the GLS model, separated by decade, using a probability density function. Transparent ribbons indicate 95% confidence intervals.

Figure S59. Relationships between DBH and BAI by decade for HKK.

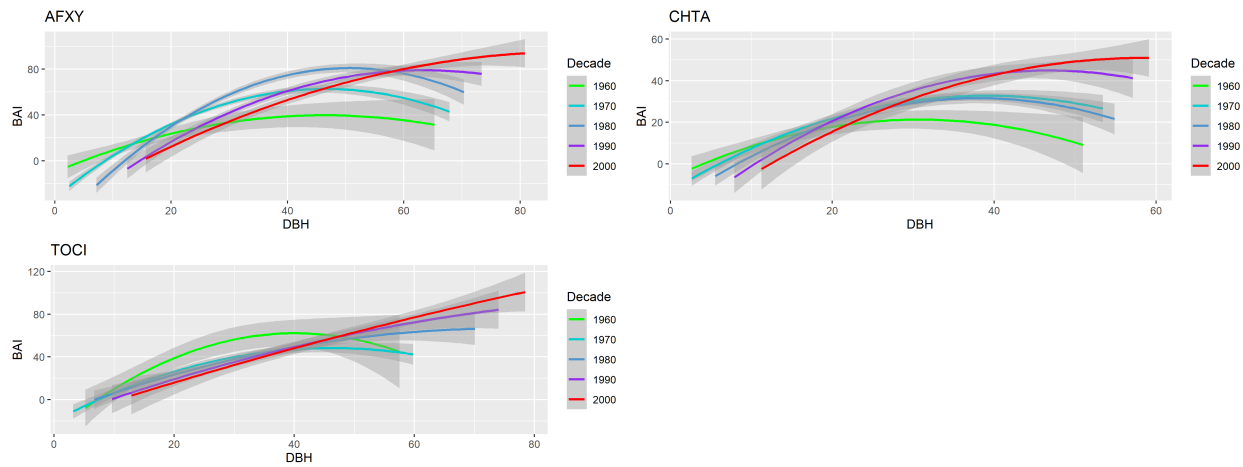


Figure S59. Relationships between DBH and BAI by decade for HKK. Plot visualizes the data included in the GLS model, separated by decade, using a probability density function. Transparent ribbons indicate 95% confidence intervals.

Figure S60. Relationships between DBH and BAI by decade for SCBI.

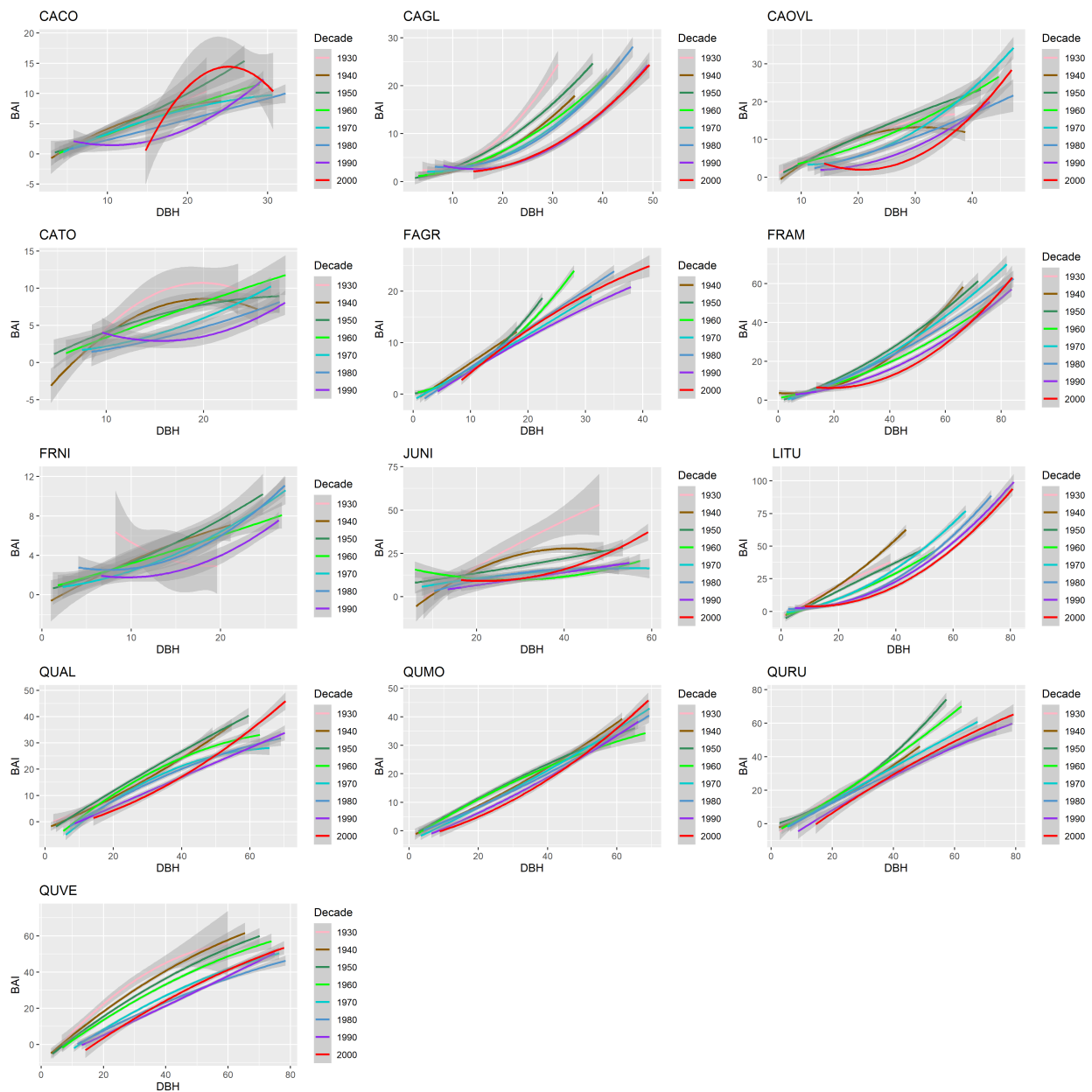


Figure S60. Relationships between DBH and BAI by decade for SCBI. Plot visualizes the data included in the GLS model, separated by decade, using a probability density function. Transparent ribbons indicate 95% confidence intervals.

Figure S61. Relationships between DBH and BAI by decade for LDW.

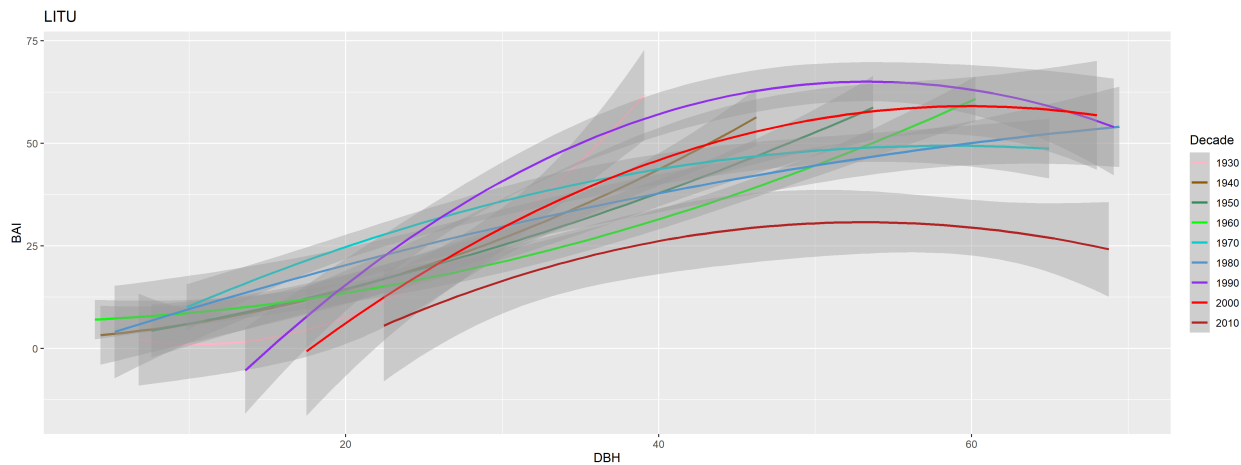


Figure S61. Relationships between DBH and BAI by decade for LDW. Plot visualizes the data included in the GLS model, separated by decade, using a probability density function. Transparent ribbons indicate 95% confidence intervals.

Figure S62. Relationships between DBH and BAI by decade for HF.

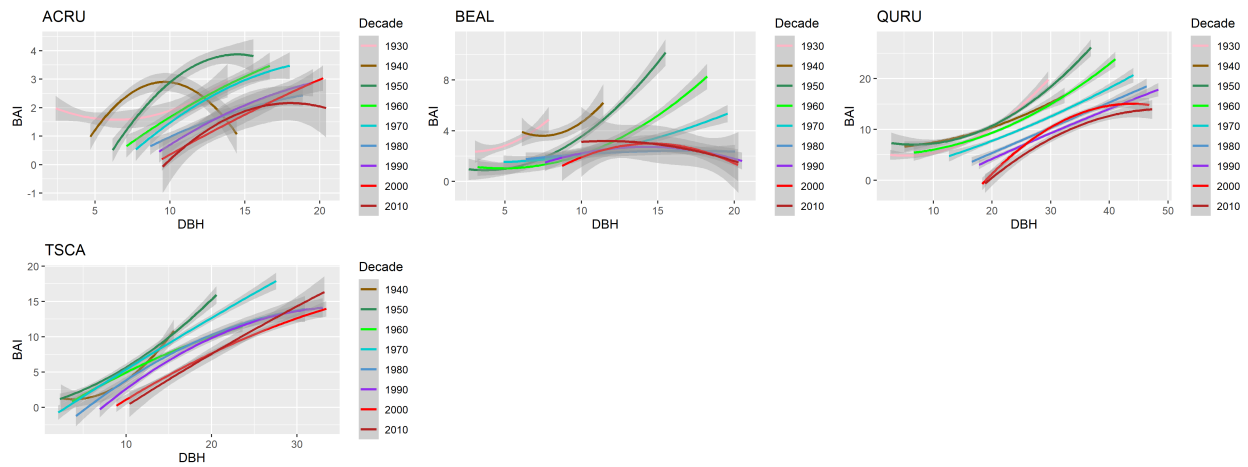


Figure S62. Relationships between DBH and BAI by decade for HF. Plot visualizes the data included in the GLS model, separated by decade, using a probability density function. Transparent ribbons indicate 95% confidence intervals.

Figure S63. Relationships between DBH and BAI by decade for ZOF.

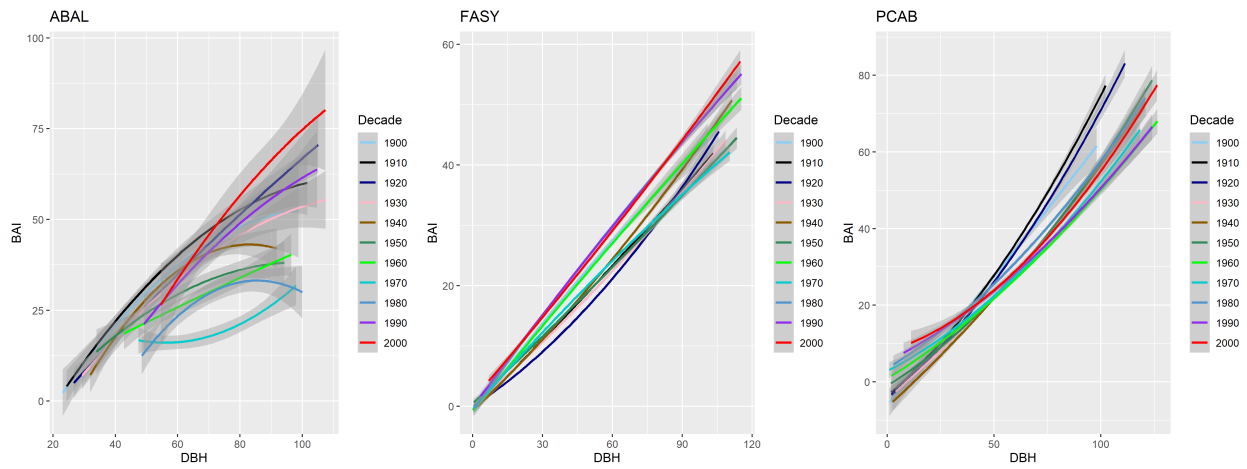


Figure S63. Relationships between DBH and BAI by decade for ZOF. Plot visualizes the data included in the GLS model, separated by decade, using a probability density function. Transparent ribbons indicate 95% confidence intervals.

Figure S64. Relationships between *DBH* and *BAI* by decade for NIO.

```
![`r decadal_plot_NIO_legend` `r decadal_generic_legend`] (tables_figures/SI_figures/decadal_plots/NIO.p
```

Figure S65. Relationships between DBH and BAI by decade for LT.

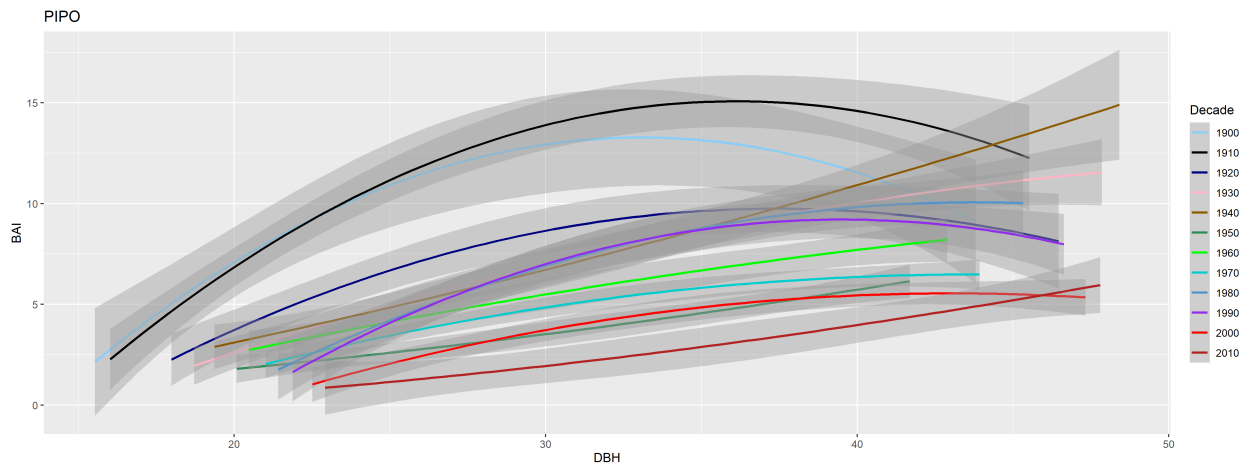


Figure S65. Relationships between DBH and BAI by decade for LT. Plot visualizes the data included in the GLS model, separated by decade, using a probability density function. Transparent ribbons indicate 95% confidence intervals.

Figure S66. Relationships between DBH and BAI by decade for CB.

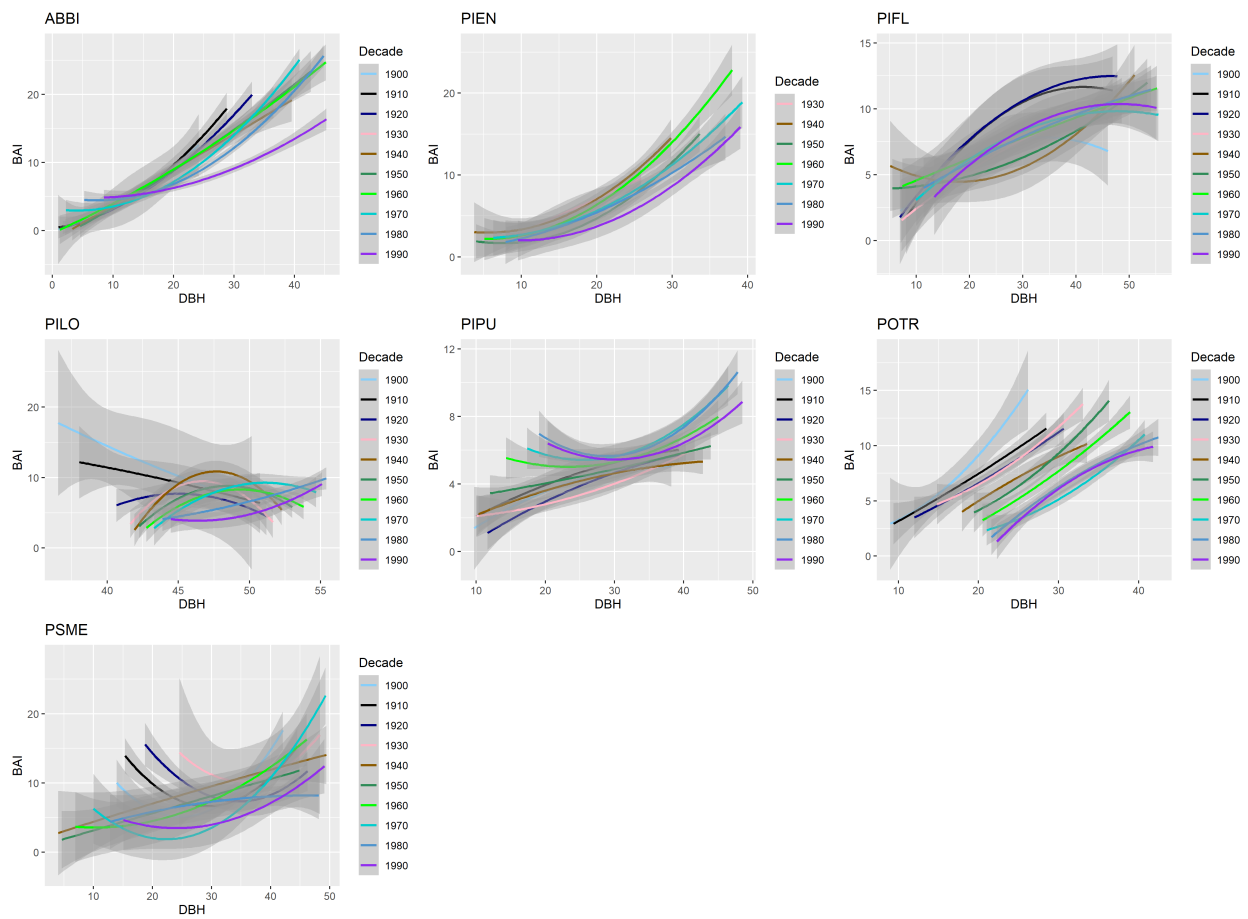


Figure S66. Relationships between DBH and BAI by decade for CB. Plot visualizes the data included in the GLS model, separated by decade, using a probability density function. Transparent ribbons indicate 95% confidence intervals.

Figure S67. Relationships between DBH and BAI by decade for SC.

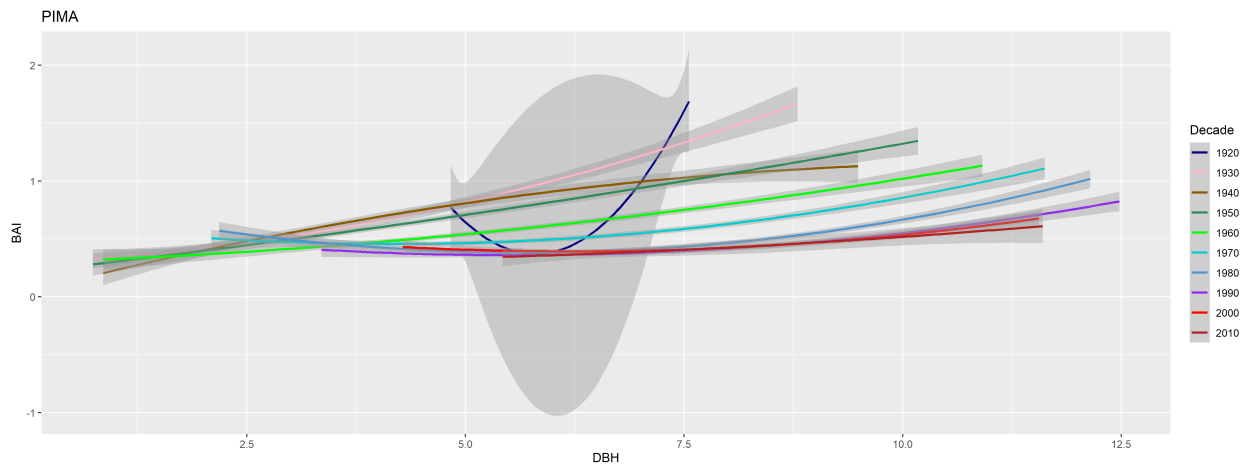


Figure S67. Relationships between DBH and BAI by decade for SC. Plot visualizes the data included in the GLS model, separated by decade, using a probability density function. Transparent ribbons indicate 95% confidence intervals.

SI References

- Alexander, M. R., Pearl, J. K., Bishop, D. A., Cook, E. R., Anchukaitis, K. J., & Pederson, N. (2019). The potential to strengthen temperature reconstructions in ecoregions with limited tree line using a multispecies approach. *Quaternary Research*, 92(2), 583–597. <https://doi.org/10.1017/qua.2019.33>
- Alfaro-Sánchez, R., Muller-Landau, H. C., Wright, S. J., & Camarero, J. J. (2017). Growth and reproduction respond differently to climate in three Neotropical tree species. *Oecologia*. <https://doi.org/10.1007/s00442-017-3879-3>
- Applequist, M. (1958). A simple pith locator for use with off-center increment cores. *Journal of Forestry*.
- Baker, P. J., Bunyavejchewin, S., Oliver, C. D., & Ashton, P. S. (2005). Disturbance history and historical stand dynamics of a seasonal tropical forest in western Thailand. *Ecological Monographs*, 75(3), 317–343. <https://doi.org/10.1890/04-0488>
- Biondi, F., & Waikul, K. (2004). DENDROCLIM2002 : A C++ program for statistical calibration of climate signals in tree-ring chronologies. *Computers & Geosciences*, 30(3), 303–311. <https://doi.org/10.1016/j.cageo.2003.11.004>
- Birch, J. D., DeRose, R. J., & Lutz, J. A. (2020a). Birch - Cedar Breaks National Monument - ABBI - ITRDB UT545. NOAA NCDC. <https://doi.org/https://www.ncdc.noaa.gov/paleo-search/study/31994>
- Birch, J. D., DeRose, R. J., & Lutz, J. A. (2020b). Birch - Cedar Breaks National Monument - PCEN - ITRDB UT546. NOAA NCDC. <https://doi.org/https://www.ncdc.noaa.gov/paleo-search/study/31995>
- Birch, J. D., DeRose, R. J., & Lutz, J. A. (2020c). Birch - Cedar Breaks National Monument - PIFL - ITRDB UT547. NOAA NCDC. <https://doi.org/https://www.ncdc.noaa.gov/paleo-search/study/31996>
- Birch, J. D., DeRose, R. J., & Lutz, J. A. (2020d). Birch - Cedar Breaks National Monument - PSME - ITRDB UT548. NOAA NCDC. <https://doi.org/https://www.ncdc.noaa.gov/paleo-search/study/31997>
- Bourg, N. A., McShea, W. J., Thompson, J. R., McGarvey, J. C., & Shen, X. (2013). Initial census, woody seedling, seed rain, and stand structure data for the SCBI SIGEO Large Forest Dynamics Plot: *Ecological Archives* E094-195. *Ecology*, 94(9), 2111–2112. <https://doi.org/10.1890/13-0010.1>
- Bumann, E., Awada, T., Wardlow, B., Hayes, M., Okalebo, J., Helzer, C., Mazis, A., Hiller, J., & Cherubini, P. (2019). Assessing responses of *Betula Papyrifera* to climate variability in a remnant population along the Niobrara River Valley in Nebraska, U.S.A., Through dendroecological and remote-sensing techniques. *Canadian Journal of Forest Research*, 49(5), 423–433. <https://doi.org/10.1139/cjfr-2018-0206>
- Bunn, A. G. (2008). A dendrochronology program library in R (dplR). *Dendrochronologia*, 26(2), 115–124. <https://doi.org/10.1016/j.dendro.2008.01.002>
- Charney, N. D., Babst, F., Poulter, B., Record, S., Trouet, V. M., Frank, D., Enquist, B. J., & Evans, M. E. K. (2016). Observed forest sensitivity to climate implies large changes in 21st century North American forest growth. *Ecology Letters*, 19(9), 1119–1128. <https://doi.org/10.1111/ele.12650>
- Cook, Edward Roger. (1985). *A Time Series Analysis Approach to Tree Ring Standardization: Vol. PhD [PhD thesis]*. University of Arizona.
- Cook, E. R., & Kairiukstis, L. A. (Eds.). (1990). *Methods of Dendrochronology: Applications in the Environmental Sciences*. Springer Netherlands. <https://doi.org/10.1007/978-94-015-7879-0>
- Cook, Edward R., & Peters, K. (1997). Calculating unbiased tree-ring indices for the study of climatic and environmental change. *The Holocene*, 7(3), 361–370. <https://doi.org/10.1177/095968369700700314>
- Daly, C., Halbleib, M., Smith, J. I., Gibson, W. P., Doggett, M. K., Taylor, G. H., Curtis, J., & Pasteris, P. P. (2008). Physiographically sensitive mapping of climatological temperature and precipitation across the conterminous United States. *International Journal of Climatology*, 28(15), 2031–2064. <https://doi.org/10.1002/joc.1688>

- Daly, C., Smith, J. I., & Olson, K. V. (2015). Mapping Atmospheric Moisture Climatologies across the Conterminous United States. *PLOS ONE*, 10(10), e0141140. <https://doi.org/10.1371/journal.pone.0141140>
- Dearborn, K. D., Wallace, C. A., Patankar, R., & Baltzer, J. L. (2020). Permafrost thaw in boreal peatlands is rapidly altering forest community composition. *Journal of Ecology*. <https://doi.org/10.1111/1365-2745.13569>
- Driscoll, W. W., Wiles, G. C., D'Arrigo, R. D., & Wilmking, M. (2005). Divergent tree growth response to recent climatic warming, Lake Clark National Park and Preserve, Alaska. *Geophysical Research Letters*, 32(20). <https://doi.org/10.1029/2005GL024258>
- Duncan, R. P. (1989). An evaluation of errors in tree age estimates based on increment cores in kahikatea (*Dacrycarpus dacrydioides*). *New Zealand Natural Sciences*, 16, 31–37.
- Dye, A., Barker Plotkin, A., Bishop, D., Pederson, N., Poulter, B., & Hessl, A. (2016). Comparing tree-ring and permanent plot estimates of aboveground net primary production in three eastern U.S. forests. *Ecosphere*, 7(9), e01454. <https://doi.org/10.1002/ecs2.1454>
- Elling, W., Dittmar, C., Pfaffelmoser, K., & Rötzer, T. (2009). Dendroecological assessment of the complex causes of decline and recovery of the growth of silver fir (*Abies alba* Mill.) In Southern Germany. *Forest Ecology and Management*, 257(4), 1175–1187. <https://doi.org/10.1016/j.foreco.2008.10.014>
- Finzi, A. C., Giasson, M.-A., Plotkin, A. A. B., Aber, J. D., Boose, E. R., Davidson, E. A., Dietze, M. C., Ellison, A. M., Frey, S. D., Goldman, E., Keenan, T. F., Melillo, J. M., Munger, J. W., Nadelhoffer, K. J., Ollinger, S. V., Orwig, D. A., Pederson, N., Richardson, A. D., Savage, K., ... Foster, D. R. (2020). Carbon budget of the Harvard Forest Long-Term Ecological Research site: Pattern, process, and response to global change. *Ecological Monographs*, 90(4), e01423. <https://doi.org/10.1002/ecm.1423>
- Furniss, T. J., Larson, A. J., & Lutz, J. A. (2017). Reconciling niches and neutrality in a subalpine temperate forest. *Ecosphere*, 8(6). <https://doi.org/10.1002/ecs2.1847>
- Gonzalez-Akre, E., Meakem, V., Eng, C.-Y., Tepley, A. J., Bourg, N. A., McShea, W., Davies, S. J., & Anderson-Teixeira, K. (2016). Patterns of tree mortality in a temperate deciduous forest derived from a large forest dynamics plot. *Ecosphere*, 7(12), e01595. <https://doi.org/10.1002/ecs2.1595>
- Harris, I., Jones, P. D., Osborn, T. J., & Lister, D. H. (2014). Updated high-resolution grids of monthly climatic observations - the CRU TS3.10 Dataset. *International Journal of Climatology*, 34(3), 623–642. <https://doi.org/10.1002/joc.3711>
- Harris, Ian, Osborn, T. J., Jones, P., & Lister, D. (2020). Version 4 of the CRU TS monthly high-resolution gridded multivariate climate dataset. *Scientific Data*, 7(1). <https://doi.org/10.1038/s41597-020-0453-3>
- Helcoski, R., Tepley, A. J., Pederson, N., McGarvey, J. C., Meakem, V., Herrmann, V., Thompson, J. R., & Anderson-Teixeira, K. J. (2019). Growing season moisture drives interannual variation in woody productivity of a temperate deciduous forest. *New Phytologist*, 223(3), 1204–1216. <https://doi.org/10.1111/nph.15906>
- Jones, P. D., Osborn, T. J., & Briffa, K. R. (1997). Estimating sampling errors in large-scale temperature averages. *Journal of Climate*, 10(10), 2548–2568.
- Kašpar, K., Tumajer, J., Vašíčková, I., & Šamonil, P. (in review). *Species-specific climate-growth interactions determine the future tree species dynamics of the mixed Central European mountain forests*.
- Kozáková, R., Šamonil, P., Kuneš, P., Novák, J., Kočár, P., & Kočárová, R. (2011). Contrasting local and regional Holocene histories of *Abies alba* in the Czech Republic in relation to human impact: Evidence from forestry, pollen and anthracological data. *The Holocene*, 21(3), 431–444. <https://doi.org/10.1177/0959683610385721>
- Maxwell, J. T., Harley, G. L., & Robeson, S. M. (2016). On the declining relationship between tree growth and climate in the Midwest United States: The fading drought signal. *Climatic Change*, 138(1-2), 127–142.

- <https://doi.org/10.1007/s10584-016-1720-3>
- Ninemets, Ü., & Valladares, F. (2006). Tolerance to shade, drought, and waterlogging of temperate northern hemisphere trees and shrubs. *Ecological Monographs*, 76(4), 521–547. <https://doi.org/10.6084/m9.figshare.e.c.3309258.v1>
- Paton, S. (2019). *Barro Colorado Island, Clearing_Precipitation, manual*. The Smithsonian Institution. <https://doi.org/10.25573/data.10042502.v3>
- Rutishauser, E., Wright, S. J., Condit, R., Hubbell, S. P., Davies, S. J., & Muller-Landau, H. C. (2020). Testing for changes in biomass dynamics in large-scale forest datasets. *Global Change Biology*, 26(3), 1485–1498. <https://doi.org/10.1111/gcb.14833>
- Sniderhan, A. E., & Baltzer, J. L. (2016). Growth dynamics of black spruce (*Picea Mariana*) in a rapidly thawing discontinuous permafrost peatland: Growth Dynamics Boreal Peatlands. *Journal of Geophysical Research: Biogeosciences*, 121(12), 2988–3000. <https://doi.org/10.1002/2016JG003528>
- Speer, J. H. (2010). *Fundamentals of tree-ring research*. Univ. of Arizona Press.
- Šamonil, Pavel, Doleželová, P., Vašíčková, I., Adam, D., Valterá, M., Král, K., Janík, D., & Šebková, B. (2013). Individual-based approach to the detection of disturbance history through spatial scales in a natural beech-dominated forest. *Journal of Vegetation Science*, 24(6), 1167–1184. <https://doi.org/10.1111/jvs.12025>
- Šamonil, Pavel, Kotík, L., & Vašíčková, I. (2015). Uncertainty in detecting the disturbance history of forest ecosystems using dendrochronology. *Dendrochronologia*, 35, 51–61. <https://doi.org/10.1016/j.dendro.2015.05.005>
- Šamonil, P., Timková, J., & Vašíčková, I. (2016). Uncertainty in the detection of disturbance spatial patterns in temperate forests. *Dendrochronologia*, 37, 46–56. <https://doi.org/10.1016/j.dendro.2015.12.002>
- Šamonil, P., Vašíčková, I., Daněk, P., Janík, D., & Adam, D. (2014). Disturbances can control fine-scale pedodiversity in old-growth forests: Is the soil evolution theory disturbed as well? *Biogeosciences*, 11(20), 5889–5905. <https://doi.org/10.5194/bg-11-5889-2014>
- Šamonil, Pavel, & Vrška, T. (2008). Long-term vegetation dynamics in the Šumava Mts. Natural spruce-fir-beech forests. *Plant Ecology*, 196(2), 197–214. <https://doi.org/10.1007/s11258-007-9345-2>
- Touchan, R., Woodhouse, C. A., Meko, D. M., & Allen, C. (2011). Millennial precipitation reconstruction for the Jemez Mountains, New Mexico, reveals changing drought signal. *International Journal of Climatology*, 31(6), 896–906. <https://doi.org/10.1002/joc.2117>
- Tumajer, J., Altman, J., Štěpánek, P., Treml, V., Doležal, J., & Cienciala, E. (2017). Increasing moisture limitation of Norway spruce in Central Europe revealed by forward modelling of tree growth in tree-ring network. *Agricultural and Forest Meteorology*, 247, 56–64. <https://doi.org/10.1016/j.agrformet.2017.07.015>
- Vašíčková, I., Šamonil, P., Fuentes Ubilla, A. E., Král, K., Daněk, P., & Adam, D. (2016). The true response of *Fagus sylvatica* L. To disturbances: A basis for the empirical inference of release criteria for temperate forests. *Forest Ecology and Management*, 374, 174–185. <https://doi.org/10.1016/j.foreco.2016.04.055>
- Vašíčková, I., Šamonil, P., Král, K., Fuentes Ubilla, A. E., Daněk, P., & Adam, D. (2019). Driving factors of the growth response of *Fagus sylvatica* L. To disturbances: A comprehensive study from Central-European old-growth forests. *Forest Ecology and Management*, 444, 96–106. <https://doi.org/10.1016/j.foreco.2019.04.018>
- Vlam, M., Baker, P. J., Bunyavejchewin, S., & Zuidema, P. A. (2014). Temperature and rainfall strongly drive temporal growth variation in Asian tropical forest trees. *Oecologia*, 174(4), 1449–1461. <https://doi.org/10.1007/s00442-013-2846-x>
- Williams, A. P., Allen, C. D., Macalady, A. K., Griffin, D., Woodhouse, C. A., Meko, D. M., Swetnam, T. W., Rauscher, S. A., Seager, R., Grissino-Mayer, H. D., Dean, J. S., Cook, E. R., Gangodagamage, C., Cai, M., & McDowell, N. G. (2013). Temperature as a potent driver of regional forest drought stress and tree mortality. *Nature Climate Change*, 3(3), 292–297. <https://doi.org/10.1038/nclimate1693>

Wilmking, M., Juday, G. P., Barber, V. A., & Zald, H. S. J. (2004). Recent climate warming forces contrasting growth responses of white spruce at treeline in Alaska through temperature thresholds. *Global Change Biology*, 10(10), 1724–1736. <https://doi.org/10.1111/j.1365-2486.2004.00826.x>

Zang, C., & Biondi, F. (2013). Dendroclimatic calibration in R: The bootRes package for response and correlation function analysis. *Dendrochronologia*, 31(1), 68–74. <https://doi.org/10.1016/j.dendro.2012.08.001>